Employing the Au(111) surface as substrate for the synthesis of two-dimensional metal oxide and metal sulfide structures

Dissertation
zur Erlangung des Doktorgrades
der Naturwissenschaften
— Dr. rer. nat. —

Vorgelegt dem Promotionsausschuss
des Fachbereichs 2 (Chemie/Biologie)
der Universität Bremen

von
Monika Biener

Bremen, November 2004

This thesis is based on the following papers, which will be referred to in the text by their Roman numerals:

I) Heteroepitaxial growth of novel MoO_3 nanostructures on Au(111)
Monika M. Biener, Cynthia M. Friend,
Surf. Sci. **559**, L173 (2004)

II) Growth of nanocrystalline MoO_3 on Au(111) studied by in-situ STM
Monika M. Biener, Juergen Biener, Richard Schalek, Cynthia M. Friend,
J. Chem. Phys., in press

III) Novel synthesis of two-dimensional TiS_2 nanocrystals on Au(111)
Monika M. Biener, Juergen Biener, Cynthia M. Friend,
J. Chem. Phys., in press

IV) Surface alloying of immiscible metals: Mo on Au(111) studied by STM
Monika M. Biener, Juergen Biener, Richard Schalek, Cynthia M. Friend,
submitted to Phys. Rev. B

V) Revisiting the S-Au(111) interaction: static or dynamic?
Monika M. Biener, Juergen Biener, Cynthia M. Friend,
submitted to Langmuir

VI) Sulfur induced corrosion of Au(111) studied by real-time STM
Monika M. Biener, Juergen Biener, Cynthia M. Friend,
submitted to J. Am. Chem. Soc.

VII) Enhanced transient reactivity of O-sputtered Au(111) surfaces
Monika M. Biener, Juergen Biener, Cynthia M. Friend,
in preparation

VIII) Tuning electronic properties of novel metal oxide nanocrystals using interface interaction: MoO_3 monolayers on Au(111)
Su Ying Quek, Monika M. Biener, Juergen Biener, Cynthia M. Friend, Efthimios Kaxiras,
submitted to Surf. Sci. Lett. (As I am not the main contributor of this combined theory-experimental paper, it is not included in my thesis)

Contents:

1. Introduction

Novel properties of a material arise by reducing the length scale from macroscopic to the nanometer scale. This effect can be exploited to engineer materials with unique electronic[1,2], catalytic[3,4], optical[5] and mechanical[6,7] properties. Due to the immense technological potential of length-scale engineering, the research in the field of nanoparticles, ultrathin films and nanocrystalline materials has expanded dramatically in recent years. The goal is to develop materials with unique properties that meet the design requirements for a particular technology.

The growing field of nanocatalysis explores the catalytic activity due to size effects in the nanometer scale and aims at catalyst design on the atomic scale. Gold nanoparticles, for example, are chemically very active[3,4] if dispersed on metal oxides in contrast to gold in the bulk phase. Molybdenum clusters on gold exhibit a very low activity towards O_2 and CO[4,8], whereas bulk Mo dissociates CO and O_2 below 300 K[9,10], providing another example. Hence, it is important to develop and control methods for synthesizing nanoscopic materials.

In this thesis, I will demonstrate that we are able to synthesize novel, nanocrystalline monolayer structures of MoO_3, TiS_2, MoS_2 and AuS on Au(111). The synthesis of well-defined, single layer structures on the nanometer scale is a first step towards the development of materials with novel chemical and physical properties.

Because of its apparent inertness gold was selected as a substrate material. As the most noble of all metals it is traditionally widely used in jewellery, however, due to its unique blend of properties gold has become increasingly important in industrial applications. For example, the high electronic conductivity in combination with corrosion resistance makes

gold-plated contacts an essential part in microelectronics. Due to its chemical inertness gold is also an attractive substrate for surface science studies, for instance gold films are widely used as substrate for alkanethiol-based self-assembled monolayers (SAMs)[11-13].

The noble character of Au does not imply a general inability to form stable bonds with non-metals but is rather a consequence of high reaction barriers towards dissociation reactions[14]. For example chemisorbed oxygen on Au(111) is stable up to 500 K[15] indicating a rather strong interaction. Au can even exhibit a high catalytic reactivity if the reaction barrier towards dissociation is modified by interaction with a suitable substrate as demonstrated in the case of dispersed gold nanoparticles supported on metal oxide surfaces[3,16]. Indeed, Au-based catalysts are being developed for industrial oxidation processes. In the course of this thesis I will demonstrate that the Au(111) surface is anything but a static, inert surface. I will discuss various levels of interaction between the Au(111) surface and various adsorbates and adsorbed monolayer structures. Specifically, I will discuss the role of surface stress, the enhanced reactivity of under-coordinated Au atoms such as step edge atoms or surface atoms, and surface alloying. We will see that:

- The surface stress of the Au(111) surface is modified by small amounts of adsorbed sulfur causing a lifting of the herringbone reconstruction (chapter 3.2.).
- High sulfur coverages lead to the corrosion of Au(111) surfaces: the formation of stable Au-S bonds drives a restructuring of the surface landscape and formation of a 2D AuS phase (chapter 5.2.).
- The step edges of the Au(111) surface are reactive sites for decomposition of $Mo(CO)_6$ (chapter 4.2.).
- Place exchange with physical vapour deposited Mo occurs at the elbow sites of the herringbone reconstruction (chapter 4.2.).
- Mo deposited on Au(111) at elevated temperatures leads to formation of a substitutional surface alloy, although the two elements are immiscible (chapter 4.3.).
- Bond lengths and bond angles within nanocrystalline MoO_3 structures on Au(111) are distorted to fit the symmetry of the underlying gold substrate, indicating a rather strong interaction between Mo and Au (chapter 5.1.).

- The orientation of triangular TiS_2 nanocrystals on Au(111) surfaces is affected by a strain field interaction at the TiS_2-Au interface (chapter 5.3.).
- Au clusters exhibit a high reactivity towards SO_2 decomposition (chapter 6.).

This list of examples demonstrates that the Au(111) surface can be a very dynamic rather than a static substrate.

2. Experimental

The experiments were performed in two different ultrahigh vacuum (UHV) systems, which I will refer to as system A and system B.

System A is a homebuilt UHV system equipped with a homebuilt "beetle"-type STM, as well as with commercial instrumentation for Auger electron spectroscopy (AES), low energy electron diffraction (LEED) and mass spectroscopy (Figure 1). The typical base pressure of the system is $4x10^{-10}$ mbar. To enable easy STM tip change the chamber was designed with a gate valve between the main chamber and the STM z-manipulator. This allows one to change the tip without opening the main chamber, a procedure frequently performed in order to achieve high quality STM resolution. Details of the chamber are published elsewhere[17,18].

The Au(111) sample was typically cleaned by repeated cycles of sputtering (30 min/1000 eV/ ~5 μA) at 300 K and annealing (10 min at 700 K followed by 60 min at 600 K) until no contaminants were detected by means of AES. Following this procedure, a LEED pattern characteristic of the Au(111)-(22x√3) reconstruction[19] was observed. The "herringbone" reconstruction was also observed by STM. The optimum sputter position was

initially determined by measuring a sputter profile (sputter current versus x-y position).The sample is radiatively heated, and the temperature was monitored using a Cr-Al thermocouple.

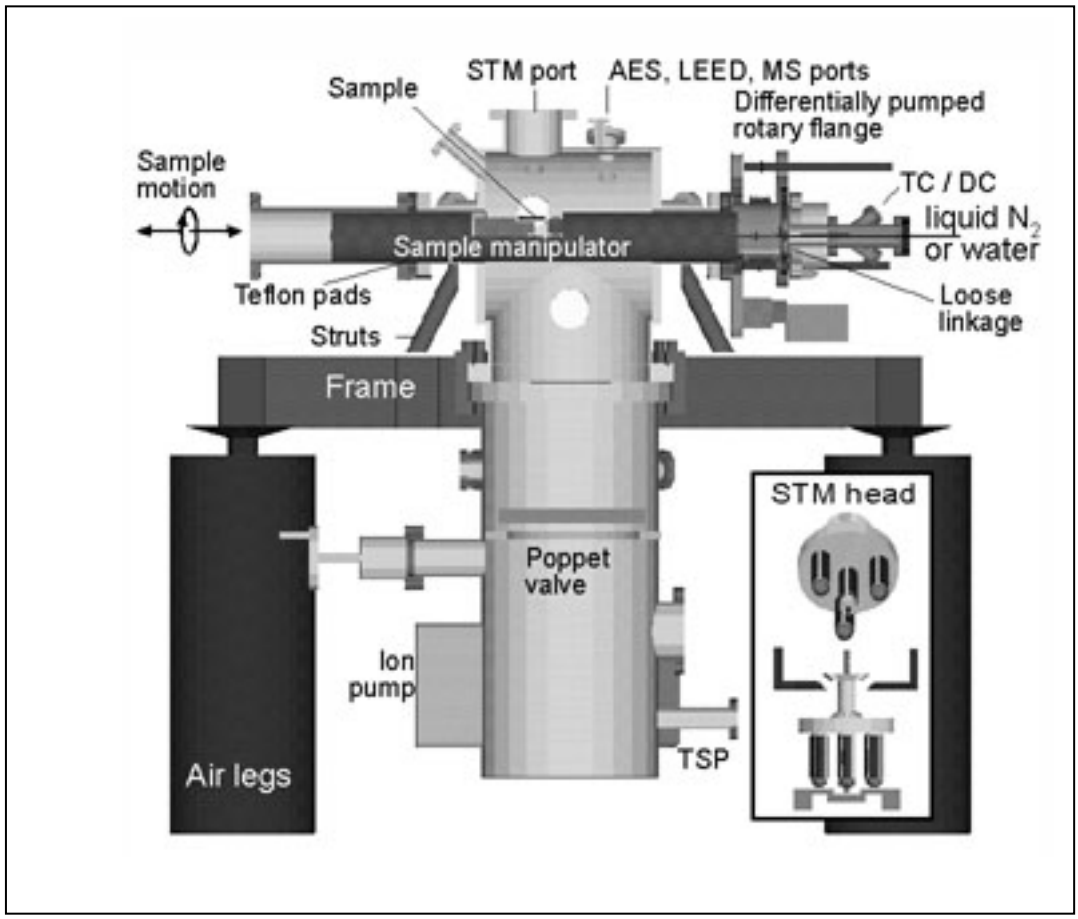

Figure 1: A cross-section of the UHV STM system A showing the chamber, the beam frame and the air legs. The top half contains surface science analysis equipment and the sample manipulator. The inset shows a schematics diagram of the STM head. (Figure taken from ref [18])

I designed and installed a new dosing system for $Mo(CO)_6$. The sample container as well as all other parts of the dosing system were made of stainless steel to reduce contaminations and to eliminate light-induced decomposition of the precursor. The partial pressure of $Mo(CO)_6$) in the gas line was frequently checked using a Pirani gauge. In order to minimize thermally-induced decomposition of the $Mo(CO)_6$ precursor, the Pirani head can be separated from the main gas line by a valve. $Mo(CO)_6$ was initially purified by several freeze-pump-thaw cycles, and NO_2 (Matheson) and SO_2 (Matheson) were used as received. All gas lines were evacuated and freshly filled before each dose. The sample was exposed to the

reactants by backfilling the chamber, and exposures are given in uncorrected ion gauge readings in units of Langmuir (1L=10^{-6} torr•s). STM images were collected either at room temperature or at elevated temperatures using commercial $Pt_{0.8}$ $Ir_{0.2}$ tips (Molecular Imaging). Scan dimensions were calibrated by imaging the unit cell of the Au(111) surface.

System B is a commercial system (Omicron) with separate compartments for sample preparation and sample characterization. A transfer mechanism allows the operator to move the sample between both compartments without breaking the vacuum (Figure 2). The analysis chamber is equipped with a variable–temperature STM/AFM (Omicron), AES (Omicron), and LEED (Omicron), and has a typical base pressure of $5x10^{-11}$ mbar. The STM system is designed to collect Z-channel (topography) and I-channel (current) images simultaneously. The preparation chamber is equipped with a differentially-pumped ion sputter gun (Omicron), an electron-beam evaporator (Omicron, EFM 3), a quartz thickness monitor (Inficon, XTM/2), an optical pyrometer (Omega), and a residual gas analyzer.

The Au(111) sample was cleaned by cycles of Ar sputtering at room temperature (60 min / 1000 eV / 4 μA) and annealing (10 min at 900 K followed by one hour at 600 K) until contaminations were no longer detected by means of AES. The sample was heated by a PBN heating element, and the temperature was monitored using an optical pyrometer calibrated against a thermocouple.

Metal (Titanium (Aldrich, 99.99%) and Molybdenum (Goodfellow, 99.9%)) was evaporated from rod material (Ti: 2.0 mm diameter, Mo: 1.5 mm diameter) using an electron beam evaporator (Ti: 800 V / 30 mA, Mo: 900 V / 65 mA). The deposition rate was monitored continuously by a flux monitor measuring the ion flux, which is proportional to the flux of evaporated atoms. Initially the deposition rate was calibrated using a quartz thickness monitor.

NO_2 (Matheson) and SO_2 (Matheson) were used as received. All reagents were admitted to the sample by backfilling the chamber. The purity of all gases was periodically checked with a residual gas analyzer, and all gas lines were evacuated before each dose.

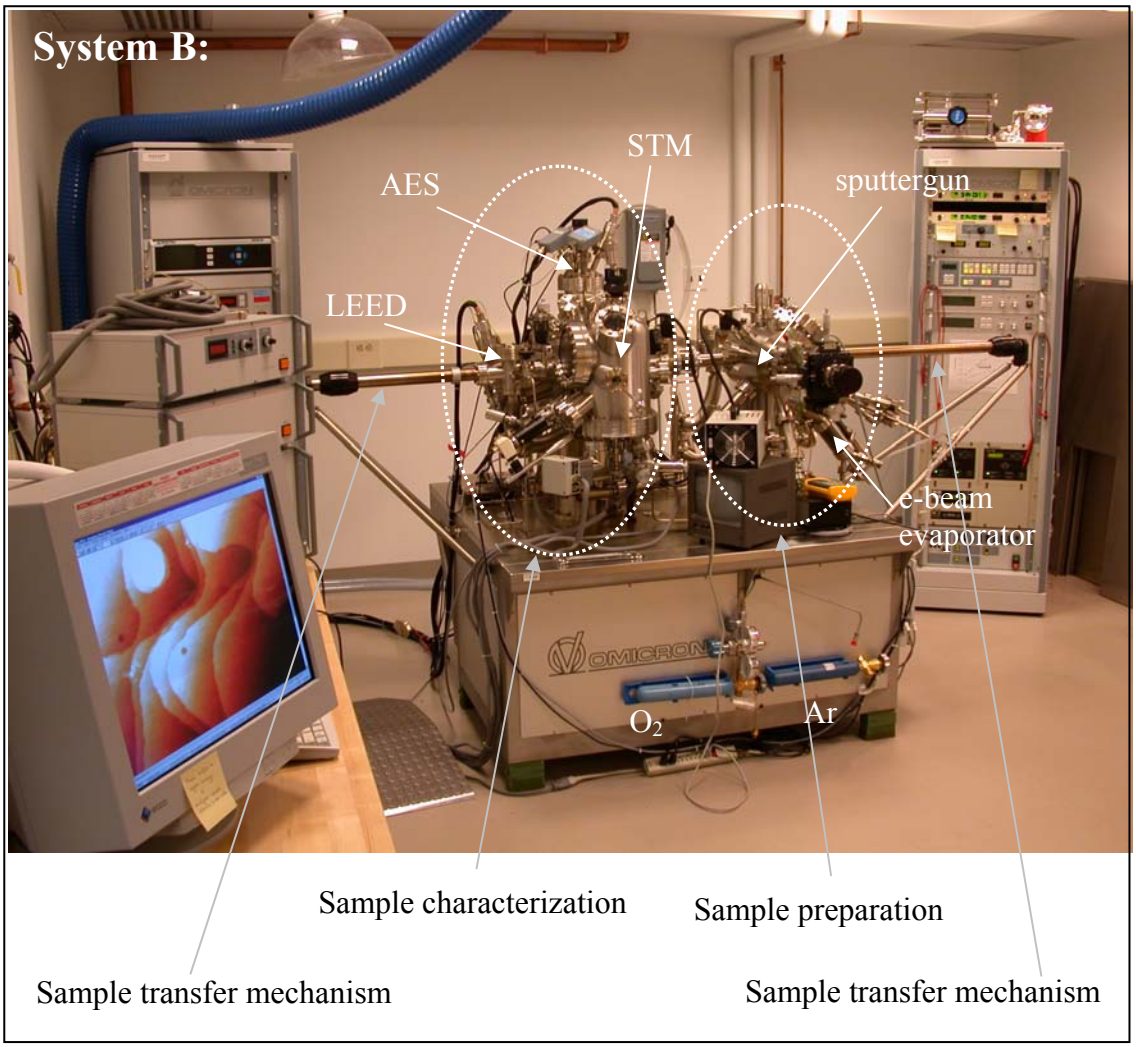

Figure 2: A picture of the Omicron UHV chamber (System B)

More details of the experimental parameters can be found in the experimental section of each paper. The experiments for the papers I, V and VI were performed in system A, whereas all experiments involving physical vapor deposition of a metal (papers II, III, IV) and the experiments for paper VII were carried out in system B.

3. The Au(111) surface as a substrate

3.1. The herringbone reconstruction

Surface atoms are generally under-coordinated with respect to their bulk phase. This gives rise to a charge redistribution at the surface which in turn causes the generally observed positive (tensile) stress of a clean metal surfaces[20]. The surface layer often rearranges in order to reduce this tensile surface stress. This leads to a surface structure that differs from the bulk terminated surface structure and is called surface reconstruction.

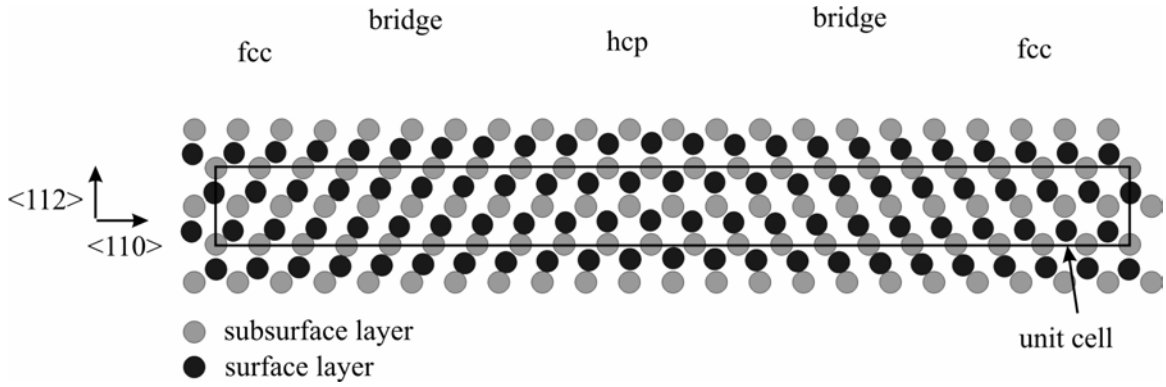

Figure 3: Schematic illustrating the incorporation of additional 4.55% Au atoms (2 per unit cell) in the surface layer and the resulting transition between fcc and hcp stacking areas.

For example, the characteristic "herringbone" reconstruction of the Au(111) surface is caused by the presence of tensile surface stress which drives the incorporation of an additional 4.55% of Au atoms in the surface layer. This leads to a uniaxial contraction along the close-packed <110> directions (Figure 3): 23 surface atoms along the <110> direction are in registry with 22 atoms of the subsurface layer[21,22]. The resulting fcc and hcp stacking

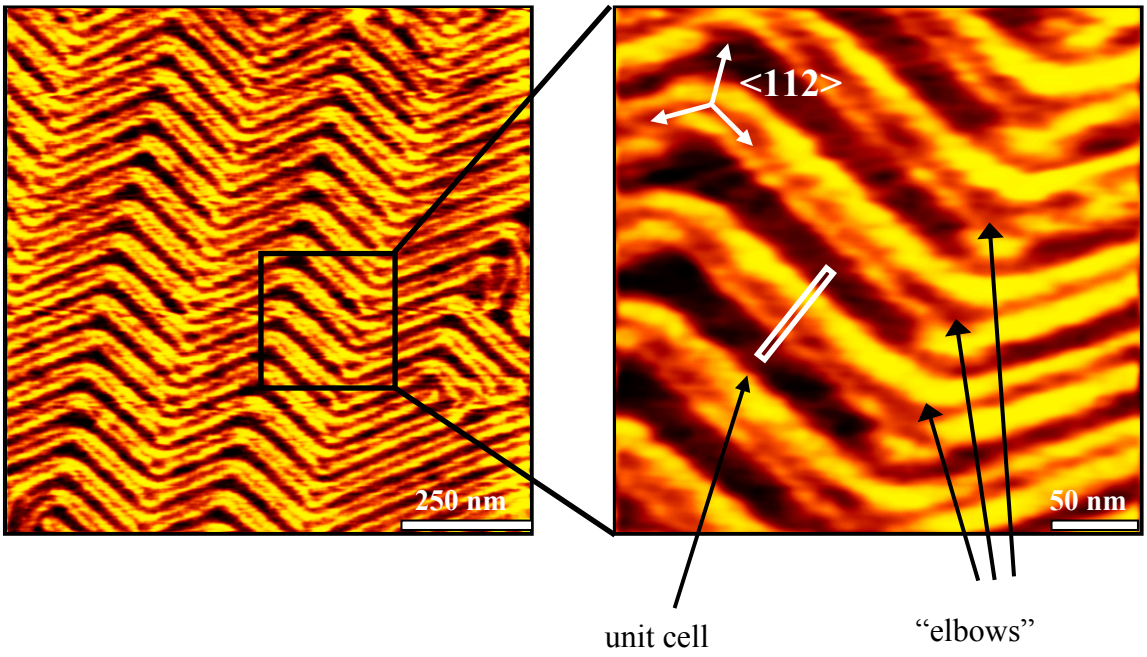

Figure 4: STM image of the clean reconstructed Au(111) surface.

regions are separated by rows of bridging Au atoms which appear as ridges in STM images (Figure 4) and are aligned with the <112> directions. A regular arrangement of rotational domains of uniaxially contracted areas allows for a more isotropic stress distribution and gives rise to the observation of the characteristic zig-zag (chevron or herringbone) pattern, where the bending points (elbows) form a periodic network of dislocations. Au atoms at these elbow sites are under-coordinated and thus can be employed as preferential nucleation sites. The Au(111) surface is thus an ideal template for self-organized growth of nanostructures (see chapter 4). The Au(111)-(√3x22) herringbone reconstruction is also revealed by the presence of characteristic satellite spots in the LEED pattern. The arrangement of the herringbone dislocation lines in the vicinity of the steps depends drastically on the step microstructure[23].

3.2. Sulfur induced modification of the surface stress: lifting of the herringbone reconstruction

(Relevant papers: V, VI)

Surface stress is crucial to various phenomena of a clean surface, such as surface reconstruction, surface diffusion, and surface morphology. It also plays an important role in adsorbate-surface interactions as it can control e.g. the shape or orientation of adsorbate structures as we will see in chapters 5.1 and 5.2.

Surface stress in general can be modified by interaction with adsorbates. One example for adsorbate-induced modification of surface stress is the effect of S on the Au(111) surface: Sulfur reverses the stress of the Au(111) surface from tensile to compressive as revealed by the ejection of Au atoms and the lifting of the herringbone reconstruction (Figure 5). The origin of adsorbate-induced compressive surface stress can be understood in terms of a charge transfer from substrate surface bonds to the adsorbate atoms[20]. This in turn drives the ejection of surface atoms, which agglomerate at ascending step edges. It is quite remarkable that a sulfur coverage of only 0.1 ML is sufficient to completely lift the herringbone reconstruction at room temperature and thus drives a lateral expansion of the Au surface layer by ~4%. The lifting of the Au(111) reconstruction by small amounts of strongly (specifically) adsorbed anions is also a common observation in electrochemical environments[24].

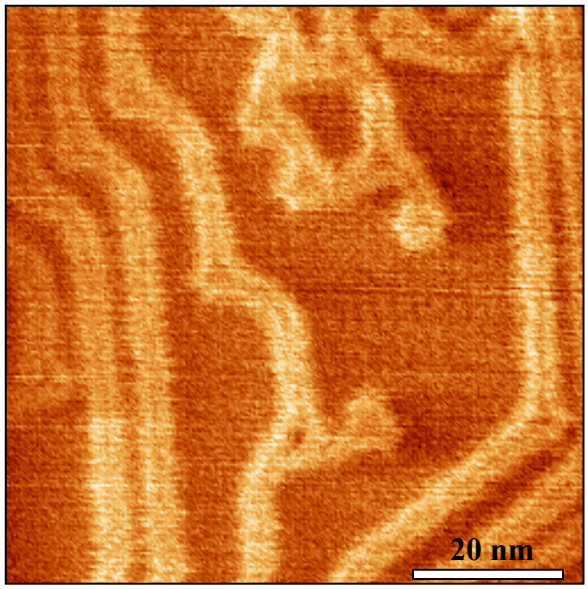

Figure 5: S-induced modification of the surface stress on the Au(111) surface: the herringbone reconstruction is partly lifted.

4. Deposition of metals on Au(111)

As outlined in the previous chapter, the regular array of dislocations of the herringbone reconstruction can be exploited as a template for self-organized growth of metal nanostructures. In my thesis work, I investigated the synthesis of Mo nanoclusters on the Au(111) surface using two different preparation methods: Physical Vapor Deposition (PVD) and Chemical Vapor Deposition (CVD). I will shortly describe these two methods and then compare the experimental results for PVD and CVD of Mo on Au(111).

4.1. Methods: CVD, PVD

Chemical Vapor Deposition (CVD) is a widely used method for depositing thin films of various materials on a substrate. In a typical CVD process one or more volatile precursors are dosed onto a substrate from the gas phase. Chemical reaction or decomposition of the precursors on the surface leads to deposition of the desired material. Heat or radiation is often used to promote a reaction/decomposition.

We used $Mo(CO)_6$ as a precursor to deposit small amounts (less than a monolayer) of Mo on the Au(111) surface (Figure 6, left panel). Thermal energy is necessary to promote the decomposition of the precursor. We chose a substrate temperature of 450 K as the apparent deposition rate decreases at either higher or lower temperatures than 450 K. At temperatures below 450 K the thermal energy imparted to the metal carbonyl is insufficient to promote its decomposition. Our explanation for the lower deposition rate observed at temperatures above 450 K is that the surface lifetime of the $Mo(CO)_6$ precursor decreases due to an increased desorption rate.

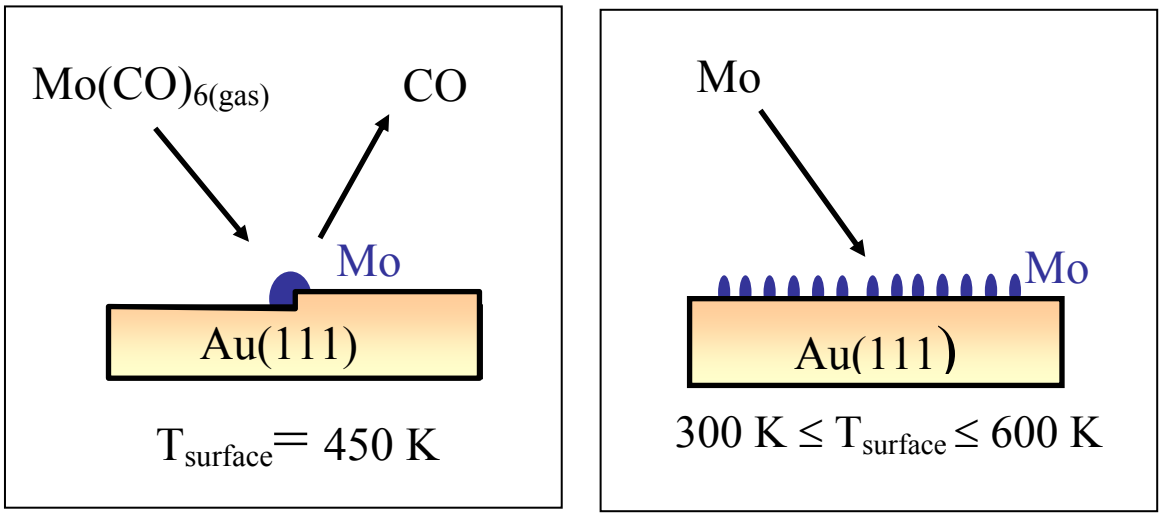

Figure 6: Schematic representation of the two preparation methods used to deposit Mo on the Au(111) surface: CVD (left panel) and PVD (right panel). The preparation method affects the distribution of the Mo clusters: CVD leads to step edge decoration, PVD to nucleation at the elbow sites.

Physical Vapor Deposition (PVD) is another method for thin film deposition, wherein the atoms or molecules of a substance are thermally evaporated in vacuum and deposited onto the substrate without any chemical reaction. In this instance, the rate of deposition is largely controlled by the flux of Mo from the source and is, therefore, relatively insensitive to the substrate temperature during deposition. However, the surface temperature does affect the mobility and, therefore, the distribution of the metal atoms on the surface during deposition. The wider range of deposition temperatures generally available in the PVD process renders it more versatile for materials growth. On the other hand, changing the metal source is not as convenient in PVD.

We used PVD to deposit submonolayer coverages of Mo on Au(111) at various substrate temperatures (Figure 6, right panel). The substrate temperature strongly influences the resulting Mo cluster distribution, as we will see in chapter 4.3.

4.2. Results: CVD versus PVD

(Relevant papers: I, IV)

Preferential nucleation of three-dimensional molybdenum nanoclusters at step edges is observed after dosing of $Mo(CO)_6$ onto the Au(111) surface maintained at 450 K (Figure 7, left panel). The distribution of Mo clusters suggests that the active sites for $Mo(CO)_6$ decomposition are related to step edges of the Au surface. Indeed, small amounts of sulfur (< 0.1 ML) completely inhibit the decomposition of $Mo(CO)_6$ on the Au(111) surface. It is known that the most stable bonding sites for sulfur are located at the step edges of Au(111)[25], indicating that blocking the step sites inhibits dissociation of $Mo(CO)_6$. These results, therefore, indicate that Au atoms at the step edges promote the decomposition of $Mo(CO)_6$; i.e., the Au surface is not just a "spectator" providing thermal energy. The apparent deposition rate increases with increasing Mo coverage, suggesting that deposited Mo auto-catalyzes further $Mo(CO)_6$ decomposition.

In contrast, well-ordered arrays of Mo nanoclusters form on the reconstructed Au(111) surface using PVD to deposit Mo at room temperature (Figure 7, right panel). The elbow sites of the herringbone reconstruction of the Au(111) surface thereby serve as selective nucleation sites. A preferential nucleation of metals at the elbow sites of the

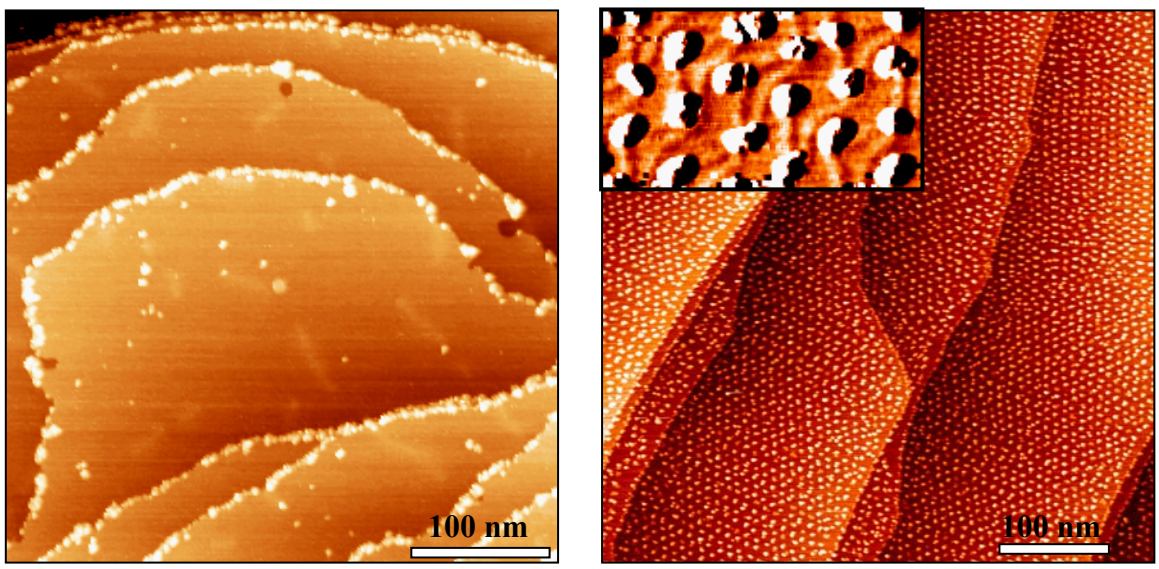

Figure 7: STM images after CVD (left panel) and PVD (right panel) of Mo on Au(111). CVD leads to a preferential step edge decoration, whereas PVD results in a regular array of Mo clusters which nucleate at the elbows (inset).

reconstructed Au(111) surface is a common phenomenon and was previously observed for other metals[26-28]. It has been suggested that the nucleation is initiated via a site selective place exchange by impinging metal atoms at the elbows sites[29], i.e. the formation of a local surface alloy. The elbow sites are expected to be the most reactive sites for place exchange due to the under-coordinated nature of gold atoms at these sites.

By choosing the Mo deposition method (CVD vs. PVD) we are able to control the distribution of the resulting Mo nanostructures. The difference in the Mo cluster distribution reflects the different active sites of the Au surface which are involved in the deposition process. In case of CVD, $Mo(CO)_6$ decomposes preferentially at step edges, whereas in case of PVD a place exchange of Mo with Au atoms takes place at the elbow sites of the reconstruction.

4.3. Mo-Au surface alloying at elevated temperatures

(Relevant paper: IV)

Surface alloying becomes important if Mo deposition via PVD is performed at elevated temperatures (525 K and above). This is inferred from the evolution of a serrated step-edge morphology (Figure 8) caused by attachment of ejected Au atoms, and a decrease of the Mo surface coverage, as well as the appearance of vacancy islands in the Au surface after chemically-driven dealloying of Mo (see chapter 5.1). The formation of a Mo-Au surface alloy is quite remarkable as Mo and Au are bulk immiscible.

Mo-Au surface alloying is an activated process as demonstrated by a decrease in Mo surface coverage (increase of alloying) with increasing deposition temperature: the fraction of the deposited Mo found in Mo clusters after deposition at 600 K is ~ 30% of the corresponding value after deposition at 300 K. As the Mo/Au AES peak ratio differs only by 20% (deposition at 600 K vs. deposition at 300 K) the majority of the alloyed molybdenum seems to be confined near the surface. Once Mo clusters are formed via deposition at room temperature, they are, however, resistant to alloying up to at least 600 K. This suggests that the Mo-Mo interactions are strong enough to suppress the formation of an alloy. Only

individual atoms impinging on the surface at or above 525 K can surmount the activation barrier for surface alloying.

In the case of CVD, the decomposition of the precursor species ($Mo(CO)_6$) is auto-catalyzed by Mo already deposited via thermal decomposition, and the Mo atoms released are thus immediately stabilized by formation of Mo-Mo bonds. Thus surface alloying is not expected - and not observed - for Mo deposited via CVD on Au(111).

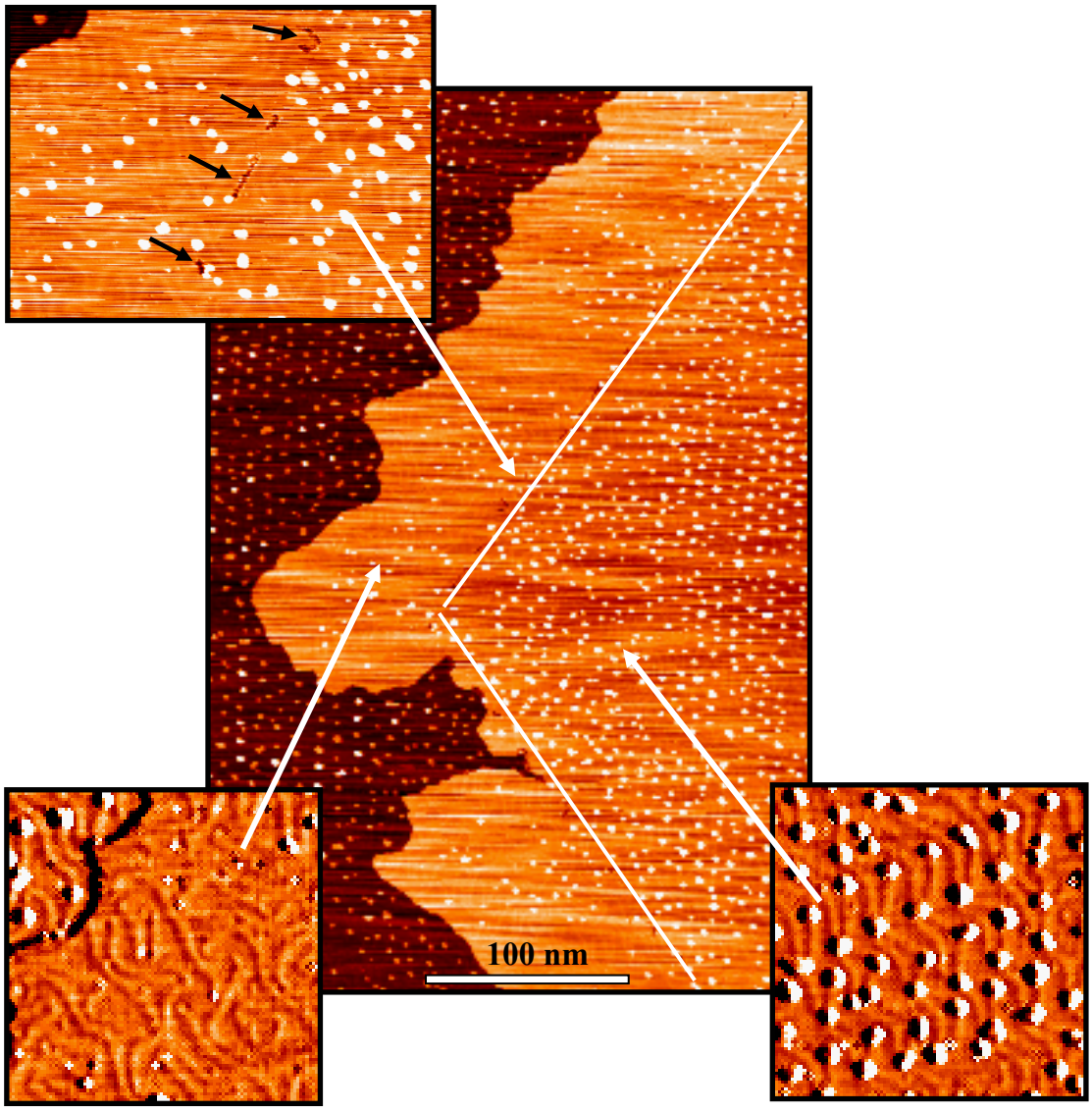

Figure 8: Surface alloying is observed during PVD of Mo on Au(111) at (or above) 525 K. The insert top left shows a linear vacancy line defect which seems to indicate the position of the original step edge.

5. Two-dimensional metal oxide and metal sulfide structures on Au(111)

5.1. Synthesis and characterization of two-dimensional MoO_3 nanocrystals

(Relevant papers: I, II, VIII)

Transition metal oxides are a technologically very important class of materials due to their interesting electronic and catalytic properties. For example, transition metal oxides are used in the conversion of hydrocarbons to oxygenates that are of interest as alternative fuels and as building blocks for other chemicals. Molybdenum trioxide specifically is known to promote the partial oxidation of methane to formaldehyde[30-33]. Transition metal oxides have a wide range of chemical, electronic and optical properties that depend on stoichiometry and size scale. For example, bulk MoO_3 is a semiconductor with a bandgap of 2.8 eV; however, states are introduced in the gap when point defects due to loss of oxygen are introduced[34]. Catalytic activity is often attributed to the presence of oxygen vacancies associated with edge sites of the material[35].

We developed a synthetic procedure that yields novel nanocrystalline, monolayer islands of MoO_3 on Au(111). Both CVD and PVD can be used to deposit Mo clusters on the surface. The Mo nanoclusters can be fully oxidized via subsequent exposure to NO_2 at elevated temperatures (450 K to 600 K), as inferred from the oxidation state (+6) as determined by X-ray photoelectron spectroscopy (Figure 9)[36]. These 2D nanocrystalline MoO_3 islands exhibit a large "surface to volume" ratio and are thus very promising candidates for catalysis and sensor applications.

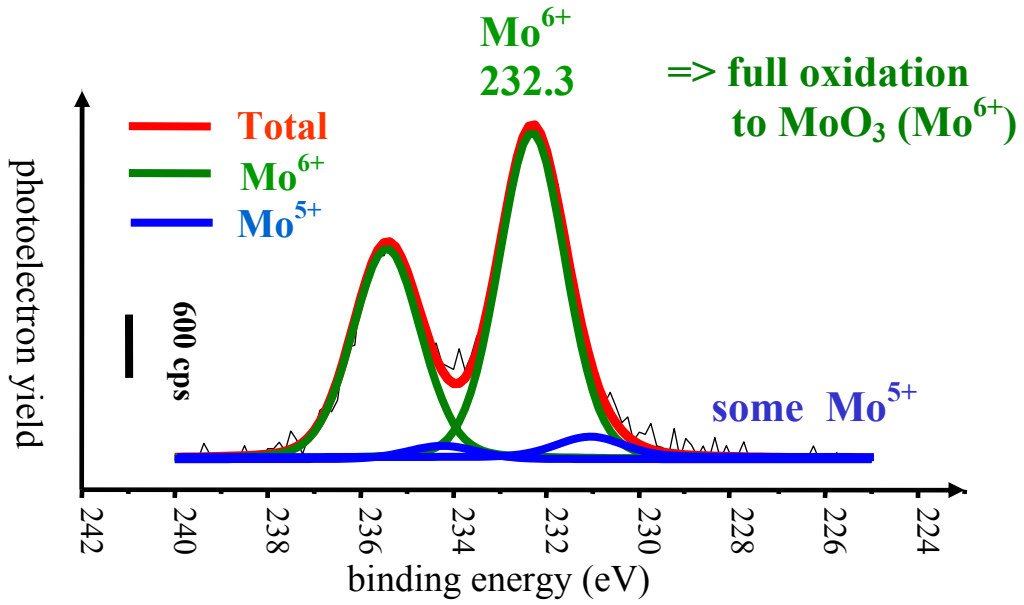

Figure 9: XPS spectra of MoO_3 islands, prepared via CVD of $Mo(CO)_6$ and oxidation by NO_2. Mo is fully oxidized towards MoO_3 [36].

The in-situ growth experiments of the MoO_3 islands indicate a non-local, long-range mass transport of MoO_3 precursor species from oxidized Mo clusters to growing MoO_3 islands. Oxidized Mo clusters thereby serve as both reservoir of mobile MoO_3 species and as nucleation sites. However, as the density of MoO_3 islands is much lower than the density of

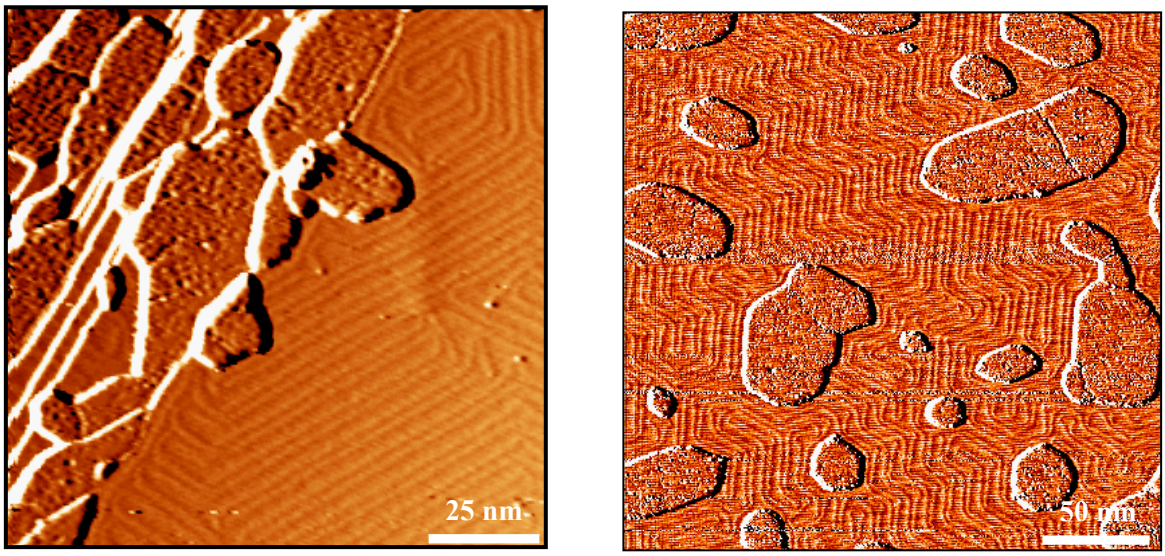

Figure 10: STM images of 2D well ordered MoO_3 islands on Au(111). Preparation via CVD (left panel) leads to step edge decoration whereas PVD (right panel) results in terrace decoration.

Mo clusters prior to oxidation, the majority of the Mo clusters must dissolve during oxidation via formation of mobile MoO_3 species. However, the spatial distribution of the Mo clusters prior to oxidation still controls the distribution of the growing MoO_3 islands: MoO_3 islands form *on* Au(111) terraces if the Mo clusters were prepared by PVD, whereas oxidation of Mo clusters at step edges prepared by CVD leads to the growth of MoO_3 islands at step edges (Figure 10).

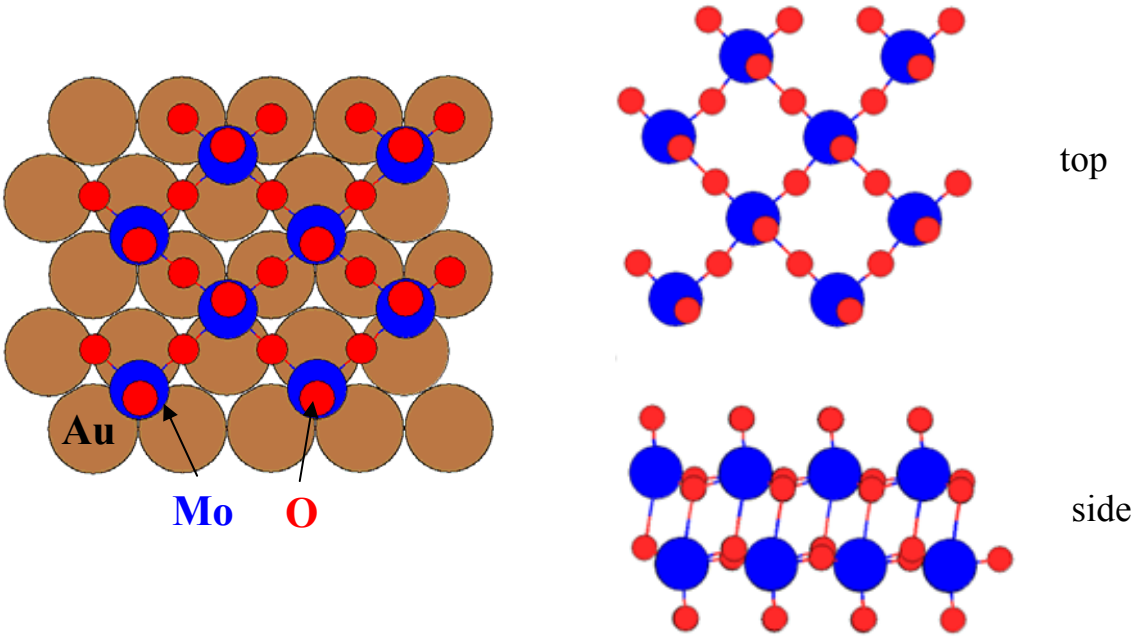

Figure 11: Structure model of single-layer MoO_3 on Au(111) (left panel) versus the structure of bulk MoO_3 (right panel) which consists of bilayers.

These MoO_3 islands reflect the symmetry of the underlying gold surface as inferred from the observation of a c(4x2) unit cell by both, high resolution STM and LEED. The structure of single-layer MoO_3 islands on Au(111) differs from the bilayer structure of bulk MoO_3[37], and can be explained in terms of an ordered, two-dimensional array of interacting MoO_3 entities (Figure 11). This is consistent with associated density functional theory calculations (paper VIII). Furthermore, the calculated local density of states reveals that the single layer MoO_3 on Au(111) is semi-metallic whereas bulk MoO_3 is known to be semi-conducting.

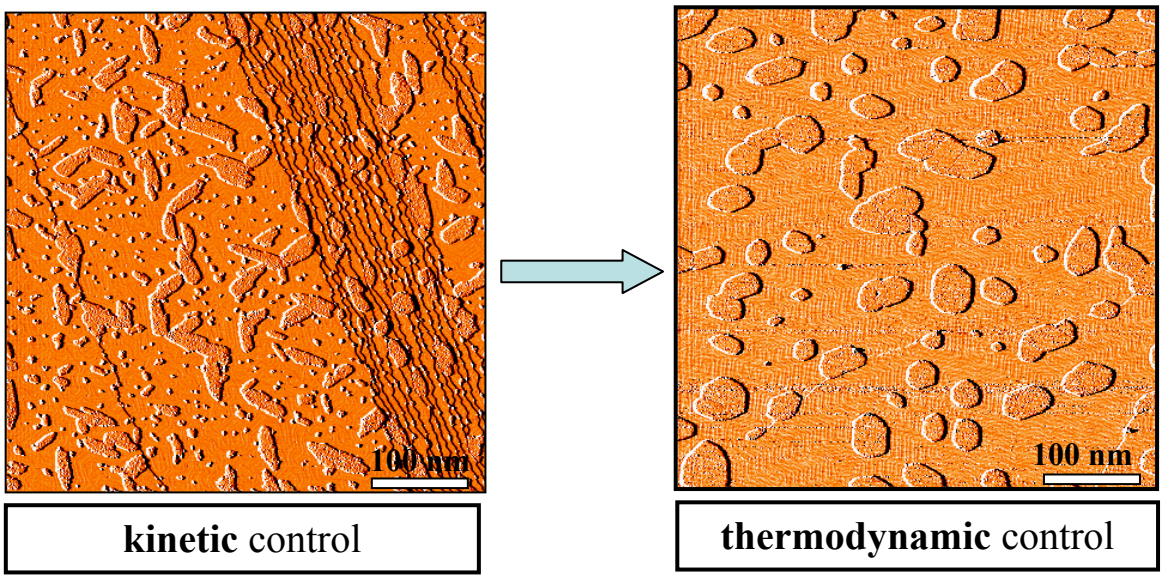

Figure 12: Kinetic controls the morphology of MoO_3 islands prepared at 450 K (left panel). Subsequent annealing at 600 K leads to a more compact island shape and an increasing island size consistent with Ostwald ripening (right panel).

The morphology of the MoO_3 islands strongly depends on preparation conditions. For example, the oxidation temperature affects the growth kinetics of MoO_3 islands: diffusion of MoO_3 precursor species is kinetically controlled at 450 K, which leads to an irregular shape of MoO_3 islands with a high aspect ratio. With further annealing the islands change in size and shape via Ostwald ripening (Figure 12). For deposition temperatures at 525 K or above we observe NO_2 induced dealloying of a Mo-Au surface alloy formed during Mo deposition. This, in turn, leads to the observation of "embedded" MoO_3 islands, which nucleate at steps of Au vacancy islands (Figure 13).

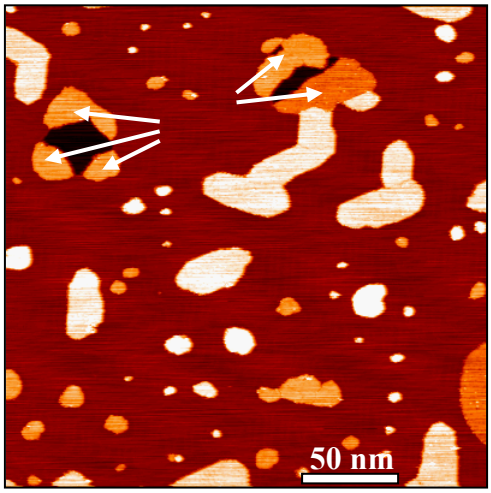

Figure 13: Embedded MoO_3 islands (indicated by arrows) are observed after NO_2 induced dealloying of Mo.

MoO_3 islands on Au(111) are partially reduced by annealing to 650 K and above. This is concluded from the observation of shear planes (Figure 14, left panel). The formation of shear planes can be explained by a local transformation from corner sharing to edge

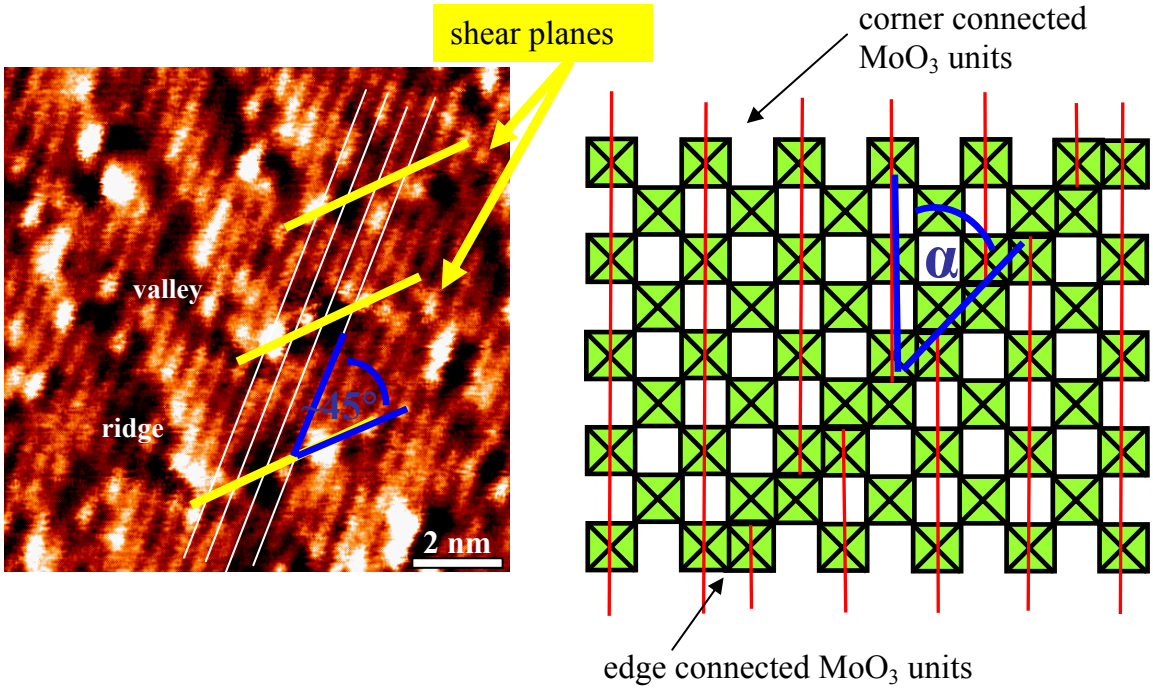

Figure 14: Shear planes develop upon annealing to 650 K. A possible structure associated with the formation of shear planes is shown schematically on the right. In this model, the shear planes are formed due to a local transformation of corner connected MoO_3 units to edge connected MoO_3 units, and corresponds to a partial reduction to Mo^{+5}.

sharing of MoO_3 units as illustrated in the schematic (Figure 14, right panel). This process eliminates ordered, linear arrays of oxygen vacancies which arise during the annealing step. Consistently, X-ray photoelectron spectroscopy (XPS) reveals a partial reduction of Mo^{+6} to Mo^{+5} during annealing[38], and thus the formation of oxygen vacancies. Reduction and oxygen vacancy formation upon thermal treatment is also observed for other transition metal oxides, e.g. TiO_2[39].

By controlling the shape and distribution of the MoO_3 islands on the surface, we are able to create different bonding environments that may affect the chemical and physical properties of the nanostructures. In particular, atoms at the periphery of the nanostructures have different bonding environments and coordination and may, therefore, have different chemical properties than in interior. Furthermore, we are able to manipulate the oxidation state in these oxides which may create reactive centers or change the catalytic properties of these materials.

5.2. S-induced corrosion of Au(111): formation of a two-dimensional AuS phase

(Relevant papers: V, VI)

The Au-S interaction is probably the most intensively studied interaction of Au surfaces with a non-metal as it is important in numerous technological applications: Au ore formation[40], thiol-based self-assembled monolayers SAMs[12, 13, 41] and corrosion inhibition, to name only a few. Furthermore, the increase of the electrical resistivity of thin gold films upon adsorption of certain sulfur-containing gases can be exploited to design sensors which allow the detection of minute traces of those species in gaseous mixtures[42,43]. However, an atomic level picture of the underlying mechanism for the resistivity change has not been given yet, although numerous studies on the S/Au(111) interaction have been performed in recent years[44-52].

A quite complex picture of the interaction of sulfur with Au(111) surfaces emerged, and a variety of S-induced surface structures was reported under different conditions. The majority of these structures were interpreted in terms of a static Au surface, where the positions of the Au atoms remain essentially unperturbed. For example, ordered arrays of rectangular structures were observed at higher S coverages and were predominantly attributed to adsorbed S_8 species[25,44,46-48]. In contrast, our studies demonstrate that the Au(111) surface exhibits a very dynamic character upon interaction with adsorbed sulfur: low sulfur coverages modify the surface stress of the Au surface leading to lateral expansion of the surface layer (see chapter 3.2); large-scale surface restructuring and incorporation of Au atoms into a growing two-dimensional AuS phase were observed with increasing sulfur coverage.

We used SO_2 as a source of sulfur. Only a small fraction of the SO_2 molecules that impinge on the surface decomposes and deposits sulfur. The oxygen released by SO_2 decomposition seems to be removed via an abstraction reaction with excess SO_2 (see chapter 6, paper VII). We used real-time STM to capture the dynamic rearrangement whilst forming a two-dimensional AuS phase: gold surface atoms are removed from regular terrace sites and incorporated into the growing gold sulfide phase resulting in the appearance of etch pits and irregularly shaped AuS islands (Figure 15).

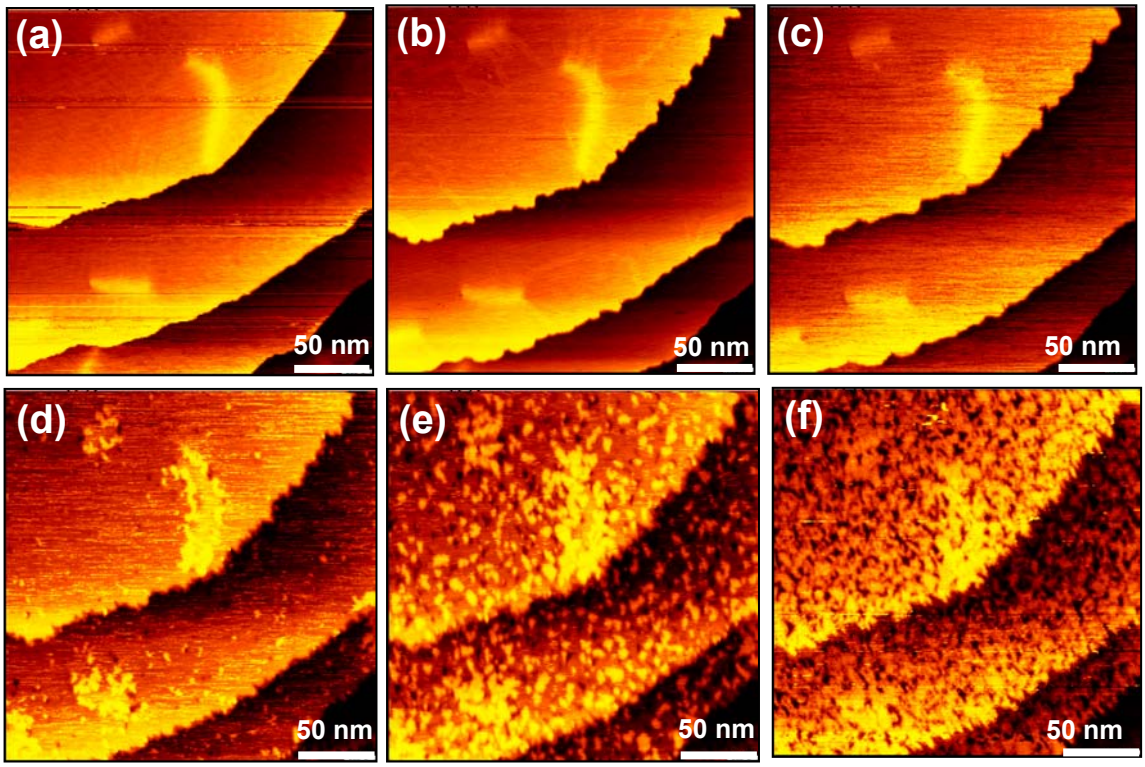

Figure 15: Real-time STM images capturing the dynamics of the S-induced Au corrosion at room temperature. (a) clean Au(111) surface, (b, c) lifting of the reconstruction, (d) monoatomic etch pits and small AuS clusters appear on terraces, and (e) their density increases with increasing S-coverage. (f) At a sulfur coverage of ~0.6 ML the Au surface is sulfur saturated.

Gold sulfide prepared at room temperature exhibits short range order; an incommensurate, long-range ordered AuS phase develops upon annealing at 450 K (Figure 16). The quasi-rectangular unit cell as revealed by LEED and high resolution STM (Figure 16, inset) resembles the earlier reported structures that were (mis)interpreted as regular arrays of adsorbed S_8 molecules. Temperatures higher than 525 K lead to decomposition of the AuS corrosion film. The formation of an ordered AuS phase via rapid step retraction rather than etch pit formation is observed during S-interaction with Au(111) surfaces *at* 420 K. This is captured by real-time STM imaging *at* 420 K (paper VI).

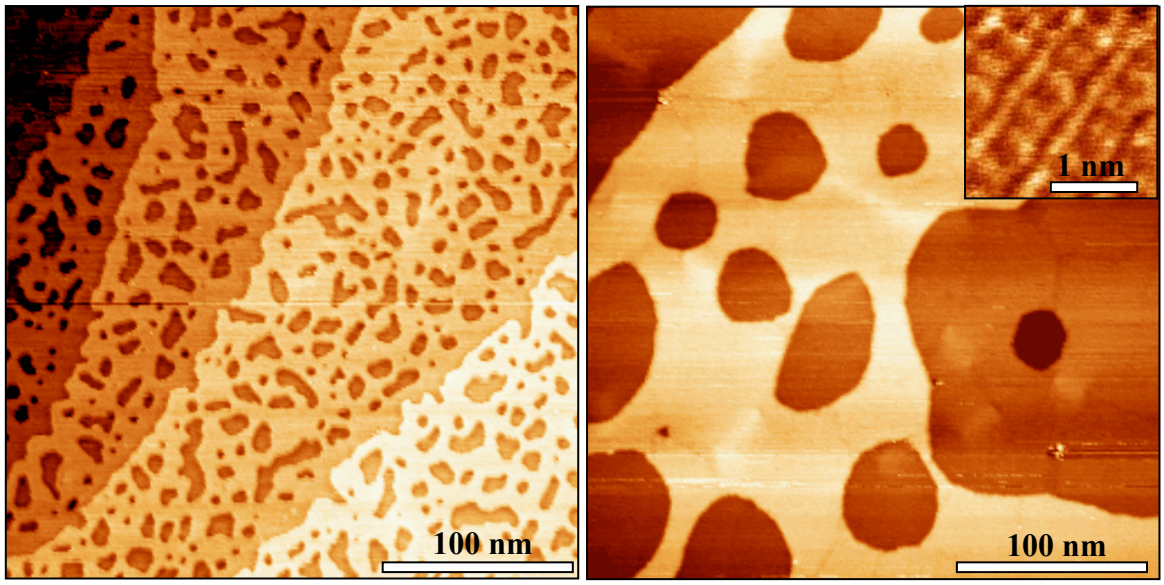

Figure 16: The AuS phase develops long-range order upon annealing. Left: after annealing to 420 K, right: after annealing to 450 K. The inset shows the unit cell structure.

Real-time STM provides us with nano-scale, time resolved information and reveals the very dynamic character of the Au(111) surface upon interaction with sulfur, such as large-scale mass transport and incorporation of Au atoms in a growing AuS phase. In view of the typically observed inertness of Au surfaces the S-induced corrosion and mobilization of Au atoms is surprising and sheds new light on the nature of the Au-S interaction.

The observed phenomena provide a basis for potential sensor or actuator applications: In materials with a high surface-to-volume ratio, such as nanoporous gold, the large S-induced expansion of the Au surface layer (4%) should lead to macroscopically observable dimension changes. Another interesting outlook is the synthesis of single-layer transition-metal disulfide structures using the 2D AuS phase as a sulfur reservoir. Using this approach, we are able to prepare single-layer MoS_2 and TiS_2 structures on Au(111), as described in the following chapter.

5.3. Novel approach to synthesize two-dimensional TiS_2 and MoS_2 nanocrystals

(Relevant paper: III)

Layered transition metal dichalcogenides with the general composition MX_2 (X = S, Se, Te) have many technological applications due to their highly anisotropic physical properties. These arise from strong covalent M-X intra-layer bonding contrasted by weak van-der-Waals inter-layer bonding. For example, mechanically flexible high-mobility field-effect transistors (FETs) can be based on transition metal dichalcogenides[53], MoS_2 is widely used as a solid lubricant and TiS_2 is one of the most effective cathode materials for high energy rechargeable batteries[54,55]. Furthermore, the layered structure of transition metal dichalcogenides allows the synthesis of fullerene-like and nanotube-like materials[56-58] with interesting electronic properties[59,60].

In the following we will focus on the synthesis of single-layer TiS_2 on Au(111). TiS_2 is a small-band-gap[61] semiconductor and a promising candidate for potential electronic applications due to its two-dimensional electronic structure. The structure of bulk TiS_2 can be regarded as hexagonally close-packed layers of S atoms with Ti occupying octahedral sites between every other pair of S layers. These S-Ti-S sandwiches are strongly bonded internally but only weakly coupled to each other by van-der-Waals forces.

Theoretical investigations predict that the electronic properties of an isolated S-Ti-S layer are different from those of the corresponding bulk material[62]. Similarly, single-layer TiS_2 on Au(111) may have different electronic properties than bulk TiS_2. Although thin films of TiS_2 have previously been prepared by chemical vapor deposition (CVD) or plasma assisted CVD using $TiCl_4$ and various S containing species such as H_2S and thiols as chemical precursors, these films are often amorphous and are contaminated with oxygen and carbon[63-67].

Here, we describe a novel, two step method for synthesis of single-layer nanocrystalline TiS_2 islands on Au(111) surfaces. First, a two-dimensional AuS overlayer

with a sulfur coverage of 0.5 ML is prepared as described in detail in the previous chapter. Second, Ti is deposited by PVD at room temperature on the AuS covered Au(111) surface which serves as a sulfur reservoir for TiS_2 formation.

Single-layer, nanocrystalline triangular TiS_2 islands develop during subsequent annealing to 670 K (Figure 17). These TiS_2 nanocrystals exhibit the same unit cell dimensions as bulk TiS_2 and are composed of S-Ti-S stacking units as the TiS_2 bulk phase. This is in contrast to single-layer MoO_3 on Au(111) where the MoO_3 lattice adapts to the geometry of the Au(111) surface (chapter 5.1.). In case of TiS_2 the islands are aligned with the substrate and form a Moire superlattice on the Au(111) which results from the coincidence of 5 TiS_2 units with 6 Au atoms based on both, STM and LEED. The energy cost of S not solely occupying high symmetry sites, such as the three-fold hollow sites, is obviously smaller than the energy necessary to distort the structure, as in case of MoO_3 (chapter 5.1), which is consistent with a van-der-Waals type of interaction.

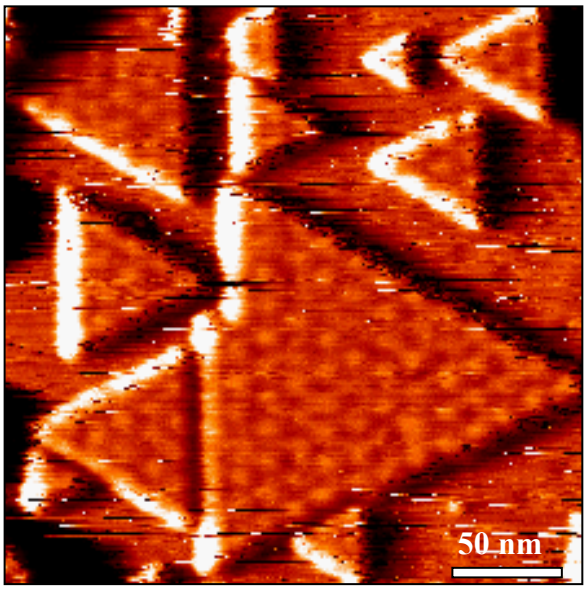

Figure 17: 2D nanocrystalline TiS_2 triangles on Au(111). A lattice mismatch between TiS_2 and Au leads to the formation of a Moire superlattice.

The triangular shape of the islands after annealing (to 670 K) is in contrast to the hexagonal symmetry of the S layers and indicates a preference for one of the two possible island edge terminations. The observation of two different island orientations rotated by 60 degrees with respect to each can be explained by the existence of different stacking sequences either within the S-Ti-S sandwich or at the TiS_2-Au interface, meaning that the S atoms in registry are either located in fcc or hcp sites. In any case, TiS_2 islands with the same orientation, i.e. the same stacking sequence, can easily coalesce, whereas TiS_2 with different stacking sequences remain separated by domain boundaries (Figure 17).

A preferred island orientation develops during further annealing at 800 K. This indicates that the interface environments of the two island orientations are energetically distinct. Indeed, STM reveals that the two island orientations interact differently with the surrounding herringbone pattern: islands of one orientation are surrounded by fcc areas of the Au(111) reconstruction whereas islands of the other orientation are surrounded by alternating hcp and fcc areas, respectively (Figure 18) . This indicates that the strain field of the Au(111) surface layer is affected by the TiS_2-Au interface environment. A similar effect was observed for close-packed steps on a clean Au(111) surface: the arrangement of the herringbone dislocation lines in the vicinity of the steps depends drastically on the step microstructure[23].

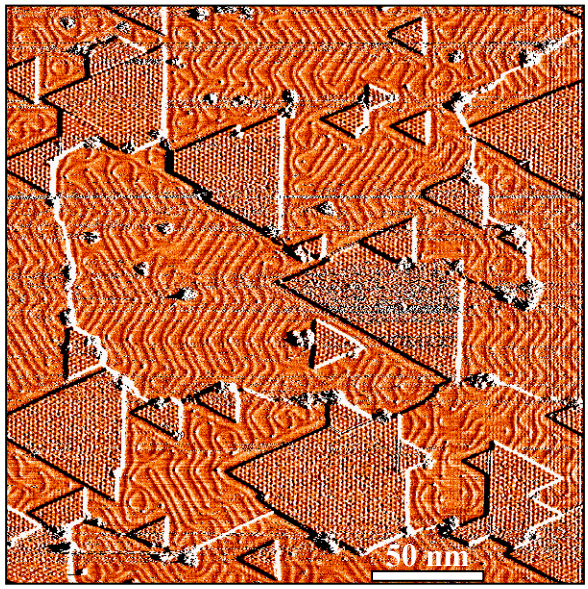

Figure 18: The TiS_2 islands grow in size and develop a preferential orientation during annealing at 800 K (triangle pointing to the left). The herringbone pattern is affected by the Au-TiS_2 interface environment: the dislocation lines run along the edges of islands pointing to the left and perpendicular to the edges of islands pointing to the right.

A novel metal rich TiS_{2-x} phase develops if Ti is deposited in excess (more than 0.25 ML which is the stoichiometric reaction condition). This new phase coexists with the TiS_2 phase and forms needle-like structures with a high aspect ratio (Figure 19). The unit cell is rectangular (inset).

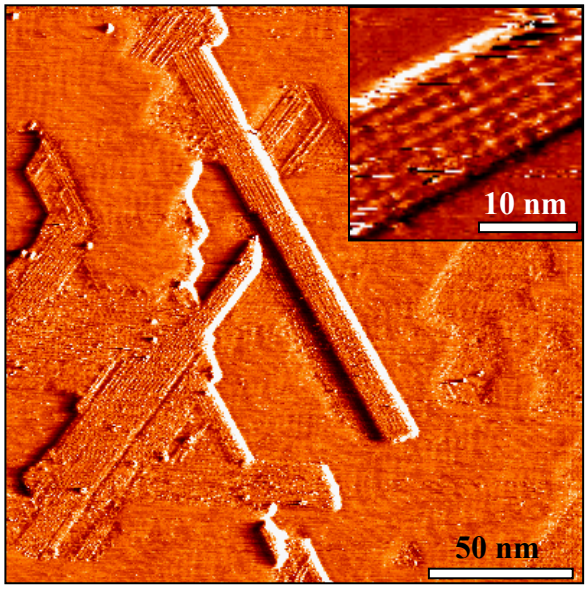

Figure 19: A novel metal rich TiS_{2-x} phase develops in case of excess Ti deposition. This structure exhibits a rectangular unit cell (inset).

MoS_2 forms nanocrystalline islands on Au(111), very similar to those described above. Helveg et.al.[68] first reported the synthesis of ~30 Å wide triangular MoS_2 islands on Au(111) by deposition of Mo in a H_2S ambient. Atomic resolution STM images revealed that the single layer MoS_2 islands exhibit the structure of bulk MoS_2 with a characteristic bright brim along the edges. A MoS_2 island with the bulk structure of MoS_2 should give rise to the observation of a "9 on 10" coincidence lattice. However, a Moire pattern was not observed as the coincidence superlattice cell is larger than the island size of ~ 30 Å. Using the same approach as for the synthesis of TiS_2 - i.e. physical vapor deposition of Mo onto AuS - we synthesized larger MoS_2 crystallites on Au(111) which indeed produce the expected Moire pattern.

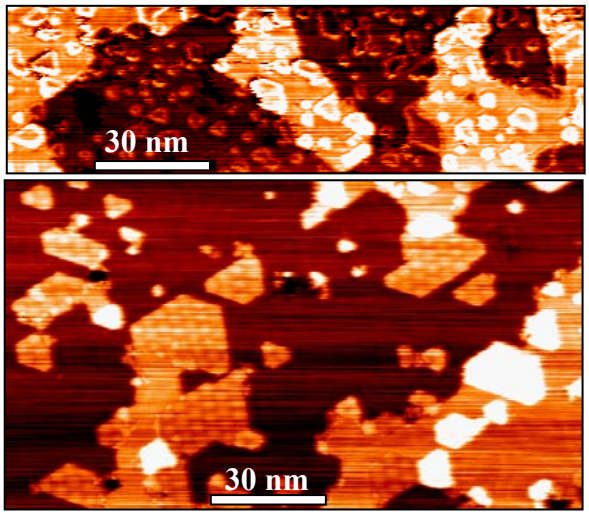

Figure 20: 2D MoS_2 structures on Au(111). The island edges are pronounced for negative tunneling voltage (top) and the islands increase in size during annealing (bottom)

Our MoS_2 crystallites exist in different shapes (triangular, hexagonal, truncated hexagonal) (Figure 20 bottom) and exhibit pronounced edge sites (Figure 20 top) as described by Helveg et al.[68]. These edge sites were attributed to 1D metallic states and it was shown that they exhibit an enhanced catalytic activity. We did not observe an analog pronunciation of the edge sites in case of TiS_2. Possibly, the different environment of the metal atoms (Mo in MoS_2 is in trigonal prismatic coordination, Ti in TiS_2 is in octahedral coordination) might explain the different electronic edge structure which in turn might give rise to different catalytic properties.

6. Enhanced transient reactivity of oxygen-sputtered Au(111) surfaces

(Relevant paper: VII)

The high reactivity of dispersed gold nanoparticles supported on metal oxide surfaces has recently attracted considerable interest. For example, gold nanoparticles on TiO_2(110) are very efficient catalysts for the low temperature oxidation of CO[3], as well as the decomposition of SO_2[69]. Various models have been proposed to explain the unusual catalytic properties of gold nanoclusters ranging from metal-support interactions to finite size effects[3]. In addition to these models, a recent theoretical study by Rodriguez et al.[70] suggests that under-coordinated Au atoms in Au nanoparticles should exhibit an enhanced catalytic reactivity. Specifically, this study revealed that SO_2 interacts more strongly with under-coordinated Au atoms than with regular terrace atoms of Au(111) surfaces.

In contrast to the high reactivity of supported Au nanoparticles, bulk metallic gold typically exhibits a low reactivity. For example, Liu et al. observed that SO_2 adsorbs molecularly on Au(111) at 100 K[71], and desorbs without noticeable decomposition at 150 K.

We investigated the interaction of SO_2 with oxygen-sputtered Au(111) surfaces ($\theta_{oxygen} \leq 0.35$ ML) by monitoring the oxygen and sulfur coverages as a function of SO_2 exposure. Two reaction regimes were observed: oxygen depletion followed by sulfur deposition (Figure 21). The decreasing oxygen coverage with increasing SO_2 exposure suggests that chemisorbed oxygen on Au(111) surfaces can be abstracted by impinging SO_2 molecules via SO_3 formation:

$$SO_2 + O_{ad} \rightarrow SO_{3,\,gas} \qquad \text{(I)}$$

The deposition of sulfur is only observed *after* the initially adsorbed oxygen is *completely* removed by reaction (I). The observation of S deposition can be explained in terms of a disproportionation reaction of SO_2 into adsorbed S and SO_3 via a two-step mechanism:

SO_2 decomposition: $SO_2 \rightarrow S_{ad} + 2O_{ad}$, (II)

followed by O abstraction (I).

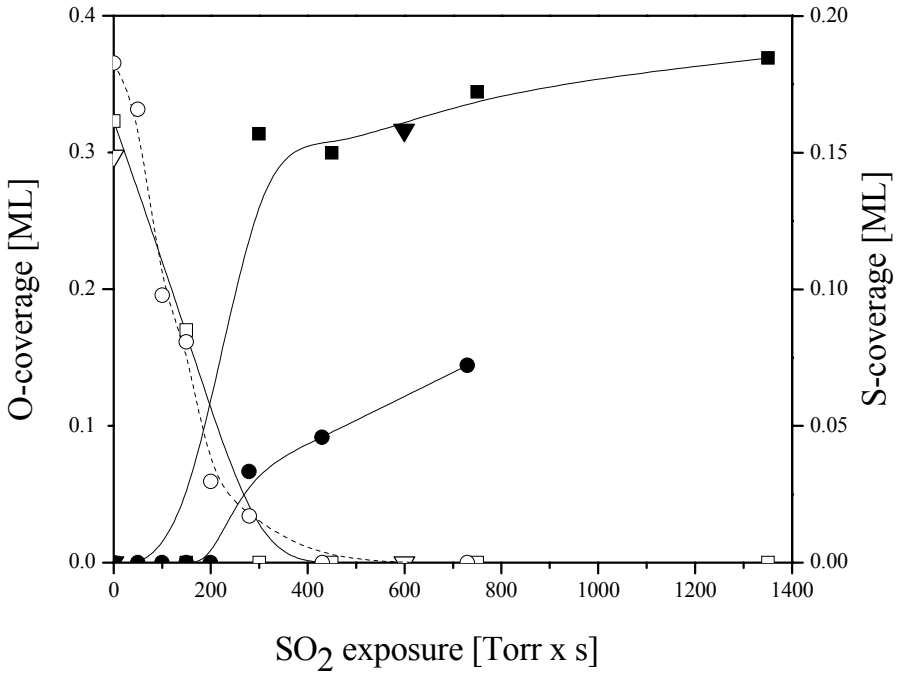

Figure 21: Transient enhanced reactivity towards SO_2 decomposition of O-sputtered Au(111) surfaces (full symbols indicate S coverage, open symbols O coverage). Note that the step-like increase in the sulfur coverage at the oxygen depletion point is more pronounced if SO_2 is dosed continuously (squares, trinagles) rather than in small increments (circles).

The Au(111) surface exhibits an enhanced, transient reactivity towards SO_2 decomposition within the first one hundred langmuir of SO_2 exposure after reaching the oxygen depletion point. The extent of this reactivity enhancement is strongly influenced by the experimental procedure: The step-like increase in the S-coverage at the oxygen depletion point is more pronounced if the Au surface is continuously exposed to SO_2 while reaching the oxygen depletion point (Figure 21, squares and tringles) and not interrupted for collecting AES data (Figure 21, circles). This reveals that the surface reactivity towards SO_2

disproportionation decreases on a timescale of a few minutes (typical time necessary to collect AES data) *after* reaching the oxygen depletion point.

The enhanced reactivity towards S deposition can be explained by the presence of highly reactive, under-coordinated Au atoms. Adsorbed oxygen appears to stabilize, but also to block these sites. In absence of the stabilization effect of adsorbed oxygen, i.e. at the oxygen depletion point, the enhanced reactivity decays on a timescale of a few minutes, suggesting that the undercoordinated Au atoms assume a more stable configuration (higher coordination). This is the first experimental evidence for the theoretical predictions made by Rodriguez et al.[70] and thus sheds new light on the catalytic reactivity of highly dispersed gold nanoparticles.

7. Summary

In conclusion, I have synthesized and characterized several novel two-dimensional nanocrystalline metal oxide and metal sulfide structures on Au(111) surfaces. The main results of this work can be summarized as follows:

By choosing the Mo deposition method (CVD vs. PVD) we are able to control the distribution of the resulting Mo nanostructures. The difference in the Mo cluster distribution reflects the different processes involved in Mo deposition: in case of CVD, the precursor $Mo(CO)_6$ decomposes preferentially at step edges leading to a step edge decoration of Mo clusters, whereas in case of PVD a place exchange of impinging Mo atoms with Au atoms at the elbow sites of the reconstruction leads to terrace decoration. Surface alloying becomes an important process if Mo deposition via PVD is performed at elevated temperatures (525 K and above).

Nanocrystalline 2D MoO_3 islands on Au(111) can be synthesized by Mo deposition followed by oxidation using NO_2. These single layer MoO_3 islands exhibit a different structure than bulk MoO_3: both bond angles and bond lengths of single-layer MoO_3 islands on Au(111) are distorted to fit the geometry and symmetry of the underlying substrate leading to different electronic properties: MoO_3 on Au(111) is semi-metallic whereas bulk MoO_3 is semi-conducting. Furthermore, the spatial distribution, shape and size of single-layer MoO_3 islands can be controlled by the Mo deposition method (CVD versus PVD) and the substrate temperature during Mo deposition and Mo oxidation. Finally, the oxidation state of Mo can be tuned by annealing causing a partial reduction to Mo^{+5}. The possibility to control the morphology as well as the chemical composition potentially opens the door to design novel catalysts.

Two-dimensional nanocrystalline triangular TiS_2 islands on Au(111) were synthesized using a novel approach: PVD of Ti on AuS-covered Au(111) surfaces. In contrast to MoO_3, the TiS_2 islands exhibit the same intrinsic structure as the corresponding bulk material. A lattice mismatch of 20% between TiS_2 and Au gives rise to a Moire superlattice. The energy cost of S not solely occupying high symmetry sites, such as the three-fold hollow sites, is obviously smaller than the energy necessary to distort the structure, consistent with van-der-Waals type interactions between the Au(111) surface and the TiS_2 islands. This is in contrast to MoO_3 islands on Au(111) (chapter 5.1) where the interaction between the Au(111) surface and the MoO_3 islands leads to the distortion of bond angles and bond lengths. Both size and orientation of the TiS_2 nanocrystals can be controlled by the preparation parameters, and a novel metal-rich TiS_{2-x} phase can be synthesized under non-stoichiometric reaction conditions. Using the same approach as for TiS_2, we further synthesized MoS_2 islands on Au(111). In contrast to TiS_2 islands which exhibit bulk terminated edges, MoS_2 island edges are reconstructed.

Sulfur-induced corrosion of the Au(111) surface and the development of a 2D AuS phase was investigated by real-time imaging. Even small amounts of S (<0.1 ML) modify the surface structure: the surface stress is reversed from tensile to compressive which causes expansion of the surface layer and lifting of the reconstruction pattern. Higher S coverages lead to a massive mass transport and a dynamic large-scale surface restructuring: Au atoms are removed from the surface layer, and incorporated into a growing AuS phase. This AuS phase develops a long-range ordered, incommensurate structure upon annealing.

These examples demonstrate that the Au surface is not an inert, static substrate material. In fact, the Au(111) surface can be directly involved in surface reactions (formation of AuS) as well as affect/modify the intrinsic structure (MoO_3) or morphology/orientation (TiS_2) of adsorbates via stress-field interactions. Furthermore the Au(111) surface exhibits reactive sites for metal surface alloying (elbows) and precursor decomposition (step edges). Finally, we demonstrated that undercoordinated Au atoms exhibit an enhanced reactivity towards SO_2 decomposition.

8. References

[1] J. W. G. Wildoer, L. C. Venema, A. G. Rinzler, et al., Nature **391**, 59 (1998).

[2] T. W. Odom, J. Huang, P. Kim, et al., Nature **391**, 62 (1998).

[3] M. Valden, X. Lai, and D. W. Goodman, Science **281**, 1647 (1998).

[4] Z. P. Chang, Z. Song, G. Liu, et al., Surf. Sci. **512**, L353 (2002).

[5] L. M. Liz-Marzan, materialstoday, p. 26, february 2004.

[6] Y. M. Wang and E. Ma, Appl. Phys. Lett. **80**, 2395 (2002).

[7] R. Valiev, Nature **419**, 887 (2002).

[8] J. A. Rodriguez, J. Dvorak, T. Jirsak, et al., Surf. Sci. **490**, 315 (2001).

[9] A. J. Jaworowski, M. Smedh, M. Borg, et al., Surf. Sci. **492**, 185 (2001).

[10] G. H. Smudde and P. C. Stair, Surf. Sci. **317**, 65 (1994).

[11] G. E. Poirier and E. D. Pylant, Science **272**, 1145 (1996).

[12] A. Ulman, Chem. Rev. **96**, 1533 (1996).

[13] G. E. Poirier, Chem. Rev. **97**, 1117 (1997).

[14] B. Hammer and J. K. Norskov, Nature **376**, 238 (1995).

[15] J. Wang and E. Koehl, J. Phys. Chem. A **102**, 8573 (1998).

[16] M. Haruta, Catal. Today **36**, 153 (1997).

[17] P. G. Clark, PhD thesis, *UHV-STM Studies of Cobalt Thin Films Deposited on Clean, Oxygen- and Sulfur-covered Molybdenum (110)*, Harvard University, Department of Chemistry (1999)

[18] W. W. Crew and R. J. Madix, Rev. Sci. Instrum. **66**, 4552 (1995).

[19] M. V. R. Murty, T. Curcic, A. Judy, et al., Phys. Rev. B **60**, 16956 (1999).

[20] H. Ibach, Surf. Sci. Rep. **29**, 193 (1997).

[21] C. Woell, R. J. Chiang, J. Wilson, et al., Phys. Rev. B **39**, 7988 (1989).

[22] J. V. Barth, H. Brune, G. Ertl, et al., Phys. Rev. B **42**, 9307 (1990).

[23] V. Repain, J. M. Berroir, S. Rousset, et al., Appl. Surf. Sci. **162**, 30 (2000).

[24] D. M. Kolb, Prog. Surf. Sci. **51**, 109 (1996).

[25] C. Vericat, J. N. Andersen, M. E. Vela, et al., J. Phys. Chem. B **104**, 302 (2000).
[26] J. A. Stroscio, D. T. Pierce, R. A. Dragoset, et al., J. Vac. Sci. Technol. A **10**, 1981 (1992).
[27] B. Voigtlaender, G. Meyer, and N. Amer, Phys. Rev. B **44**, 10354 (1991).
[28] D. Chambliss, R. Wilson, and S. Chiang, Phys. Rev. Let. **66**, 1721 (1991).
[29] J. A. Meyer, I. D. Baikie, E. Kopatzki, et al., Surf. Sci. **365**, L647 (1996).
[30] P. J. Spencer, United States Patent **4,607,127** (1986).
[31] N. D. Spencer and C. J. Pereira, Am. Inst. Chem. Eng. J. **33**, 1808 (1987).
[32] N. D. Spencer, J. Catal. **109**, 187 (1988).
[33] M. A. Banares, N. D. Spencer, M. D. Jones, et al., J. Catal. **146**, 204 (1994).
[34] M. Chen, C. M. Friend, and E. Kaxiras, J. Am. Chem. Soc. **123**, 2224 (2001).
[35] J. Haber and E. Lalik, Catal. Today **33**, 119 (1997).
[36] X. Deng, M. M. Biener, J. Biener, et al., (to be published).
[37] E. Itoh, K. Hayakawa, and S. Oishi, J. Phys.: Condens. Matter **13**, 6853 (2001).
[38] Z. Song, T. Cai, Z. Chang, et al., J. Am. Chem. Soc. **125**, 8059 (2003).
[39] G. S. Rohrer, V. E. Henrich, and D. A. Bonnell, Science **250**, 1239 (1990).
[40] G. N. Phillips and K. A. Evans, Nature **429**, 860 (2004).
[41] G. E. Poirier, Langmuir **13**, 2026 (1997).
[42] K. S. Yoo, I. W. Sorensen, and W. S. Glaunsinger, J. Vac. Sci. Technol. A **12**, 192 (1994).
[43] U.S. Patent No. 4724008, (Arizona Instrument Corporation, 1988)
[44] R. L. McCarley, Y. T. Kim, and J. Bard, J. Phys. Chem. **97**, 211 (1992).
[45] H. Martin, C. Vericat, G. Andreasen, et al., Langmuir **17**, 2334 (2001).
[46] C. Vericat, M. E. Vela, G. Andreasen, et al., Langmuir **17**, 4919 (2001).
[47] C. Vericat, M. E. Vela, G. A. Andreasen, et al., Phys. Rev. Lett. **90**, 075506 (2003).
[48] X. Gao, Y. Zhang, and M. J. Weaver, J. Phys. Chem. **96**, 4156 (1992).
[49] M. Kostelitz and J. Oudar, Surf. Sci **27**, 176 (1971).
[50] M. Kostelitz, J. L. Domange, and J. Oudar, Surf. Sci. **34**, 431 (1972).
[51] J. A. Rodriguez, J. Dvorak, T. Jirsak, et al., J. Am. Chem. Soc. **125**, 276 (2002).
[52] I. Touzov and C. B. Gorman, Langmuir **13**, 4850 (1997).
[53] V. Podzorov and M. E. Gershenson, Appl. Phys. Lett. **84**, 3301 (2004).
[54] M. S. Whittingham, Solid State Ionics **134**, 169 (2000).
[55] M. S. Whittingham, Science **192**, 1126 (1972).
[56] L. Margulis, G. Salitra, R. Tenne, et al., Nature **365**, 113 (1993).

[57] R. Tenne, L. Margulis, M. Genut, et al., Nature **360**, 444 (1992).
[58] R. Tenne, M. Homyonfer, and Y. Feldman, Chem. Mater. **10**, 3225 (1998).
[59] G. L. Frey, S. Elani, M. Homyonfer, et al., Phys. Rev. B **57**, 6666 (1998).
[60] G. Seifert, H. Terrones, M. Terrones, et al., Solid State Commun. **114**, 245 (2000).
[61] C. Wang, L. Dotson, M. McKelvy, et al., J. Phys. Chem. **99**, 8216 (1995).
[62] C. M. Fang, R. A. de Groot, and C. Haas, Phys. Rev. B **56**, 4455 (1996).
[63] J. Cheon, J. E. Gozum, and G. S. Girolami, Chem. Mater. **9**, 1847 (1997).
[64] S. Kikkawa and M. Miyazaki, J. Mater. Res. **5**, 2894 (1990).
[65] S. Kikkawa, R. Shimanouchi-Futagami, and M. Koizumi, Appl. Phys. A **49**, 105 (1989).
[66] H. S. W. Chang and D. M. Schleich, J. Solid State Chem. **100**, 62 (1992).
[67] T. S. Lewkebandara and C. H. Winter, Adv. Mater. **6**, 237 (1994).
[68] S. Helveg, J. V. Lauritsen, E. Laegsgaard, et al., Phys. Rev. Lett. **84**, 951 (2000).
[69] J. A. Rodriguez, G. Liu, T. Jirsak, et al., J. Am. Chem. Soc. **124**, 5242 (2002).
[70] J. A. Rodriguez, M. Perez, T. Jirsak , et al., Chem. Phys. Lett. **378**, 526 (2003).
[71] G. Liu, J. A. Rodriguez, J. Dvorak, et al., Surf. Sci. **505**, 295 (2002).

9. Acknowledgements

I feel like sitting on a mountain top with an endless horizon around me. The way up here was steep and windy, and most of all exciting. God only knows where I would be without the help of many - who helped me find the way and made this journey a real pleasure.

Specifically, I would like to gratefully acknowledge the enthusiastic supervision of Prof. Cynthia M. Friend, at Harvard University, without whom this thesis would not exist. She gave me the opportunity and encouraged me to do real science again, which I missed so much. I would like to thank Prof. Marcus Baeumer, at Bremen University, for many very helpful discussions and suggestions and in particular for his support of this external dissertation and for bearing the administrative burden connected with that. I would further like to thank the Friend Group for the very friendly atmosphere and for everybody's individual way of contributing, specifically Dilini Pinnaduwage, Su Ying Quek, Xingyi Deng, Dae-Hyuk Kang and Wanda DiBernardo who keeps me connected with the Friend group even during my time in California. I would like to thank Richard Schalek for his support and friendship, especially in the difficult experimental endphase.

Finally, I would like to give my special thanks to Juergen Biener, my beloved husband, for all his support – emotional and scientific - and his endless encouragement.

I

Available online at www.sciencedirect.com
SCIENCE DIRECT®
Surface Science 559 (2004) L173–L179
SURFACE SCIENCE
www.elsevier.com/locate/susc

Surface Science Letters

Heteroepitaxial growth of novel MoO_3 nanostructures on Au(1 1 1)

Monika M. Biener [a,b], Cynthia M. Friend [a,b,*]

[a] Department of Chemistry, Harvard University, 12 Oxford Street, Cambridge, MA 02138, USA
[b] Division of Engineering and Applied Sciences, Harvard University, 12 Oxford Street, Cambridge, MA 02138, USA

Received 10 February 2004; accepted for publication 16 April 2004
Available online 10 May 2004

Abstract

We have developed a synthetic procedure that yields novel nanocrystalline, islands of MoO_3 on Au(1 1 1). Careful control of the growth conditions yields monolayer islands with a rectangular unit cell that is aligned with the Au substrate. These structures are distinctly different than either bulk MoO_3 or than ramified, two-dimensional MoO_3 islands formed on Au(1 1 1) which were recently reported [J. Am. Chem. Soc. 125 (2003) 8059, Surf. Sci. 512 (2002) L353]. The atomic structure of these single-layer MoO_3 islands has been characterized by scanning tunnelling microscopy (STM), low energy electron diffraction (LEED), X-ray photoelectron spectroscopy (XPS), and Auger electron spectroscopy (AES). We discuss our synthetic method and important characteristics of the MoO_3 islands.

Keywords: Low energy electron diffraction (LEED); Scanning tunneling microscopy; Catalysis; Epitaxy; Growth; Surface chemical reaction; Gold; Molybdenum oxides

1. Introduction

Metal oxides are of considerable interest because of their electronic properties and their role in several important technologies. One significant application of metal oxides is in the area of heterogeneous catalysis, in particular conversion of hydrocarbons to oxygenates that is of interest as alternative fuels and as building blocks for other chemicals. Molybdenum trioxide is specifically known to promote the partial oxidation of methane to formaldehyde [3–6].

Metal oxides have a wide range of chemical, electronic and optical properties that depend on stoichiometry and size scale. For example, bulk MoO_3 is a semiconductor with a bandgap of 2.8 eV; however, states are introduced in the gap when point defects due to loss of oxygen are introduced [7]. Catalytic activity is often attributed to the presence of oxygen vacancies associated with edge sites of the material [8].

Chemical, electronic, and optical properties of materials can be influenced by changing the length scale from macroscopic to nanoscale particles or

* Corresponding author. Address: Department of Chemistry, Harvard University, 12 Oxford Street, Cambridge, MA 02138, USA. Tel.: +1-617-495-4052; fax: +1-617-496-8410.
E-mail address: cfriend@deas.harvard.edu (C.M. Friend).

0039-6028/$ - see front matter
doi:10.1016/j.susc.2004.04.021

films. For example gold nanoparticles dispersed on metal oxides are chemically active [2,9], whereas bulk gold is inert. Molybdenum clusters on gold exhibit a very low activity towards O_2 and CO [2,10], whereas bulk Mo dissociates CO and O_2 below 300 K [11,12], providing another example. Hence, it is important to develop methods for synthesizing nanoscopic materials.

In this work, we describe a procedure that yields novel nanocrystalline, monolayer islands of MoO_3 on Au(1 1 1). The possibility of creating well-defined, single layer MoO_3 nanocrystals is a first step towards the development of materials with unusual chemical and physical properties.

2. Experimental

All experiments were performed in an ultrahigh vacuum (UHV) system with a base pressure of 4×10^{-10} Torr. The system is equipped with a "beetle-type" STM and commercial instrumentation for AES and LEED, described elsewhere [13,14]. The sample was radiatively heated via a tungsten filament located behind the sample. The temperature was monitored by a chromel/alumel thermocouple affixed to the sample holder. To account for the temperature gradient of the sample holder versus the crystal a calibration was performed using a thermocouple directly mounted to the crystal.

The Au was cleaned by cycles of Ar^+ sputtering (1000 eV, ~5 μA) at 300 K, followed by annealing to 700 K for 10 min and 600 K for 60 min. This procedure was repeated several times until no contaminants were detected using AES. Following this procedure, a LEED pattern characteristic of the Au(1 1 1)-$(22\times\sqrt{3})$ reconstruction [15] was observed. The "herringbone" reconstruction was also observed by STM.

$Mo(CO)_6$ (Alfa Aesar) was initially purified by freeze–pump–thaw cycles, and NO_2 (Matheson, anhydrous grade) was used as received. Both reagents were introduced to the sample by backfilling the chamber to 1×10^{-7} Torr. Gas lines were evacuated before each dose. All exposures are given in uncorrected ion gauge readings using units of Langmuir ($1\ L = 10^{-6}$ Torr s).

Molybdenum nanoclusters were deposited on Au(1 1 1) surfaces at 450 K via chemical vapor deposition (CVD) of $Mo(CO)_6$. Nanocrystalline MoO_3 was prepared by subsequent exposure to NO_2 at 450 K, followed by annealing at 600 K.

All STM images were collected at room temperature using commercial $Pt_{0.8}Ir_{0.2}$ tips (molecular imaging). Scan dimensions were calibrated by imaging the unit cell of the Au(1 1 1) surface. The sample bias voltage was set between +0.1 and +2.8 V. All images are unfiltered and only background corrected.

3. Results and discussion

Preferential nucleation of three-dimensional molybdenum nanoclusters at step edges was observed after dosing 4 L of $Mo(CO)_6$ onto the Au(1 1 1)-$(22\times\sqrt{3})$ surface maintained at 450 K (Fig. 1). The apparent height of the Mo clusters is in the range of 0.3–0.7 nm and their average diameter is ~10 nm. No carbon or oxygen was detected by AES. The herringbone reconstruction persists on the terraces of the Au surface following deposition of the Mo clusters (data not shown).

The preferred nucleation of Mo clusters along the step edges is in contrast to the deposition of

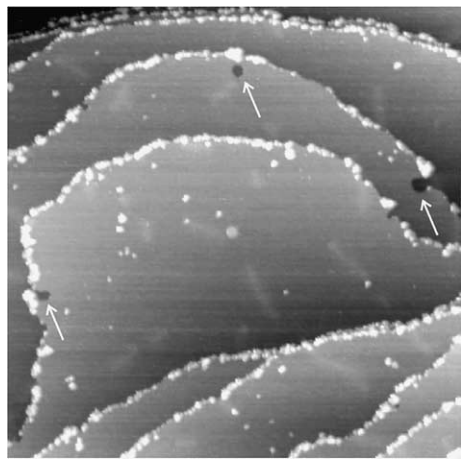

Fig. 1. STM image showing Mo particles formed by exposure of the Au(1 1 1)-$(22\times\sqrt{3})$ surface to 4 L of $Mo(CO)_6$ at 450 K. Etch holes are indicated by arrows. The image was obtained at 300 K and corresponds to an area of 400 nm×400 nm.

Mo via physical vapor deposition (PVD), where the clusters preferentially nucleate at the elbow sites of the herringbone reconstruction as reported recently [16] and reproduced in our laboratory [17]. Our results are also different than those reported previously for growth of Mo clusters deposited using thermal decomposition of $Mo(CO)_6$, but using a different experimental configuration [18]. This difference is attributed to the strong sensitivity of the CVD process to temperature and to CO induced mobility of Mo nanoclusters [19].

The strong sensitivity of the CVD process to surface temperature is illustrated by the fact that the deposition rate decreases to an immeasurable rate at a surface temperature of 400 K. Specifically, no Mo was detected by means of STM after exposure of up to 100 L at 10^{-7} Torr of $Mo(CO)_6$ to the surface maintained at 400 K. Furthermore, no extraneous material or other changes were observed. This decrease in deposition rate is consistent with the fact that the CVD process is thermally activated. At minimum, dissociation of one Mo–CO bond is required to deposit Mo from $Mo(CO)_6$, which has an energy cost of ~40 kcal/mol [20]. Surprisingly, the amount of Mo observed using STM after exposure of 4 L of $Mo(CO)_6$ to the Au surface maintained at 500 K was less than 20% of that observed at 450 K using the same flux and integrated dose. This observation is consistent with precursor-mediated decomposition: at higher temperatures the surface lifetime of the $Mo(CO)_6$ precursor decreases due to an increased desorption rate. The lifetime, τ, of the precursor would decrease by a factor of 5 upon increasing the surface temperature from 450 to 500 K. This estimate assumes a $Mo(CO)_6$ desorption barrier of 14 kcal/mol [18] and that the pre-exponential factor for desorption, A, is the same at the two temperatures. The ratio of lifetimes at the two temperatures is calculated using the Frenkel equation: $\tau = 1/A* \exp(E_{des}/RT_s)$, where E_{des} is the activation barrier and T_s is the surface temperature. The pre-exponential factors cancel in the ratio. This is in agreement with our observation that the Mo coverage decreased to ~20%.

The Au surface itself promotes the decomposition of $Mo(CO)_6$ based on the fact that small sulfur coverages (<0.1 ML) completely inhibit the decomposition of $Mo(CO)_6$ on the Au(1 1 1) surface, most likely by poisoning active sites. Specifically, no Mo was detected after exposure to 4 L $Mo(CO)_6$ at 450 K by means of AES and STM. If the Au surface were simply a source of thermal energy, there would not be such a strong dependence of the Mo deposition rate on the presence of a small amount of impurity. It is known that the most stable bonding sites for sulfur are located at the step edges of Au(1 1 1) [21]. This indicates that the active sites for $Mo(CO)_6$ decomposition are related to step edges of the Au surface. We were, however, not able to identify the active sites by STM.

The Mo nanoclusters probably also contain Au based on changes in the surface morphology observed in STM following CVD of the Mo. Specifically, the originally straight step edges become irregular. Etch holes appear along the step edges between neighbouring molybdenum clusters (Fig. 1). These observations are also consistent with the appearance of nanoscopic holes as observed in our previous work [19] when Mo is transported from terraces to step edges by CO exposure.

Oxidation of the Mo nanoclusters using exposure to NO_2 at 450 K leads to spreading into a two-dimensional layer and full oxidation to MoO_3, in qualitative agreement with previous studies [1,2]. The predominant oxidation state was determined to be Mo^{6+} using X-ray photoelectron spectroscopy (data not shown), as described in detail elsewhere [22].

Nanocrystalline MoO_3 islands that are one layer high and ordered relative to the underlying gold surface are formed using our iterative dosing procedure described below (Figs. 2 and 3). The structure of the observed single-layer MoO_3 differs from the bilayer structure of bulk MoO_3 [23] and can be explained in terms of an ordered, two-dimensional array of interacting MoO_3 entities based on a combination of experimental data and associated density functional theory calculations, described elsewhere [24]. The apparent height of the islands is ~0.5 nm, in contrast to 1.38 nm as the height of a bulk bilayer unit cell, which is consistent with the single layer structure described above.

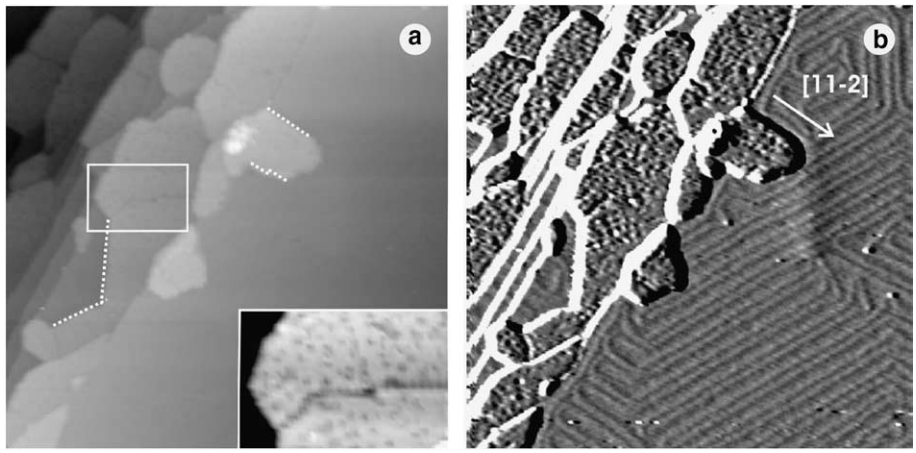

Fig. 2. STM image showing nanocrystalline MoO_3 islands on Au(1 1 1) after alternate exposure to 1 L $Mo(CO)_6$ and 10 L NO_2 at 450 K followed by annealing to 600 K for 1 min after every four cycles of dosing for a total of 16 cycles: (a) alignment of the island edges (dotted lines) with the $\langle 1\,1\,-2\rangle$ directions of the substrate: a magnification of a domain wall is shown in the inset (28 nm × 18 nm); (b) image is differentiated to enhance the contrast and show the orientation of the substrate. The $\langle 1\,1\,-2\rangle$ directions run parallel to the herringbone dislocation lines; one of them is indicated in the figure. The total coverage, as estimated by AES, is ~0.3 ML, however, the local coverage is strongly dependent on the substrate step density. The image was obtained at 300 K and corresponds to an area of 120 nm × 120 nm.

The MoO_3 islands nucleate preferentially along step-edges, and exhibit well-defined edges with kinks and domain walls (Fig. 2). The islands are aligned with the Au(1 1 1) surface, based on the observation of a well-ordered LEED pattern (see Fig. 3c and discussion below). STM reveals that the island edges run parallel to the $\langle 1\,1\,-2\rangle$ directions of the substrate, if the shape of the islands is not dictated by the step edges of the substrate. STM data further reveal a rectangular unit cell with dimensions of 0.50×0.57 nm$^2 \pm 10\%$, consistent with the observation of a well-defined c(2 × 4) LEED pattern (Fig. 3). Note that the observation of the c(4 × 2) LEED pattern, as shown in (Fig. 3c), implies the existence of rotational domains. Occasionally, domain walls (Fig. 2a, inset) were observed by STM. The growth of the MoO_3 islands away from the step edge is a direct consequence of the fact that the Mo clusters have nucleated at the step edge prior to oxidation. Nanocrystalline MoO_3 islands with the same unit cell form on terraces when Mo clusters, deposited using physical vapor deposition, are oxidized [17]. The alignment of those islands with the Au substrate is more pronounced, compared to the islands shown in (Fig. 2), as the island shape is not dictated by the Au step edges.

The crystallinity of the MoO_3 islands depends on the conditions used for oxidation due to kinetic control of the oxidation and growth. Small Mo clusters (diameter $\leqslant 5$ nm) are required as starting material in order to form crystalline structures. Disordered molybdenum oxide particles, which are only partially oxidized to Mo + 6 and not completely spread into small 2D islands, form upon oxidation of larger Mo clusters (Fig. 4). In order to grow large MoO_3 islands, repeated cycles of Mo deposition in small amounts and subsequent oxidation are used (Fig. 2). For example, the MoO_3 islands shown in Fig. 2 are formed by alternate exposure of the surface to 1 L of $Mo(CO)_6$ and 10 L NO_2 at 450 K followed by annealing to 600 K for 1 min after every four cycles of dosing for a total of 16 cycles. This procedure yields well-ordered islands with an average size of 600 nm^2—large enough to observe a clear LEED pattern.

In order to study the growth mechanism of the MoO_3 islands, $Mo(CO)_6$ was dosed at 450 K to a MoO_3-covered Au(1 1 1) surface. STM images

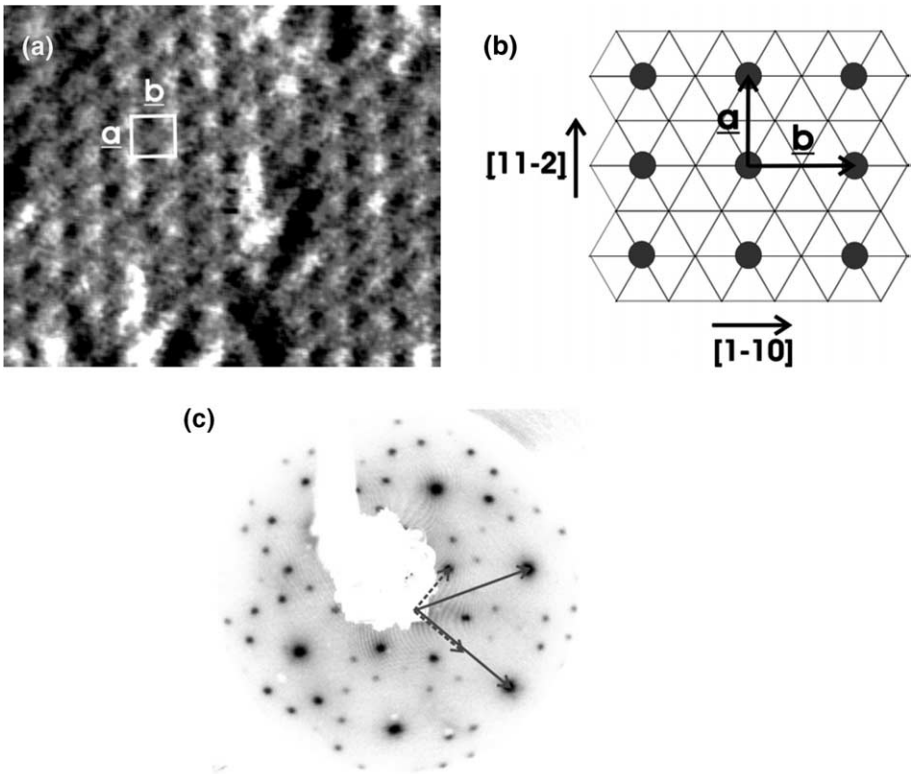

Fig. 3. Identification of the c(4×2) unit cell of the MoO_3 islands on Au(1 1 1) prepared by alternate exposure of the surface to 1 L $Mo(CO)_6$ and 10 L NO_2 at 450 K followed by annealing to 600 K for 1 min after every four cycles of dosing for a total of 16 cycles: (a) high resolution STM image (50 nm×60 nm) showing a rectangular unit cell with $a = 0.50$ nm and $b = 0.57$ nm ±10%, obtained at 300 K; (b) schematic of a c(4×2) superlattice on a hexagonal substrate, corresponding to unit cell dimensions of $a = 0.499$ nm, $b = 0.576$ nm for a Au(1 1 1) surface with the closest-packed rows of the superlattice running in the [1 1 −2] direction; (c) LEED pattern obtained at 300 K showing a c(4×2) structure (part of the picture is blocked out by the sample holder). Straight arrows indicate the basis of the hexagonal unit cell of the Au substrate, dotted arrows indicate the basis of one rotational domain (basis of the other two domains not shown) of the c(4×2) superlattice.

obtained at 300 K reveal that Mo clusters nucleate exclusively at Au step edges (Fig. 5). Mo deposition at edges of the MoO_3 islands was *not* observed. This implies that the oxidation of molybdenum clusters leads to mass transport from the step edges to the islands. Mobile MoO_3 species are created at the step edges and diffuse along the surface until they hit the edge of a MoO_3 island. Volatile $(MoO_3)_n$ ($n = 3, 4, 5$) species have been previously detected by mass spectrometric studies during sublimation of MoO_3 bulk oxide [25]. The compact shape of the islands indicates that the aggregation of these mobile clusters is reversible [26]. Detachment from the island or diffusion along the edge of the islands is possible at the chosen temperature (450 K) and influences island shape and size. Larger crystalline islands grow at the expense of smaller islands. Small islands have a larger perimeter to area ratio than large islands and are thus thermodynamically less favorable (Ostwald ripening). In contrast, a fractal island shape can be expected if the substrate temperature is too low to activate detachment of atoms or clusters from the islands and thus aggregation is irreversible [26].

Gold as a noble metal is ideally suited as inert support for the oxidation of metals since neither O_2 nor NO_2 decompose under UHV conditions on

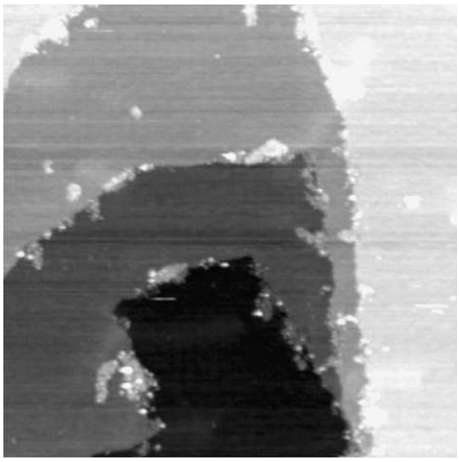

Fig. 4. STM image showing partially oxidized Mo oxide islands formed by exposure of 4 L of $Mo(CO)_6$ and 40 L of NO_2 at 450 K. The image was obtained at 300 K and corresponds to an area of 200 nm × 200 nm.

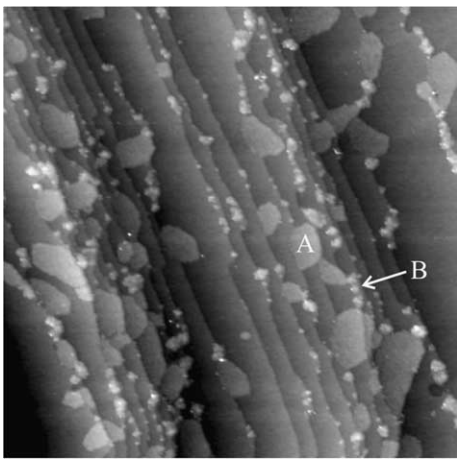

Fig. 5. STM image showing a MoO_3-covered Au(1 1 1) surface after exposure to 1 L of $Mo(CO)_6$ at 450 K. The figure illustrates that Mo clusters (B) nucleate exclusively at Au step edges and not at the edges of the MoO_3 islands (A). The image was obtained at 300 K and corresponds to an area of 300 nm × 300 nm.

Au(1 1 1) [27,28]. Selective oxidation of metal clusters deposited on Au(1 1 1) is, thus, possible by exposure to an oxidant. Recently the inertness of Au(1 1 1) was utilized to grow V_2O_3 films by evaporation of vanadium in an oxygen atmosphere [29]. The weak interaction of Au with oxygen also facilitates the diffusion of the MoO_3 species. However, the interaction is strong enough to influence the structure and orientation of the MoO_3 islands. As Mo has a higher surface free energy (2.88 $J\,m^{-2}$) than gold (1.62 $J\,m^{-2}$) [30] the formation of 3D molybdenum nanoclusters can be expected. The spreading of the 3D metal clusters during oxidation is consistent with the low free surface energy of MoO_3 ($5–7\times10^{-2}$ $J\,m^{-2}$) [31].

4. Conclusion

We are able to grow two-dimensional compact MoO_3 islands on Au(1 1 1) by carefully controlling the growth kinetics. A $c(4\times2)$ unit cell was determined by STM and LEED. The location of the deposited metal clusters dictates the initial nucleation sites for the metal oxide islands. Repeated cycles of Mo cluster deposition and oxidation in small increments are necessary to create mobile MoO_3 species that are responsible for the mass transport and thus for the island growth. The possibility to create well-defined nanocrystalline MoO_3 islands will enable the study of interesting reactions that are relevant in the field of catalysis and novel sensors. Furthermore, we expect that this methodology can be generalized to the growth of other nanoscopic metal oxides.

Acknowledgements

We gratefully acknowledge support of this work by the National Science Foundation under support for the Harvard Nanoscale Science and Engineering Center, grant no. PHY-011-7795, and the Department of Energy, Basic Energy Sciences, FG02-84-ER13289.

References

[1] Z. Song, T. Cai, Z. Chang, G. Liu, J.A. Rodriguez, J. Hrbek, J. Am. Chem. Soc. 125 (2003) 8059.
[2] Z.P. Chang, Z. Song, G. Liu, J.A. Rodriguez, J. Hrbek, Surf. Sci. 512 (2002) L353.
[3] P.J. Spencer, United States Patent 4,607,127 (1986).
[4] N.D. Spencer, C.J. Pereira, AIChE J. 33 (1987) 1808.

[5] N.D. Spencer, J. Catal. 109 (1988) 187.
[6] M.A. Banares, N.D. Spencer, M.D. Jones, I.E. Wachs, J. Catal. 146 (1994) 204.
[7] M. Chen, C.M. Friend, E. Kaxiras, JACS (2001).
[8] J. Haber, E. Lalik, Catal. Today 33 (1997) 119.
[9] M. Valden, X. Lai, D.W. Goodman, Science 281 (1998) 1647.
[10] J.A. Rodriguez, J. Dvorak, T. Jirsak, J. Hrbek, Surf. Sci. 490 (2001) 315.
[11] A.J. Jaworowski, M. Smedh, M. Borg, A. Sandell, A. Beutler, S.L. Sorensen, E. Lundgreen, J.N. Andersen, Surf. Sci. 492 (2001) 185.
[12] G.H. Smudde, P.C. Stair, Surf. Sci. 317 (1994) 65.
[13] P.G. Clark, C.M. Friend, J. Chem. Phys. 111 (1999) 6991.
[14] M. Chen, P.G. Clark, T. Mueller, C.M. Friend, E. Kaxiras, Phys. Rev. B 60 (1999) 11783.
[15] M.V.R. Murty, T. Curcic, A. Judy, B.H. Cooper, Phys. Rev. B 60 (1999) 16956.
[16] S. Helveg, J.V. Lauritsen, E. Laegsgaard, I. Stensgaard, J.K. Norskov, B.S. Clausen, H. Topsoe, F. Besenbacher, Phys. Rev. Lett. 84 (2000) 951.
[17] M.M. Biener, J. Biener, R. Schalek, C.M. Friend, in press.
[18] Z. Song, T.H. Cai, J.A. Rodriguez, J. Hrbek, A.S.Y. Chan, C.M. Friend, J. Phys. Chem. B 107 (2003) 1036.
[19] A. Chan, B. Richter, C. Friend, M. Aziz, J. Hrbek, Z. Song, Nano Letters (2003).
[20] K.E. Lewis, D.M. Golden, G.P. Smith, J. Am. Chem. Soc. 106 (1984) 3912.
[21] C. Vericat, J.N. Andersen, M.E. Vela, R.C. Salvarezza, J. Phys. Chem. B 104 (2000) 302.
[22] M.M. Biener, J. Biener, X. Deng, C.M. Friend, in press.
[23] E. Itoh, K. Hayakawa, S. Oishi, J. Phys.: Condens. Matter 13 (2001) 6853.
[24] S.Y. Quek, M.M. Biener, J. Biener, C.M. Friend, E. Kaxiras, in press.
[25] G. Demaria, R.P. Burns, J. Drowart, M.G. Inghram, J. Chem. Phys. 32 (1960) 1373.
[26] A.-L. Barabasi, H.E. Stanley, Fractal Concepts in Surface Growth, Cambridge University Press, Cambridge, 1995.
[27] J. Wang, E. Koehl, J. Phys. Chem. A 102 (1998) 8573.
[28] N.D.S. Canning, D. Outka, R.J. Madix, Surf. Sci. 141 (1984) 240.
[29] A.C. Dupuis, M. Abu Haija, B. Richter, H. Kuhlenbeck, H.J. Freund, Surf. Sci. 539 (2003) 99.
[30] L.Z. Mezey, J. Giber, Jpn. J. Appl. Phys. 21 (1982) 1569.
[31] C.B. Wang, C.T.H.E. Wachs, Langmuir 15 (1999) 1223.

II

submitted to: Journal of Chemical Physics, May 10, 2004
Revised, September 30, 2004

Growth of nanocrystalline MoO_3 on Au(111) studied by in-situ STM

Monika M. Biener[1,2], Juergen Biener[1,3,4], Richard Schalek[3], and Cynthia M. Friend[1,2,†]
[1]Department of Chemistry and
[2]Division of Engineering and Applied Sciences and
[3]Center for Imaging and Mesoscale Structures
Harvard University
12 Oxford Street, Cambridge, Massachusetts 02138 USA
[4]present address: Nanoscale Synthesis and Characterization Laboratory
Lawrence Livermore National Laboratory
7000 East Ave, Livermore, California 94550 USA

[†]Author to whom correspondence should be sent

Abstract

The growth of nanocrystalline MoO_3 islands on Au(111) using physical vapor deposition of Mo has been studied by scanning tunnelling microscopy (STM) and low energy electron diffraction (LEED). The growth conditions affect the shape and distribution of the MoO_3 nanostructures, providing a means of preparing materials with different percentages of edge sites that may have different chemical and physical properties than atoms in the interior of the nanostructures. MoO_3 islands were prepared by physical vapor deposition of Mo and subsequent oxidation by NO_2 exposure at temperatures between 450 K and 600 K. They exhibit a crystalline structure with a c(4x2) periodicity relative to unreconstructed Au(111). While the atomic-scale structure is identical to that of MoO_3 islands prepared by chemical vapor deposition, we demonstrate that the distribution of MoO_3 islands on the Au(111) surface reflects the distribution of Mo clusters prior to oxidation although the growth of MoO_3 involves long-range mass transport via volatile MoO_3 precursor species. The island morphology is kinetically controlled at 450 K, whereas an equilibrium shape is approached at higher preparation temperatures or after prolonged annealing at the elevated temperature. Mo deposition at or above 525 K leads to the formation of a Mo-Au surface alloy as indicated by the observation of embedded MoO_3 islands after oxidation by NO_2. Au vacancy islands, formed when Mo and Au dealloy to produce vacancies, are observed for these growth conditions

Introduction

Nanoparticles and systems in the nanometer size regime have been studied intensively in recent years. These systems may have electronic, optical and catalytic properties which differ considerably from those of the corresponding bulk material and depend strongly on the size and morphology of the structures. For example gold nanoparticles dispersed on metal oxides are chemically active,[1, 2] whereas gold is inert as bulk material. Another example is molybdenum: Mo clusters on gold exhibit a very low activity towards O_2 and CO,[2, 3] whereas bulk Mo dissociates CO and O_2 below 300 K.[4, 5] Hence, an understanding of the growth mechanism and the capability to control the morphology of nanoscopic systems is an important step towards the development of materials with unusual chemical and physical properties.

Considerable interest has been focused on metal oxides because of their broad range of physical and chemical properties and their applications in technology, catalysis and environmental protection. In particular, molybdenum trioxide is known to promote the partial oxidation of methane to formaldehyde.[6-9] Stoichiometric MoO_3 has a bandgap of 2.8 eV, however, states are introduced in the gap when point defects due to loss of oxygen are created.[10] Catalytic activity is often attributed to the presence of oxygen vacancies associated with edge sites of the material.[11]

Recently, the growth of 2D vanadium and iron oxides on metal surfaces has been reported. On Pd(111), a metastable two-dimensional V_2O_3 phase is formed in the submonolayer coverage regime.[12] The morphology of this oxide phase strongly depends on the preparation conditions and is different from the bulk V_2O_3 structure. Similarly, metastable FeO(111) films can be grown on Ru(0001).[13] These studies clearly demonstrate that non-equilibrium metal oxide phases can be stabilized on metal surfaces.

The formation of nanocrystalline MoO_3 islands using chemical vapor deposition (CVD) of Mo has recently been investigated by our group.[14] Briefly, preferential nucleation of Mo clusters at Au step edges was achieved by CVD of Mo using $Mo(CO)_6$ as a precursor. Subsequent exposure of these Mo clusters to NO_2 at 450 K leads to the growth of

nanocrystalline MoO_3 islands, which nucleate preferentially at the step edges. Both scanning tunnelling microscopy (STM) and low energy electron diffraction (LEED) data reveal a well defined c(2x4) superlattice. These structures are distinctly different than either bulk MoO_3 or than ramified two-dimensional MoO_3 islands formed on Au(111) which were also recently reported.[15]

In this paper we demonstrate that the spatial distribution of the Mo clusters dictates the initial nucleation sites and the morphology of MoO_3 islands. In particular, nucleation of crystalline MoO_3 islands *on* Au(111) terraces was observed after oxidation of ordered 2D arrays of Mo nanostructures by NO_2 exposure. Such ordered arrays of Mo nanostructures can be prepared by physical vapor deposition (PVD) of Mo, and are a consequence of the preferred nucleation of Mo at elbow sites of the reconstruction of the Au(111) surface. The spatial distribution of the Mo clusters controls the initial nucleation sites of MoO_3 islands despite the fact that long-range mass transport is necessary to explain the observed growth kinetics. Furthermore we show that the exact morphology of the MoO_3 islands strongly depends not only on the deposition method but also on other preparation conditions such as deposition, oxidation and annealing temperature.

Experimental

All experiments were performed in a commercial ultrahigh vacuum (UHV) system with a base pressure of $5x10^{-11}$ mbar. The system has separate compartments for sample preparation, e.g. Mo evaporation, and sample characterization. The characterization compartment is equipped with commercial instrumentation for scanning probe microscopy (SPM) (Omicron), Auger electron spectroscopy (AES) and low energy electron diffraction (LEED).

The Au(111) sample was cleaned by repeated cycles of sputtering with 1000 eV energy Ar^+ for 60 minutes with an ion current of 4 μA at room temperature. Subsequently the sample was annealed for 10 min at 900 K followed by one hour at 700 K. This procedure was repeated until no contaminants were detected by means of AES. The sample was radiatively heated, and the temperature was monitored using a Cr-Al thermocouple attached

to the manipulator. Initially the temperature was calibrated by a Cr-Al thermocouple spot-welded to a sample holder plate. Annealing times given in the text do not include the ramp-up time which was typically ~ 10 minutes.

Molybdenum (Goodfellow, 99.9%) was evaporated from rod material (1.5 mm diameter) using an electron beam evaporator (Omicron) (900 V / ~ 65 mA). The deposition rate was monitored continuously by a flux monitor measuring the ion flux, which is approximately proportional to the flux of evaporated atoms. Using the flux monitor to determine the exposure, a specific coverage could be achieved with a reproducibility of +/- 10 %. Initially the deposition rate was calibrated using a quartz thickness monitor. All preparations in this publication were performed using a flux of ~0.25 to 0.75 ML Mo min^{-1}. Evaporated molybdenum was oxidized by exposure to nitrogen dioxide (Matheson, 99.5%) at a typical pressure of 1-2 x 10^{-7} mbar. The purity of NO_2 was periodically checked with a residual gas analyzer.

STM images were collected either at room temperature or at elevated temperatures (if indicated), and Z-channel (topography) and I-channel (constant height) images were obtained simultaneously. Etched $Pt_{0.8}$ $Ir_{0.2}$ tips from Molecular Imaging were used for imaging.

Results and Discussion

The growth mechanism of nanocrystalline, single-layer MoO_3 islands during oxidation of Mo cluster arrays on Au(111) surfaces was investigated by in-situ STM (figure 1). The arrays of Mo nanoclusters were prepared by PVD of 0.3 ML Mo at 500 K. As recently reported[16] and reproduced in our laboratory[17] Mo clusters prepared by PVD nucleate preferentially at the elbow sites of the herringbone reconstruction. These Mo clusters were subsequently oxidized by incremental NO_2 exposure at 500 K which leads to nucleation of MoO_3 islands on the Au(111) surface. STM images were collected *at* 500 K between each oxidation step. During NO_2 exposure the STM tip was retracted, as otherwise a tip shadowing effect in terms of a reduced oxidation rate was observed. In the initial reaction regime the apparent height of the Mo clusters increases from 0.5 nm to 1 nm with increasing NO_2 exposure. Simultaneously, the long-range order of Mo cluster arrays diminishes. However, the unimodal size distribution of the Mo clusters remains. Starting at an exposure of ~14L

NO_2, 2D MoO_3 islands are observed to nucleate, initially at step edges and later on the terraces. A local depletion of Mo clusters around growing MoO_3 islands was not observed. With increasing NO_2 exposure the MoO_3 islands grow in size, and finally the Mo cluster density starts to decrease.

The observed growth kinetic of the MoO_3 islands indicates a non-local, long-range mass transport of MoO_3 precursor species from oxidized Mo clusters to growing MoO_3 islands. The nearly constant Mo cluster density in the initial MoO_3 growth regime reveals that existing Mo clusters contribute evenly by 2D evaporation of volatile species (most likely $(MoO_3)_x$, see below) to the observed mass transport; premature dissolution of individual Mo clusters in the vicinity of growing MoO_3 islands, i.e. the formation of a depletion zone, was not observed. A quantitative analysis of the experiment demonstrates that the initially uniform Mo coverage of ~0.3 ML (e.g. in fig. 1a) transforms into a local coverage of 0.5 ML MoO_3 on the narrow terrace running through the center of the image in figure 1d. This observation reveals that long-range mass transport takes place even across steps. This long-range mass transport was also observed in our previous study of the MoO_3 formation using CVD.

It is remarkable that the spatial distribution of the Mo clusters influences the spatial distribution of MoO_3 islands although long-range mass transport is a prerequisite to explain the observed growth kinetics. In contrast to the step-edge decoration observed in our previous study of MoO_3 using CVD of the Mo,[14] the PVD approach described in the present study leads to preferred nucleation of MoO_3 islands *on* terrace sites. This behavior is even more pronounced on surface areas with a low step density (see e.g. figures 3-6). This "memory" effect strongly suggests that oxidized Mo clusters serve as nucleation sites. However, as the density of MoO_3 islands is much lower than the density of Mo clusters prior to oxidation, the majority of the Mo clusters must dissolve during oxidation via formation of mobile MoO_3 species. Indeed, volatile $(MoO_3)_n$ (n = 3, 4, 5) species have been previously detected by mass spectrometric studies during sublimation of MoO_3 bulk oxide.[18]

The MoO_3 islands have a well-defined crystalline structure with a c(4x2) unit cell, based on our STM and LEED data (figure 2). The LEED pattern displayed in figure 2a is

identical to the LEED pattern previously observed from MoO_3 islands on Au(111) prepared by CVD.[14] High resolution STM data reveal a rectangular unit cell with dimensions of 0.50 x 0.57 nm^2 ± 10% (figure 2b), consistent with the observation of the c(2x4) LEED pattern. Thus the atomic structure of MoO_3 islands prepared by PVD is identical to the structure of MoO_3 islands using CVD to deposit the Mo.[14] MoO_3 on Au(111) forms a single layer structure which differs from the bilayer structure of bulk MoO_3.[19] The single layer MoO_3 islands exhibit an apparent height of ~ 0.5 nm and the atomic structure can be explained in terms of an ordered, two-dimensional array of interacting MoO_3 entities. X-ray photoelectron experiments revealed that the predominant oxidation state of Mo (> 90%) in single layer molybdenum oxide islands prepared on Au(111) is +6.[20]

STM images of individual islands often reveal defect structures (indicated by arrows in fig. 2b); sometimes, in a quasi-regular superlattice. Repeated scanning of an island leads to an increase in the defects present, suggesting that the STM tip may induce additional defects. Ordered arrays of defects are commonly caused by the presence of strain, as for example the herringbone reconstruction of the Au(111) surface. Indeed, the unit cell of single layer MoO_3 on Au(111) is ~2% smaller than the unit cell of the (010) plane of bulk MoO_3, suggesting a compressive stress. X-ray photoelectron data show that most of the Mo is in the +6 oxidation state, but that ~10% has a +5 oxidation state indicating the existence of defects.

The MoO_3 islands on terrace sites reflect the symmetry of the Au(111) surface, based on our STM and LEED measurements (figures 2, 3). Specifically, the MoO_3 islands shown in figure 3a were prepared by deposition of 0.3 ML Mo at 600 K and subsequent exposure to 20 L NO_2 at 600 K. The islands have a characteristic, hexagonal shape with a typical aspect (length : width) ratio of ~ 2.5. The long island edges run parallel to the herringbone structure of the Au(111) surface, i.e. parallel to the [11-2] directions of the underlying substrate. In some instances, rotational domains coalesce as they grow to form “sock-like” structures with a 120 degree bend, reflecting the three-fold symmetry of the underlying Au. Qualitative analysis of STM images reveals an average island width of ~19 nm (with a standard deviation of 4 nm) corresponding to 3 times the width of the herringbone structure.

The elongated shape of the MoO_3 islands on the terraces is a consequence of kinetic control of the growth. Indeed, the elongated nanostructures grown at 600 K assume a more compact shape after annealing at 600 K for 10 minutes (figure 3b), clearly indicating the role of growth kinetics in the formation of the anisotropic shapes. The anisotropic growth could be due to anisotropic step edge diffusion,[21] i.e. different diffusion barriers for the growth species along the short and long edges of the MoO_3 islands. Specifically, the observed island shape implies a higher diffusion barrier of MoO_3 precursor species along the short island edges than along the long edges. This leads to a higher density of MoO_3 precursor species at short island edges, and thus to a higher nucleation probability. Furthermore the observation that the island width correlates with the width of the herringbone, as mentioned above, suggests that the diffusion barriers depend not only on the orientation but also on the position of the island edge with respect to the reconstruction.

The formation of MoO_3 islands leads to a lifting of the reconstruction under the islands, based on STM data. Specifically, the characteristic herringbone structure becomes disrupted and avoids the oxide islands (figure 3a insert). Occasionally "U-turns" of the herringbone pattern were observed. It is well known that the interaction with adsorbates can lift the herringbone reconstruction.[22, 23] Note that the lifting of the reconstruction of the Au under the oxide nanostructure creates a boundary between reconstructed and unreconstructed regions of the Au that could affect growth kinetics.

The morphology of the MoO_3 islands depends strongly on the Mo deposition temperature. Specifically, the formation of "embedded" MoO_3 islands on Au(111) was observed if the Mo was deposited at or above 525 K, as exemplified in the STM image obtained from a preparation at 600 K (figure 4). The embedded MoO_3 islands can be identified by their reduced apparent height as illustrated by the line scan shown in the insert. The crystalline structure of the embedded MoO_3 islands is identical to those growing on top of the Au terrace; however, the shape of the two types of MoO_3 islands is different: island A is embedded and has a round shape, whereas island B grows free on the terrace and has the shape of an elongated hexagon.

We attribute the formation of these embedded MoO_3 islands to vacancy formation via NO_2 induced de-alloying of a Mo-Au surface alloy. In other work, we found evidence for the formation of a substitutional Mo-Au surface alloy during Mo deposition at or above 525 K.[17] Subsequent oxidation of Mo triggers de-alloying, and the vacancies generated in this step aggregate into "vacancy islands" in the Au surface. These vacancy islands then serve as nucleation sites for the growth of MoO_3 islands, or annihilate at step edges. The fact that Au vacancy islands were not observed within a distance of ~150 nm from the step edges at 600 K is an indication of the diffusion length of the vacancies. For example, vacancy islands are not observed in the surface area displayed in figure 3a, as the three steps running across the image serve as annihilation site. We attribute the difference in shape to the imposition of boundary conditions on the growth of embedded MoO_3: vacancy islands dictate the shape of MoO_3 islands growing inside a vacancy island. Thus, the shape of the embedded MoO_3 islands is significantly different from the shape of MoO_3 islands formed without boundary conditions *on* the terraces.

The observation of partially filled vacancies in case of lower deposition and oxidation temperature suggests a diffusion-limited growth regime. Partially filled vacancy islands (VI in fig. 5) were observed after deposition of 0.3 ML of Mo at 525 K and subsequent oxidation by 20 L NO_2 exposure at 525 K. As observed when MoO_3 is prepared at 600 K, the islands nucleate at the step edges of the vacancy islands; however, the ripening process is slower at 525 K, and the mass transport of MoO_3 precursor species by surface diffusion is insufficient to completely fill the vacancy island. Thus the individual MoO_3 islands within a vacancy island do not coalesce within the annealing time. Occasionally, the herringbone pattern within a vacancy island could be resolved (fig. 5b insert), confirming that the vacancy islands are in Au itself. Furthermore the density of small MoO_3 islands increases compared to the 600 K preparation described above. The height of an embedded MoO_3 island and a MoO_3 islands *on* the terrace is identical (fig. 5a) with respect to the underlying Au.

Kinetic control of the island growth is even more pronounced if the Mo clusters are oxidized at 450 K. While the regular, hexagonal shapes obtained after oxidation at 525 K and 600 K indicate that diffusion is sufficiently fast to approach an ordered state, oxidation at lower temperature leads to irregular shapes that indicate that the growth is kinetically limited.

For example, islands with less well-defined edges are obtained after oxidation of Mo (0.3 ML) deposited at 450 K and subsequently oxidized by exposure to 20 L NO_2 at 450 K (figure 6a). Most noteworthy is the large fraction of small islands and the ramified shape of the larger islands which exhibit a typical aspect ratio of approximately five with the long edge aligned parallel to the [11-2] directions of the Au(111) surface. In contrast to deposition and oxidation at 525 K or higher, vacancy islands are not observed. Instead, the formation of small Au islands is observed, which can, like step edges, serve as nucleation sites for MoO_3 islands. These Au islands can be identified by the herringbone pattern (fig. 6a inserts).

Our previous investigations[14, 17] suggest that some Au atoms are incorporated into the Mo clusters. Subsequent oxidation of the Mo clusters causes de-alloying, and the Au atoms released during this step then lead to the formation of small Au islands (6a insert). Alternatively, the Au islands might originate from the additional Au atoms of the herringbone reconstruction, which is lifted underneath the MoO_3 islands. A quantitative analysis is, however, not possible as the fraction of Au atoms which are released by the processes described above and form Au islands is unknown.

Ostwald ripening of the MoO_3 nanostructures is observed during annealing. Specifically, the irregular and elongated MoO_3 islands created by deposition and oxidation at 450 K assume a less anisotropic shape upon heating to 650 K for 10 minutes (fig. 6b). No loss of MoO_3 was observed during annealing to 650 K based on AES data (not shown). These changes are consistent with those observed if MoO_3 prepared at 600 K and subsequently imaged at room temperature (fig. 3a) was further annealed at 600 K for 10 minutes (fig. 3b).

The more compact shape should be more thermodynamically stable than an elongated irregular shape because the ratio of the perimeter length to area is smaller; thus, the number of unstable edge sites is reduced. Besides the change in shape, the islands also change in size: larger islands grow at the expense of smaller islands. The observed change of the island shape towards a more compact shape confirms our assertion that the elongated hexagonal shape observed prior to annealing is the result of anisotropic diffusion and, therefore, indicates kinetic control. The conversion towards the more stable island morphology is a slow process, even at 600 K, and requires further annealing after oxidation. According to STM and LEED

the unit cell structure of the MoO_3 islands is unaffected by the annealing to 650K. However, higher temperatures (700 K and above) lead to thermal reduction and the formation of shear planes as described elsewhere.[20]

This work provides a guide for synthesizing MoO_3 nanostructures with specific shapes and distributions on the Au surface. By controlling the shape and distribution of the islands on the surface, we are able to create different bonding environments that may affect the chemical and physical properties of the nanostructures. In particular, atoms at the periphery of the nanostructures have different bonding environments and coordination and may, therefore, have different chemical properties than in interior. Furthermore, we are able to create and image specific defects in these oxides that may create reactive centers or change the electronic and optical properties of these materials. We are currently investigating the chemical and physical properties of these materials to address these points.

Conclusion

Nanocrystalline MoO_3 islands on Au(111) terraces can be synthesized by PVD of Mo followed by oxidation using NO_2. Both shape and spatial distribution of the MoO_3 islands are in sharp contrast to the results of our previous investigations using a CVD approach to deposit molybdenum. CVD leads to preferential nucleation of MoO_3 at step-edges, and both island shape and orientation are dictated by boundary conditions induced by the presence of substrate step-edges. The main difference between the PVD approach described in this paper and the CVD approach reported earlier is the spatial distribution of the Mo clusters on the Au(111) surface prior to oxidation: terrace (PVD) versus step-edge decoration (CVD), respectively. Hence, the spatial distribution of the Mo clusters controls the initial nucleation sites of MoO_3 islands despite the fact that long-range mass transport is necessary to explain the observed growth kinetics.

Furthermore the morphology of the MoO_3 islands strongly depends on deposition and oxidation temperatures. For deposition temperatures at 525 K or above we observe NO_2 induced dealloying of a Mo-Au surface alloy formed during Mo deposition. This, in turn, leads to the observation of "embedded" MoO_3 islands, which nucleate at steps of Au vacancy islands. The oxidation temperature affects the growth kinetics of MoO_3 islands: diffusion of

MoO_3 precursor species is kinetically controlled at 450 K, which leads to an irregular shape of MoO_3 islands with a high aspect ratio. With further annealing the islands change in size and shape via Ostwald ripening.

The ability to synthesize nanostructures with different distributions and shapes is important for understanding how edge sites present in small structures and modification of materials due to boundary conditions imposed by the substrate affect chemical and physical properties. These issues are central to understanding complex, integrated nanostructures.

Acknowledgements:

We gratefully acknowledge the support of this work by the US Department of Energy, Basic Energy Science, under grant number DE-FG02-84ER13289 and by the Harvard University NSEC, funded by the National Science Foundation, grant no. PHY-01-17795. J.B. acknowledges current support under the auspices of the U. S. Department of Energy by the University of California, Lawrence Livermore National Laboratory, under Contract No. W-7405-Eng-48.

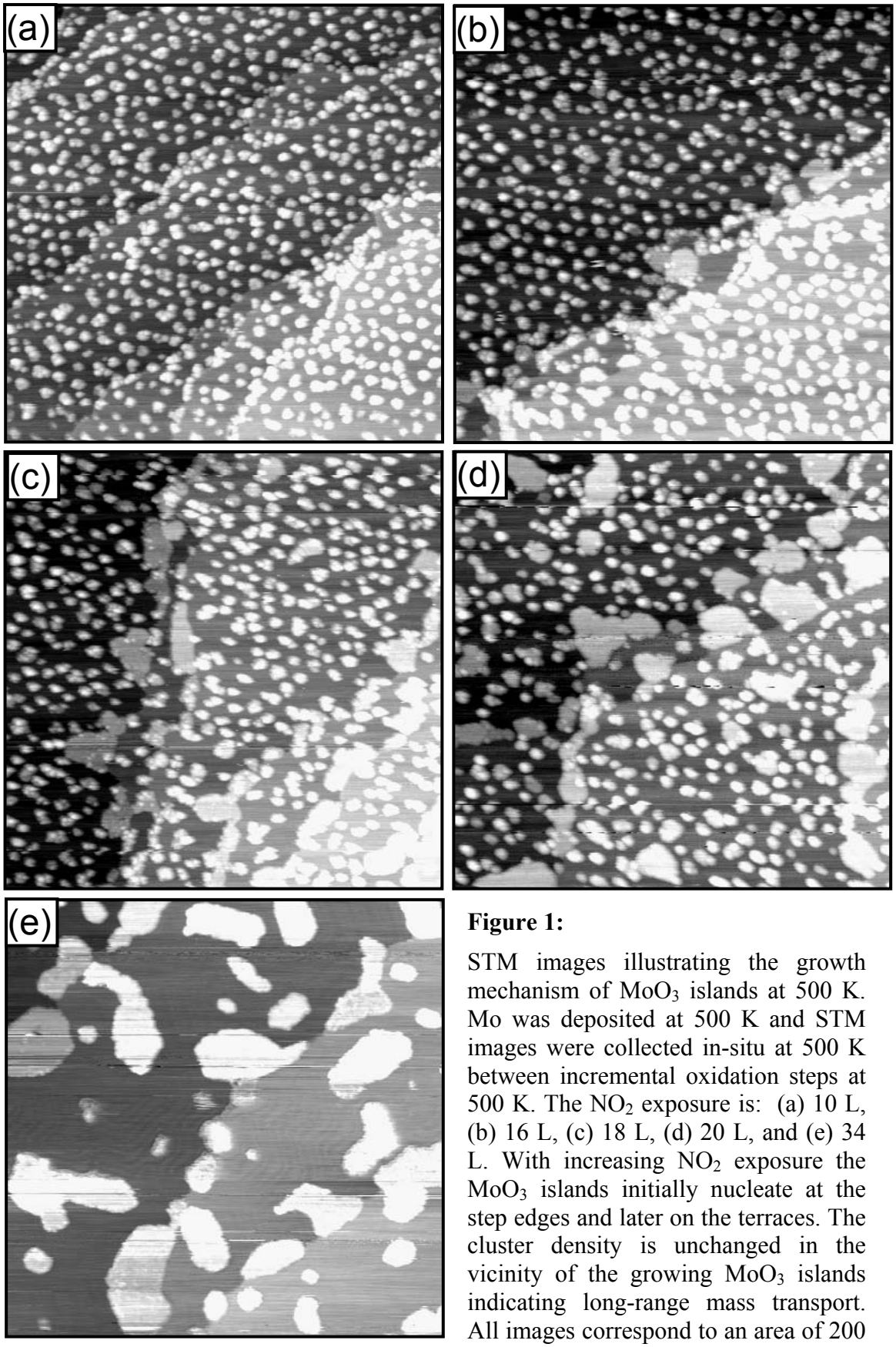

Figure 1:

STM images illustrating the growth mechanism of MoO_3 islands at 500 K. Mo was deposited at 500 K and STM images were collected in-situ at 500 K between incremental oxidation steps at 500 K. The NO_2 exposure is: (a) 10 L, (b) 16 L, (c) 18 L, (d) 20 L, and (e) 34 L. With increasing NO_2 exposure the MoO_3 islands initially nucleate at the step edges and later on the terraces. The cluster density is unchanged in the vicinity of the growing MoO_3 islands indicating long-range mass transport. All images correspond to an area of 200 nm x 200 nm.

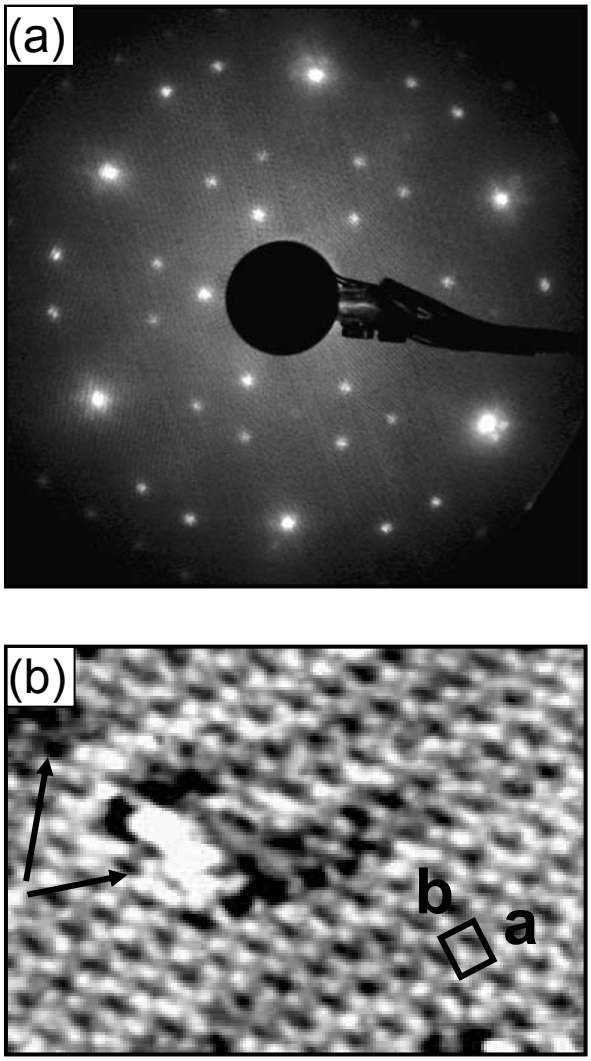

Figure 2:
Identification of the c(4x2) unit cell of the MoO_3 islands on Au(111) prepared by PVD of Mo and subsequent oxidation with NO_2 at 600 K: (a) LEED pattern obtained at 300 K revealing a c(4x2) structure, and (b) high resolution STM image (7 nm x 7 nm) showing a rectangular unit cell with a = 0.50 nm and b = 0.57 nm ±10%, obtained at 300 K. Defects are indicated by arrows.

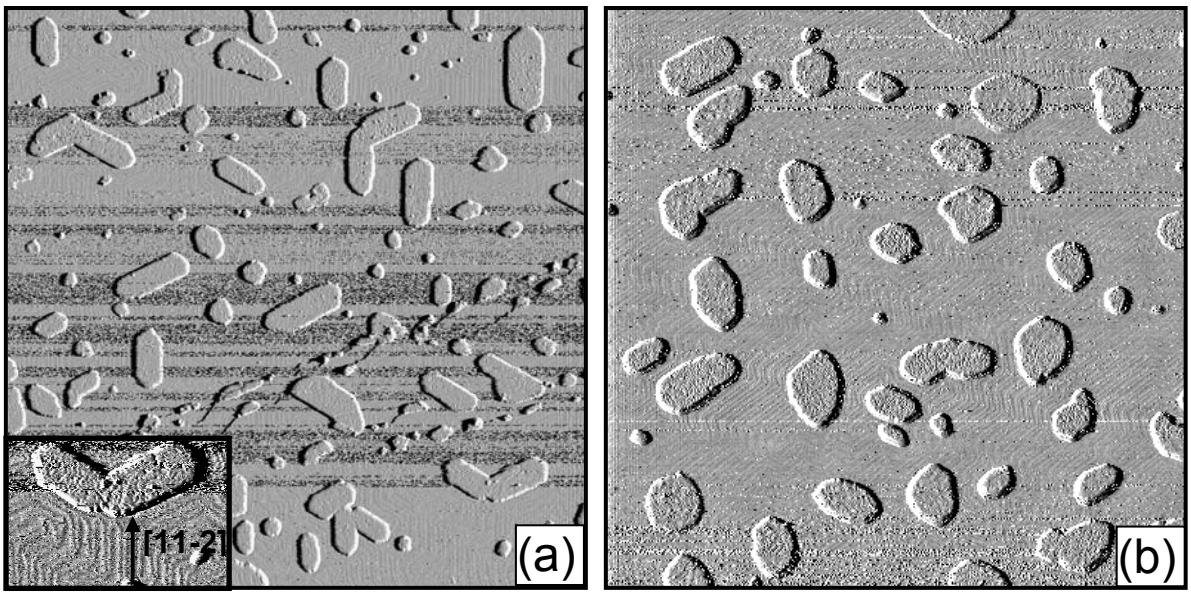

Figure 3:
STM image (I-channel) showing nanocrystalline MoO_3 islands on Au(111) after Mo deposition and subsequent oxidation by NO_2 exposure at 600 K (a).The islands nucleate predominantly on terraces and reveal a hexagonal shape with a high aspect ratio. The island edges are aligned with the [11-2] direction of the substrate. Further annealing at 600 K for 10 minutes leads to a more compact island shape (b). The images were obtained at 300 K and correspond to an area of 500 nm x 500 nm (insert in (a): 115 nm x 75 nm).

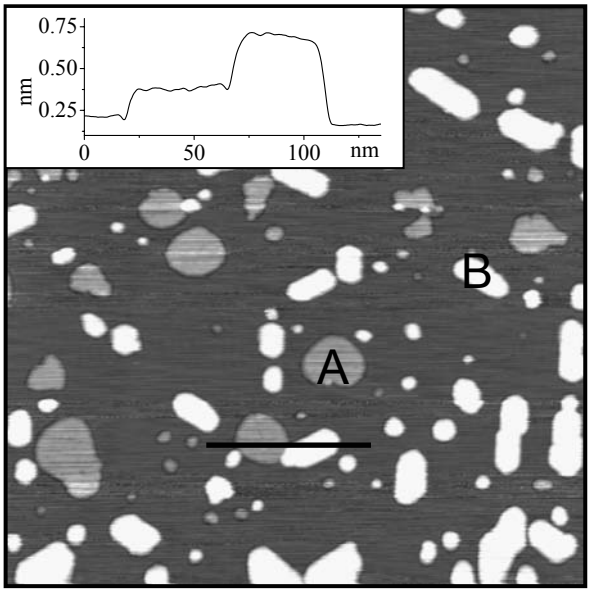

Figure 4:

STM image (Z-channel) showing two different types of MoO_3 islands prepared at 600K: island A is embedded and has a round shape, island B is on the terrace and has the shape of an elongated hexagon. A line scan along the indicated section is shown in the insert and illustrates the difference in the apparent height. The image corresponds to an area of 500 nm x 500 nm.

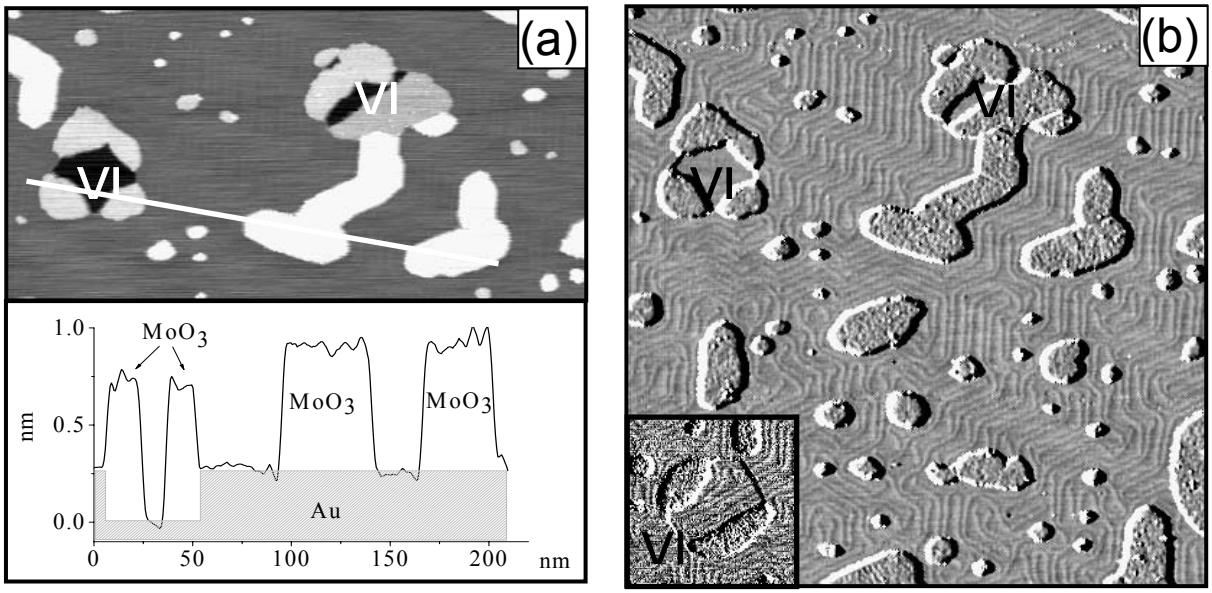

Figure 5:

STM images showing MoO_3 islands on Au(111) after Mo deposition and subsequent oxidation by NO_2 exposure at 525 K: (a) Vacancy islands (VI) on Au(111) partially filled with MoO_3. A line scan along the indicated section is shown in the insert and illustrates that the height of MoO_3 islands in vacancy islands and MoO_3 islands *on* terraces are identical with respect to the underlying Au. (b) STM image (I-channel) showing the alignment of the MoO_3 islands and the Au(111) reconstruction pattern in a vacancy island (insert). The images correspond to an area of 250 nm x 250 nm (insert 83 nm x 83 nm).

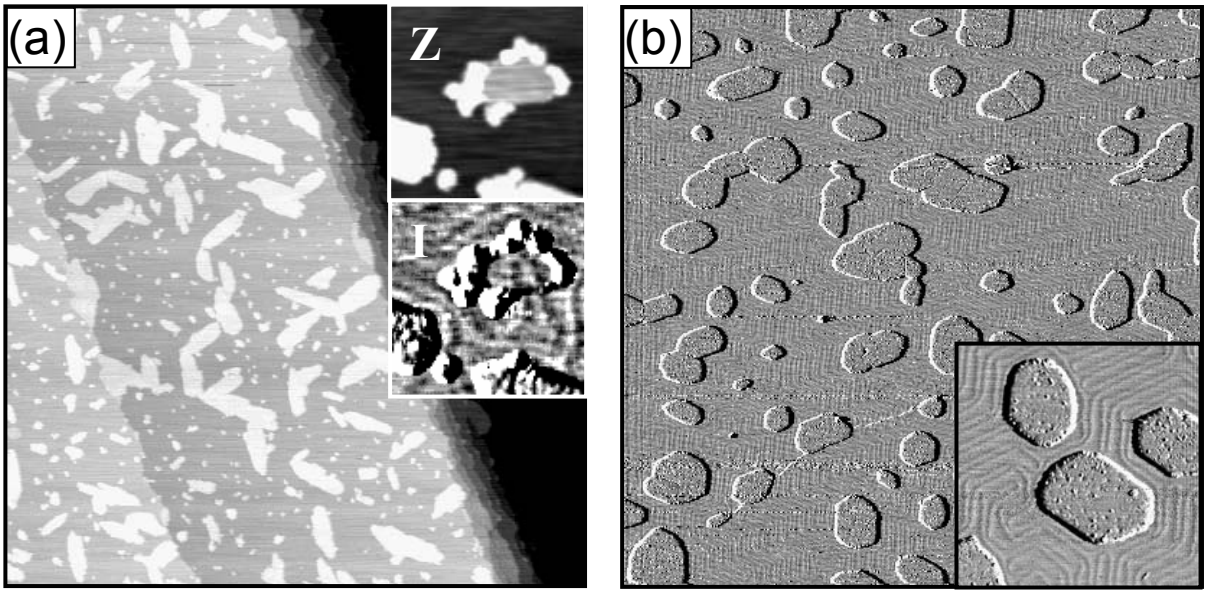

Figure 6:

STM images demonstrating Oswald ripening of MoO_3 islands on Au(111): (a) After deposition at 450 K MoO_3 islands are irregularly shaped; occasionally small Au islands are observed which can be identified by their reconstruction pattern (see inserts in I and Z channel, respectively). (b) A more compact MoO_3 island morphology is observed after annealing to 650 K for 10 min. The images correspond to an area of 500 nm x 500 nm, inserts in (a) to 33 nm x 33 nm, and (b) to 100 nm x 100 nm

References

[1] M. Valden, X. Lai, and D. W. Goodman, Science **281**, 1647 (1998).

[2] Z. P. Chang, Z. Song, G. Liu, et al., Surf. Sci. **512**, L353 (2002).

[3] J. A. Rodriguez, J. Dvorak, T. Jirsak, et al., Surf. Sci. **490**, 315 (2001).

[4] A. J. Jaworowski, M. Smedh, M. Borg, et al., Surf. Sci. **492**, 185 (2001).

[5] G. H. Smudde and P. C. Stair, Surf. Sci. **317**, 65 (1994).

[6] P. J. Spencer, United States Patent **4,607,127** (1986).

[7] N. D. Spencer and C. J. Pereira, AIChE Journal **33**, 1808 (1987).

[8] N. D. Spencer, J. Catal. **109**, 187 (1988).

[9] M. A. Banares, N. D. Spencer, M. D. Jones, et al., J.Catal. **146**, 204 (1994).

[10] M. Chen, C. M. Friend, and E. Kaxiras, J. Am. Chem. Soc. **123**, 2224 (2001).

[11] J. Haber and E. Lalik, Catal. Today **33**, 119 (1997).

[12] S. Surnev, L. Vitali, M. G. Ramsey, et al., Phys. Rev. B **61**, 13945 (1999).

[13] G. Ketteler and W. Ranke, J. Phys. Chem. B **107**, 4320 (2003).

[14] M. M. Biener and C. M. Friend, Surf. Sci. Lett. **559**, L173 (2004).

[15] Z. Song, T. Cai, Z. Chang, et al., J. Am. Chem. Soc. **125**, 8059 (2003).

[16] S. Helveg, J. V. Lauritsen, E. Laegsgaard, et al., Phys. Rev. Lett. **84**, 951 (2000).

[17] M. M. Biener, J. Biener, R. Schalek, et al., Phys. Rev. B (submitted).

[18] G. Demaria, R. P. Burns, J. Drowart, et al., J. Chem. Phys. **32**, 1373 (1960).

[19] E. Itoh, K. Hayakawa, and S. Oishi, J. Phys.: Condens. Matter **13**, 6853 (2001).

[20] X. Deng, M. M. Biener, J. Biener, et al., (to be published).

[21] T. Michely, M. Hohage, M. Bott, et al., Phys. Rev. Lett. **70**, 3943 (1993).

[22] D. Krznaric, T. Goricnik, and B. Cosovic, Croatica Chemica Acta **73**, 247 (2000).

[23] S. Strbac, O. M. Magnussen, and R. J. Behm, J. Serb. Chem. Soc. **66**, 119 (2001).

III

Submitted to: J. Chem. Phys., 19. August, 2004
Revised: 27. September, 2004

Novel synthesis of two-dimensional TiS_2 nanocrystallites on Au(111)

Monika M. Biener[1,2], Juergen Biener[3,4], and Cynthia M. Friend[1,2, †]
[1]Department of Chemistry and
[2]Division of Engineering and Applied Sciences and
[4]Center for Imaging and Mesoscale Structures
Harvard University
12 Oxford Street, Cambridge, MA 02138 USA
[3]present address: Nanoscale Synthesis and Characterization Laboratory
Lawrence Livermore National Laboratory
7000 East Ave, Livermore, CA 94550 USA

[†]Author to whom correspondence should be sent

Abstract

We describe a novel approach to synthesize two-dimensional nanocrystalline TiS_2 islands on Au(111). Ti is deposited by physical vapor deposition (PVD) at room temperature on AuS-covered Au(111) surfaces. Subsequent annealing to temperatures between 670 K and 800 K leads to the formation of single-layer, triangular TiS_2 islands. These TiS_2 nanocrystallites reflect the structure of bulk TiS_2, and are composed of S-Ti-S stacking units with hexagonally close-packed layers of sulfur atoms and titanium occupying the octahedral sites in between. The lattice constant of the hexagonal unit cell is 3.45 Å. A superlattice with a repeat distance of 17.3 Å results from the coincidence of 5 TiS_2 units with 6 Au atoms and is observed in scanning tunneling microscopy (STM) and low energy electron diffraction (LEED). The triangular shape of the islands indicates a preference for one of the two possible edge terminations. The observation of two island orientations rotated by 60° with respect to each other can be attributed to the formation of twin-related TiS_2 domains. The population of the two different island orientations changes during annealing at 800 K indicating a thermodynamic preference for one of the possible stacking sequences.

Introduction

Layered transition metal dichalcogenides with the general composition MX_2 (X = S, Se, Te) have many technological applications due to their highly anisotropic physical properties. These arise from strong covalent M-X intra-layer bonding contrasted by weak van-der-Waals inter-layer bonding. For example, mechanically flexible high-mobility field-effect transistors (FETs) can be based on transition metal dichalcogenides,[1] MoS_2 is widely used as a solid lubricant and TiS_2 is one of the most effective cathode materials for high energy rechargeable batteries.[2, 3] Furthermore, the layered structure of transition metal dichalcogenides allows the synthesis of fullerene-like and nanotube-like materials[4-6] with interesting electronic properties.[7, 8]

In the present work we focus on the synthesis of single-layer TiS_2 on Au(111). TiS_2 is a small-band-gap[9] semiconductor and a promising candidate for potential electronic applications due to its two-dimensional electronic structure. The structure of bulk TiS_2 can be regarded as hexagonally close-packed layers of S atoms with Ti occupying octahedral sites between every other pair of S layers. These S-Ti-S sandwiches are strongly bonded internally but only weakly coupled to each other by van-der-Waals forces. The lattice constant of the hexagonal unit cell of bulk TiS_2 is 3.45 Å.

Theoretical investigations predict that the electronic properties of an isolated S-Ti-S layer are different from those of the corresponding bulk material.[10] This theoretical work suggests that single-layer TiS_2 grown on a substrate may have interesting and unusual electronic properties. Hence, we devised a means of synthesizing nanometer scale single-layer islands on Au. Although thin films of TiS_2 have previously been prepared by chemical vapor deposition (CVD) or plasma assisted CVD using $TiCl_4$ and various S containing species such as H_2S and thiols as chemical precursors, these films are often amorphous and are contaminated with oxygen and carbon.[11-15]

Here, we describe a novel, two step method for synthesis of single-layer nanocrystalline TiS_2 islands on Au(111) surfaces. First, a two-dimensional AuS overlayer is prepared by decomposing SO_2, as described elsewhere.[16] During annealing at 450 K, the two-dimensional gold sulfide develops long-range order with a sulphur coverage of 0.5ML.[16, 17]

Second, Ti is deposited by physical vapor deposition (PVD) at room temperature on the AuS covered Au(111) surface which serves as a sulfur reservoir for TiS_2 formation. Nanocrystalline TiS_2 islands develop during subsequent annealing.

Experimental

The experiments were performed in a commercial ultrahigh vacuum system with a base pressure of $5x10^{-11}$ mbar. The system has separate compartments for sample preparation, e.g. Ti evaporation, and sample characterization. The characterization compartment is equipped with commercial instrumentation for scanning probe microscopy (SPM) (Omicron), Auger electron spectroscopy (AES) and low energy electron diffraction (LEED).

The Au(111) sample was cleaned by repeated cycles of sputtering with 1000 eV energy Ar^+ for 60 minutes with an ion current of 4 μA at room temperature. Subsequently the sample was annealed for 10 min at 900 K followed by one hour at 700 K. This procedure was repeated until no contaminants were detected by means of AES. The sample was radiatively heated, and the temperature was monitored using a Cr-Al thermocouple attached to the manipulator. Initially the temperature was calibrated by a Cr-Al thermocouple spot-welded to a sample holder plate.

Well-ordered AuS overlayers were prepared by exposing the clean Au(111) surface to SO_2 at a pressure of ~ 1 mbar for 15 min at room temperature in the load lock section of the system, followed by annealing at 450 K in vacuum for 10 minutes. The resulting AuS overlayer is well ordered, and contains a S coverage of 0.5 ML (1 ML is defined as the areal density of atoms in the (111) plane of Au, i.e. 1.4×10^{15} atoms cm^{-2}).[16]

Titanium (Aldrich, 99.99%) was evaporated from rod material (2.0 mm diam.) using an electron beam evaporator (800 V / ~ 30 mA). The deposition rate was monitored continuously by a flux monitor measuring the ion flux, which is approximately proportional to the flux of evaporated atoms. Using the flux monitor to determine the exposure, a specific coverage could be achieved with a reproducibility of ± 10 %. Initially the deposition rate was

calibrated using a quartz thickness monitor. All preparations in this publication were performed using a flux of ~0.3 ML Ti min^{-1}.

STM images were collected at room temperature, and Z-channel (topography) and I-channel (constant height) images were obtained simultaneously. Etched $Pt_{0.8}$ $Ir_{0.2}$ tips from Molecular Imaging were used for imaging. The sample bias voltage was set between +0.5 V and +2.0 V.

Results

Single-layer, triangular TiS_2 nanocrystallites supported on Au(111) were synthesized by physical vapor deposition (PVD) of Ti onto a two-dimensional (2D) AuS and subsequent annealing (Figure 1). The 2D AuS overlayer thereby acts as a sulfur reservoir; its formation and characterization is described in detail elsewhere.[16] Briefly, this AuS overlayer has a sulfur coverage of 0.5 ML, and is stable up to 450 K where it develops a well-defined complex LEED pattern.[16, 17] The characteristic vacancy island pattern of this surface (figure 1a) is a consequence of the dynamic rearrangement of the surface atoms during the formation of the 2D AuS overlayer caused by incorporation of Au atoms into the growing AuS layer. Atomic resolution STM images (not shown) reveal that both terrace *and* vacancy islands are completely covered with the 2D AuS overlayer.

Ti deposited on the AuS/Au(111) surface reacts at room temperature with sulfur atoms of the AuS film. The chemical interaction between Ti and S is suggested by a change in the line-shape of the sulfur LMM AES transition at 150 eV (not shown) indicating Ti-S bond formation. The large scale surface morphology (step height, size and shape of vacancy islands) is not affected by this interaction, however, the surface corrugation increases from less than 0.5 Å to approximately 2 Å upon Ti deposition, as shown for deposition of 0.25 ML Ti at room temperature (Figure 1b).

The Ti-AuS/Au(111) surface develops a granular morphology upon subsequent annealing at 450 K for 10 min. Small protrusions develop on the terraces, suggesting that small TiS_x particles are formed (fig 1c). In addition, irregularly-shaped one monolayer deep vacancies appear in the Au surface. Both TiS_x particles and vacancies grow in size (fig 1d)

after further heating to 550 K for 10 min, indicating the onset of long-range ordering. The vacancies develop a more defined shape reflecting the symmetry of the Au(111) surface, and the TiS_x particles start to assume a triangular shape.

Two-dimensional triangular TiS_2 nanocrystallites are formed after annealing to 670 K for 10 min (figure 1e). The islands exhibit a broad size distribution, ranging from approximately 3 nm to 30 nm, and are aligned with the close-packed rows of the Au(111) surface. The observation of two different orientations rotated by 60^o with respect to each other indicates the presence of twin-related domains (see discussion below). The apparent height of the islands is 2.5 Å. The TiS_2 nanocrystals are evenly distributed on the surface. There is no evidence for preferential nucleation at step edges.

The TiS_2 stoichiometry of the islands observed after depositing Ti in a ratio of 1:2 relative to S present in the AuS surface layer was inferred from a combination of AES and STM experiments. According to AES the sulfur coverage, as monitored by the S_{150}/Au_{239} AES peak ratio, does not change during annealing to 670 K. Notably, previous experiments[16] showed that AuS starts to decompose above 450 K via desorption of S. Thus the sulfur which was originally incorporated in the AuS layer must be completely consumed by the reaction with the deposited Ti leading to the formation of triangular titanium sulfide islands. The complete consumption of S by Ti is consistent with the reappearance of the Au(111) reconstruction pattern (figure 1e inset), as even small S coverages (<0.1 ML) lift the reconstruction of the Au(111) surface.[16] Thus the composition of the triangular islands can be identified as TiS_2, as the initial S coverage was 0.5 ML and the amount of deposited Ti was 0.25 ML. The atomic structure as revealed by high-resolution STM and LEED experiments (shown below) further evidences the formation of TiS_2.

The triangular TiS_2 islands grow in size and develop a preferential orientation during further annealing to 800 K (figure 1f). Less than 25% of islands are pointing to the right (R-type) and all of them are smaller than 35 nm, whereas islands pointing to the left (L-type) grow up to a size of 80 nm. In contrast, a correlation between size and orientation was not observed after annealing to 670 K (fig 1e) where the number of R- and L-type islands as observed with STM is approximately equal. The herringbone reconstruction develops long-

range order, and is lifted underneath the TiS_2 islands reflecting the interaction between TiS_2 and Au (figure 1f, inset). The shape and orientation of the TiS_2 islands will be discussed in detail below.

The LEED pattern obtained from the two-dimensional TiS_2 islands grown on Au(111) shown in Figure 1f reveals a hexagonal unit cell with a lattice constant of 3.45 Å, in excellent agreement with the lattice constant of bulk TiS_2 (figure 2a). The observed LEED pattern can be explained by a model in which a hexagonal S-Ti-S sandwich layer matches the hexagonal Au(111) lattice with a "5-on-6" coincidence lattice causing the appearance of a Moire pattern. Figure 2b illustrates the "5-on-6" coincidence lattice of 2D TiS_2 islands relative to the Au(111) surface. The assignment of the LEED spots is as follows: The bright, hexagonally arranged spots marked with a square correspond to the Au(111)-(1x1) substrate spots. The (1x1) spots of the TiS_2 overlayer (filled circles) are orientated along the Au(111) lattice directions, but are located closer to the specular beam. The difference of the reciprocal vectors for Au and TiS_2 reveals a lattice constant of 3.45 Å for the TiS_2 unit cell and thus a lattice mismatch of 20%, consistent with the "5-on-6" coincidence structure. The hexagonally arranged satellite spots (open circles) around the TiS_2 (1x1) spots (filled circles) can be explained by diffraction at the large "5-on-6" coincidence lattice.

High-resolution STM images of nanocrystalline TiS_2 supported on Au(111) are consistent with the "5-on-6" coincidence structure. A well-ordered Moire pattern with a periodicity of ~18 Å (figure 3a) and a hexagonal unit cell with a lattice constant of ~ 3.6 Å (figure 3b) are observed in STM. The hexagonally arranged protrusions observed in atomically resolved STM images of TiS_2 nanocrystallites can be attributed to the positions of the sulfur atoms in the topmost sulfur layer, as the Ti atoms are too far apart to contribute to the tunneling current.[18] The STM images shown in figure 3 demonstrate the excellent order of the TiS_2 islands; only a few defects are observed.

The formation of two-dimensional TiS_2 islands consisting of a single S-Ti-S sandwich layer is in agreement with the observed TiS_2 coverage. Starting with Ti and S coverages of 0.25 and 0.5 ML, respectively, and using the lattice constant of 3.45 Å for the hexagonal unit cell of TiS_2, one would expect a TiS_2 coverage of 0.35 ML, in good agreement with the

experimental value of 0.3 ML obtained from large scale STM images. These monolayer TiS_2 islands exhibit an apparent height of 2.5 Å in STM.

The triangular shape of the TiS_2 islands after annealing to 670 K or above (Fig. 4a) indicates a preferred edge termination of the TiS_2 islands. In principle, the hexagonal symmetry of the TiS_2 sandwich layer allows two types of closed-packed edge orientations with different atomic arrangements, the (10-10) edge and the (-1010) edge, respectively (Figure 5a). The observation of a triangular morphology indicates that one of the two possible edge terminations is preferred over the other.[19] This could be controlled by thermodynamics or by kinetics. In any case the edge energies are crucial.

In some cases TiS_2 islands with a hexagonal shape were observed at Au step edges or on top of Au islands. Under those circumstances the shape of the TiS_2 islands is imposed by boundary conditions and therefore reflects the hexagonal symmetry of the Au(111) surface. An example is indicated by the arrow in the upper right corner of the STM image shown in figure 1e.

The observation of two island orientations rotated by 60 degrees with respect to each other can be explained by the existence of different stacking sequences of the sulfur layers within the hexagonal S-Ti-S sandwich relative to the Au surface, e.g. "$A_SC_{Ti}B_S$" versus "$A_SB_{Ti}C_S$" stacking (figure 5b). Alternatively, the two island orientations can be explained by a different stacking sequence between the Au(111) substrate and the "5 on 6" coincidence lattice. In any case, TiS_2 islands with the same orientation, i.e. the same stacking sequence, can easily coalesce, whereas TiS_2 with different stacking sequences remain separated by domain boundaries. This behavior is indeed observed experimentally (figure 4b). A preference for one of the two island orientations was not observed after annealing to 670 K.

Both island growth and development of a preferred orientation during annealing reveal Ostwald ripening, as illustrated by STM images obtained after annealing at 800 K (Figure 4c). The number of R-type islands decreases while the number of L-type islands increases suggesting that the latter are thermodynamically more stable. We never observed hexagonal islands (with the exception of those growing on Au islands) as intermediates between R- and L-type islands. Thus we conclude that R-type islands are not directly

converted to L-type islands, but exhibit a higher 2D evaporation rate leading to an effective mass transport from R to L-type islands. The mobile species is probably a TiS_2 molecule as this entity was identified as a product of the gas phase reaction between Ti and S atoms.[20]

R- and L- type islands differ only in the stacking sequence relative to the substrate, either within the S-Ti-S sandwich or at the TiS_2-Au interface. In any case, this results in a different interface environment, even in case of identical TiS_2 edge terminations. The development of a preferred island orientation indicates that the different interface environments are energetically distinct. This difference is also reflected by the interaction of the TiS_2 islands with the surrounding herringbone pattern, as observed by STM (figure 4d): L-type islands are surrounded by fcc areas of the Au(111) reconstruction and R-type islands are surrounded by alternating hcp and fcc areas, respectively. This indicates that the strain field of the Au(111) surface layer is affected by the TiS_2-Au interface environment. A similar effect was observed for close-packed steps on a clean Au(111) surface: the arrangement of the herringbone dislocation lines in the vicinity of the steps depends drastically on the step microstructure.[21]

TiS_2 islands on Au(111) are stable up to at least 800 K. Further heating to 930 K leads to a decrease in the TiS_2 coverage. Figure 6 (top) shows the normalized Ti_{418}/Au_{239} and S_{150}/Au_{239} AES peak ratios for an initial Ti coverage of 0.25 ML as a function of the annealing temperature. Both Ti and S coverages are constant up to 800 K and decrease simultaneously to zero after further annealing to 930 K. The constant S coverage between 450 K and 800 K is consistent with a stoichiometric educt ratio for TiS_2 formation. In comparison, deposition of 0.1 ML Ti on AuS/Au(111) leads to an incomplete transfer of S to Ti: excess S in form of AuS desorbs between 450 K and 550 K (figure 6 bottom), consistent with other work.[16] Thus the reaction with Ti stabilizes S up to 800 K.

Discussion

Titanium which is deposited at room temperature readily reacts with the S atoms of the AuS overlayer, as suggested by the observed change in the sulfur AES line shape, indicating a low activation barrier for this chemical interaction. This is remarkable as the tabulated values of the bond strengths in the diatomic molecules Au-S and Ti-S are identical

(418 kJ/mol) and thus do not provide a driving force for the observed reaction.[22] However, the bond strength of diatomic molecules may differ considerably from the bond energies in the corresponding 2D surface layers.

TiS_2 as bulk material has a layered structure with weak coupling (van der Waals forces) between individual S-Ti-S sandwich layers. Thus, a S-Ti-S layer can be expected to interact only weakly with the Au(111) surface. Indeed, the single layerTiS_2 on Au(111) exhibits the bulk structure of TiS_2. The lattice mismatch of 20% between the TiS_2 layer and the Au surface is accommodated by the formation of a "5-on-6" coincidence lattice, which causes a variety of different S-Au coordination geometries and thus S-Au binding energies within the 5-on-6" superlattice cell. The energy cost of S not solely occupying high symmetry sites, such as the three-fold hollow sites, is obviously smaller than the energy necessary to distort the structure, which is consistent with a van-der-Waals type of interaction.

Similar observations have been made for MoS_2 nanocrystallites on Au(111).[23, 24] Helveg et.al.[24] first reported the synthesis of ~30 Å wide MoS_2 islands on Au(111) by deposition of Mo in a H_2S ambient. Atomic resolution STM images revealed that the single layer MoS_2 islands exhibit the structure of bulk MoS_2 except a reconstruction of the edge sites. A MoS_2 island with the bulk structure of MoS_2 should give rise to the observation of a "9 on 10" coincidence lattice. However, a Moire pattern was not observed as the coincidence superlattice cell is larger than the island size of ~ 30 Å. Using the same approach as in the present work - i.e. deposition of Mo onto AuS - we recently synthesized larger MoS_2 crystallites on Au(111) which indeed produce the expected Moire pattern. We also observed pronounced edge sites as described by Helveg.[24] Our resolution is, however, not good enough to resolve the edges atomically. A pronunciation of the edge sites was not observed in case of TiS_2.

Another similar system which was recently investigated is RuS_2 nanoislands on Au(111).[25] Ru was deposited via CVD using $Ru(CO)_{12}$ as a precursor and S deposition was carried out via a solid-state electrochemical cell.

Recent theoretical work on single slabs of TiS_2 reveals that the electronic properties of these slabs are significantly different from bulk TiS_2: single layer TiS_2 is semiconducting whereas bulk TiS_2 is semimetallic.[10] The difference in electronic properties is caused by quantum confinement. These theoretical studies suggest that the two-dimensional TiS_2 nanocrystals synthesized on Au(111) may have interesting electronic and chemical properties. Further work is planned to elaborate on these issues.

Conclusion

Two-dimensional nanocrystalline TiS_2 islands were synthesized on Au(111) by using a 2D AuS overlayer as a source of sulfur. Single-layer, triangular TiS_2 islands form after depositing Ti via physical vapor deposition (PVD) at room temperature and subsequent annealing. Annealing up to 800 K leads to the formation of TiS_2 nanocrystals with the same unit cell dimensions as bulk TiS_2. These islands are composed of S-Ti-S stacking units with hexagonally close-packed S layers and titanium occupying the octahedral sites in between. The TiS_2 islands have a hexagonal unit cell with a lattice constant of 3.45 Å and form a Moire superlattice on the Au(111) which results from the coincidence of 5 TiS_2 units with 6 Au atoms based on both, STM and LEED. The triangular shape of the islands indicates a preference for one of the two possible edge terminations. The growth of the islands and the development of a preferred orientation upon annealing are consistent with Ostwald ripening.

Acknowledgements

We gratefully acknowledge the support of this work under the auspices of the Harvard MRSEC supported by NSF Grant no. DMR-02-13805. J. B. acknowledges current support under the auspices of the U. S. Department of Energy by the University of California, Lawrence Livermore National Laboratory, under Contract No. W-7405-Eng-48.

References

1 V. Podzorov and M. E. Gershenson, Appl. Phys. Lett. **84**, 3301 (2004).

2 M. S. Whittingham, Solid State Ionics **134**, 169 (2000).

3 M. S. Whittingham, Science **192**, 1126 (1972).

4 L. Margulis, G. Salitra, R. Tenne, et al., Nature **365**, 113 (1993).

5 R. Tenne, L. Margulis, M. Genut, et al., Nature **360**, 444 (1992).

[6] R. Tenne, M. Homyonfer, and Y. Feldman, Chem. Mater. **10**, 3225 (1998).
[7] G. L. Frey, S. Elani, M. Homyonfer, et al., Phys. Rev. B **57**, 6666 (1998).
[8] G. Seifert, H. Terrones, M. Terrones, et al., Solid State Commun. **114**, 245 (2000).
[9] C. Wang, L. Dotson, M. McKelvy, et al., J. Phys. Chem. **99**, 8216 (1995).
[10] C. M. Fang, R. A. de Groot, and C. Haas, Phys. Rev. B **56**, 4455 (1996).
[11] J. Cheon, J. E. Gozum, and G. S. Girolami, Chem. Mater. **9**, 1847 (1997).
[12] S. Kikkawa and M. Miyazaki, J. Mater. Res. **5**, 2894 (1990).
[13] S. Kikkawa, R. Shimanouchi-Futagami, and M. Koizumi, Appl. Phys. A **49**, 105 (1989).
[14] H. S. W. Chang and D. M. Schleich, J. Solid State Chem. **100**, 62 (1992).
[15] T. S. Lewkebandara and C. H. Winter, Adv. Mater. **6**, 237 (1994).
[16] M. M. Biener, J. Biener, and C. M. Friend, in preparation.
[17] M. Kostelitz, J. L. Domange, and J. Oudar, Surf. Sci. **34**, 431 (1972).
[18] H. Martinez, C. Auriel, and G. Pfister-Guillouzo, Mater. Res. Bull. **35**, 1643 (2000).
[19] C. Busse, C. Polop, M. Mueller, et al., Phys. Rev. Lett. **91**, 056103 (2003).
[20] B. Liang and L. Andrews, J. Phys. Chem. A **2002**, 6295 (2002).
[21] V. Repain, J. M. Berroir, S. Rousset, et al., Appl. Surf. Sci. **162**, 30 (2000).
[22] *CRC Handbook of Chemistry and Physics* (CRC Press, Boca Raton, 1996).
[23] J. V. Lauritsen, M. V. Bollinger, E. Laegsgaard, et al., J. Catal. **221**, 510 (2004).
[24] S. Helveg, J. V. Lauritsen, E. Laegsgaard, et al., Phys. Rev. Lett. **84**, 951 (2000).
[25] T. H. Cai, Z. Song, J. A. Rodriguez, et al., J. Am. Chem. Soc. **126**, 8886 (2004).

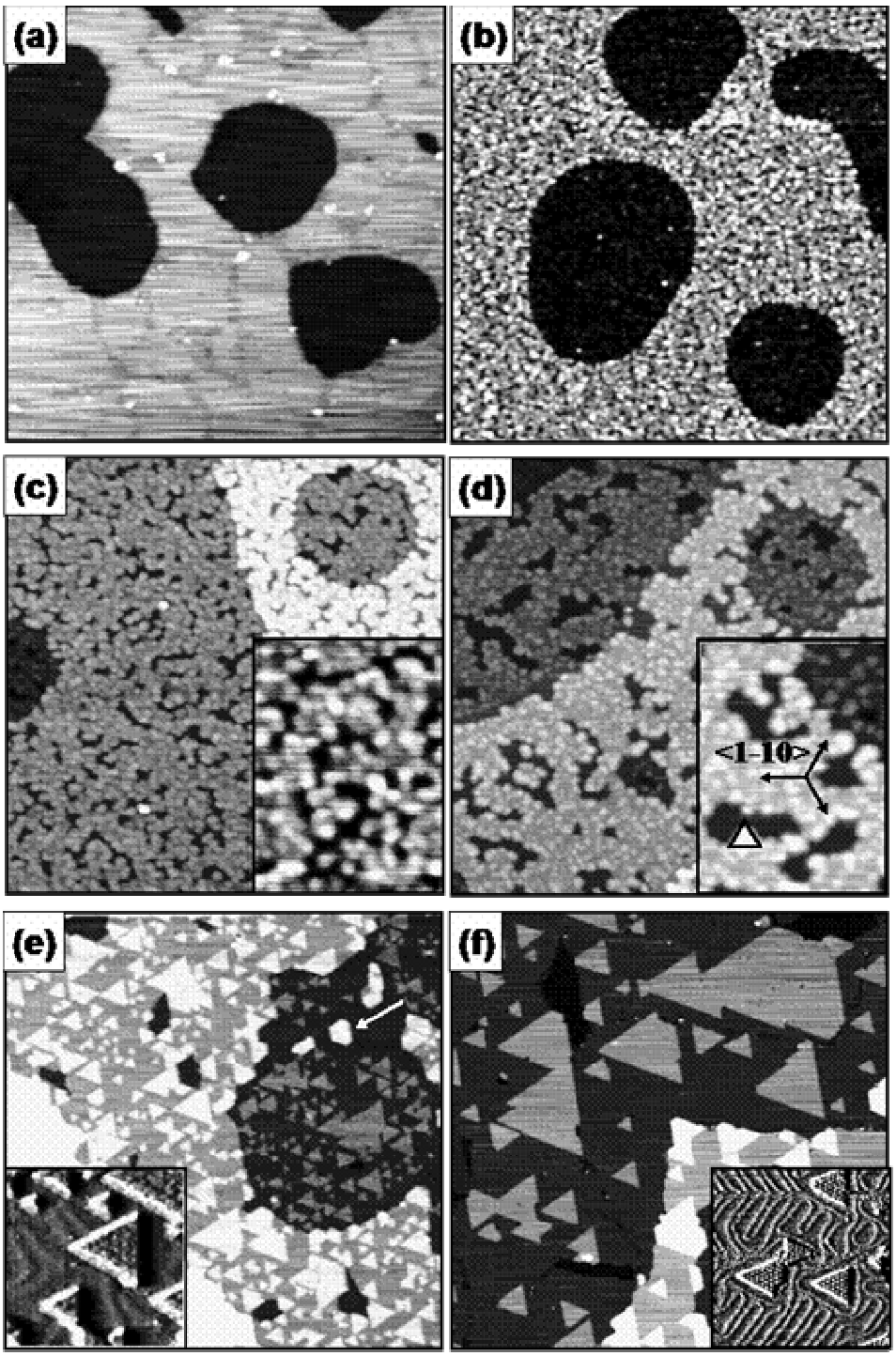

Figure 1: STM images (Z-channel) showing the formation of TiS_2 nanocrystals after deposition of Ti on AuS/Au(111): (a) as-prepared AuS film on Au(111) with a characteristic vacancy island pattern,; (b) after deposition of 0.25 ML Ti at room temperature; and after consecutive heating to (c) 450 K, (d) 550 K, (e) 670 K, and (f), 800 K for 10 minutes leads to the formation of TiS_2 nanocrystals. All images were obtained at room temperature, (a)-(e) correspond to an area of 250 x 250 nm^2, (f) 350 x 350 nm^2 (insets c,d: 50 x 67 nm^2, e: 36 x 36 nm^2, f: 73 x 73 nm^2).

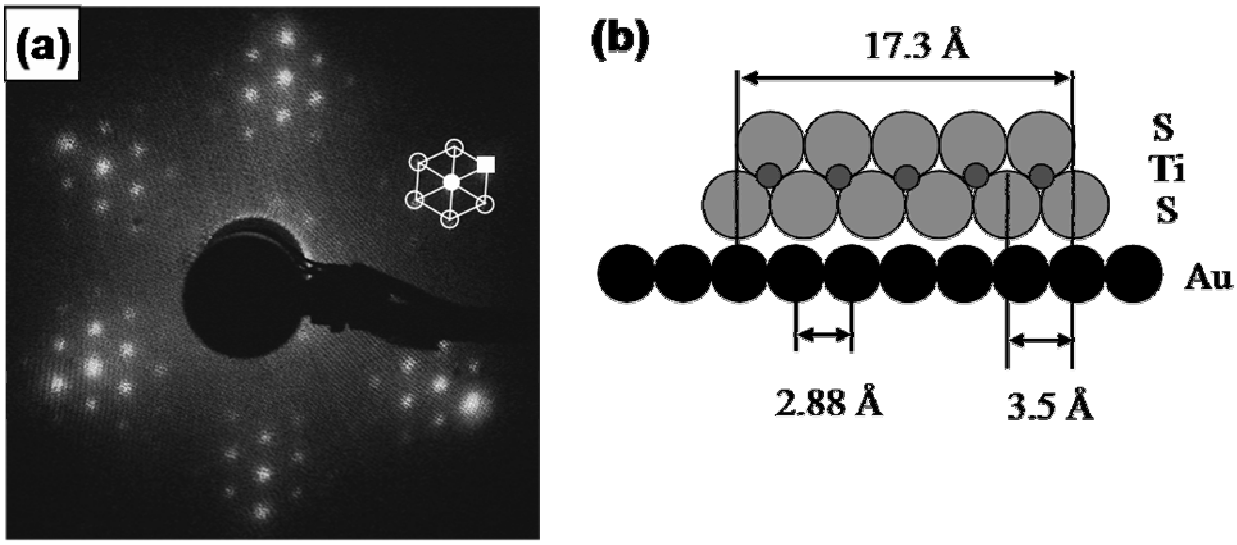

Figure 2: (a) LEED pattern obtained from the TiS_2 islands grown on Au(111) and shown in Figure 1f (0.25 ML Ti deposited at room temperature and annealed up to 800). The bright, hexagonally arranged spots marked with a square correspond to the Au(111)-(1x1) substrate spots. The (1x1) spots of the TiS_2 overlayer (filled circles) are orientated along the Au(111) lattice directions, with hexagonally arranged satellite spots (open circles) that can be explained by diffraction at the large "5 on 6" coincidence lattice shown schematically in (b).

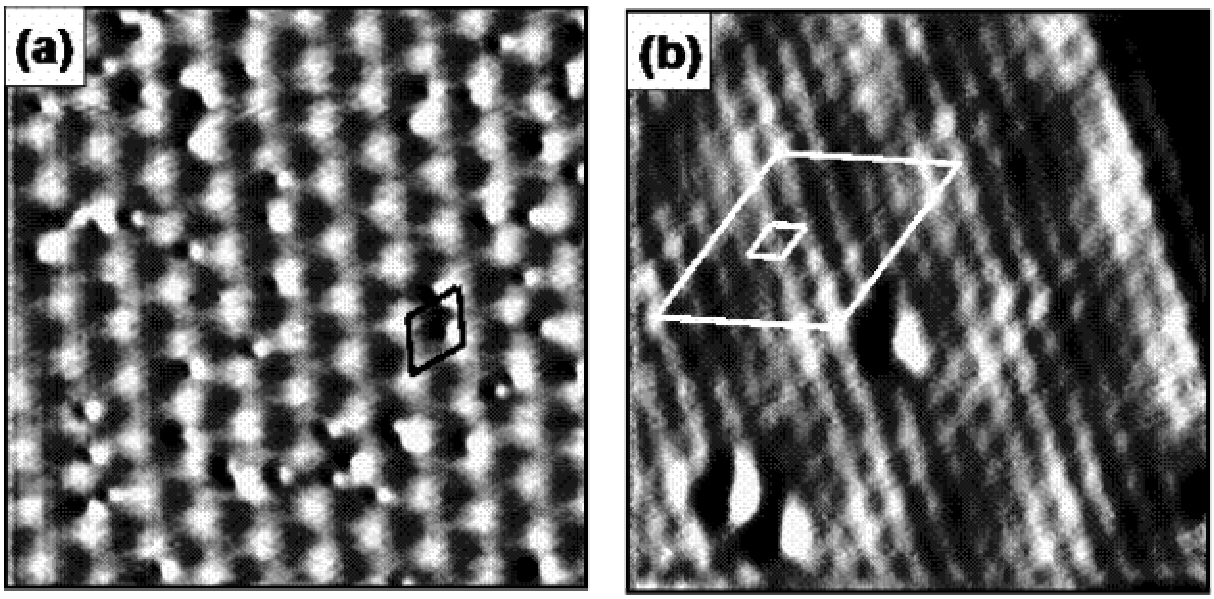

Figure 3: High resolution STM images (I-channel) showing the structure of TiS_2 nanocrystals shown in Figure 1f (0.25 ML Ti deposited at room temperature and annealed up to 800). (a) 21 x 21 nm^2 image showing Moire pattern with a superstructure periodicity of ~ 18 Å ("5 on 6" coincidence lattice); and (b) 7 x 7 nm^2 high resolution image showing both the hexagonal unit cell with a lattice constant of ~3.6 Å and the coincidence lattice. Some defects are observed. The images were obtained at room temperature.

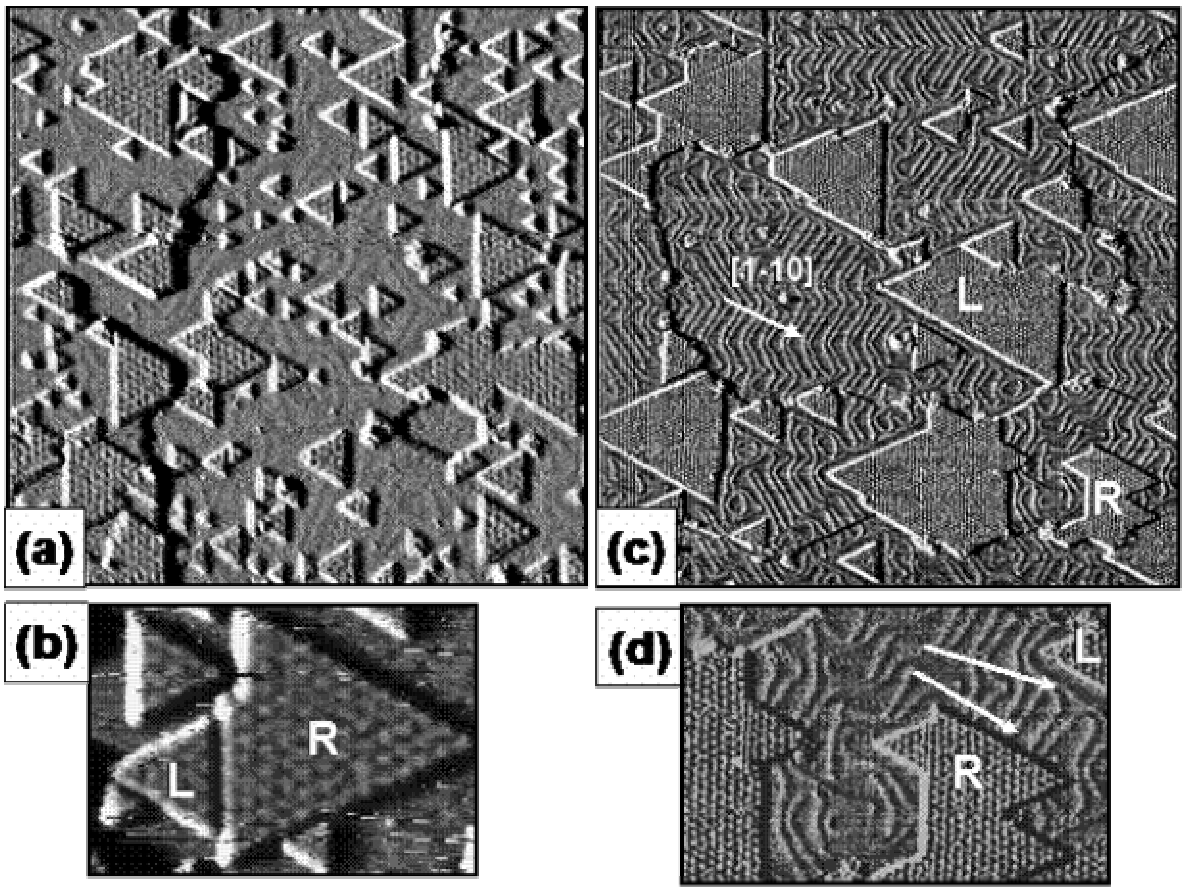

Figure 4: STM images (I-channel) illustrating changes in the morphology of TiS_2 islands during annealing: (a) TiS_2 islands after annealing at 670 K exhibit a broad size distribution and no preferred orientation; (b) islands with different orientations (L vs. R) do not coalesce; (c) after annealing at 800 K the islands grow in size and develop a preferential orientation (L); (d) the herringbone pattern is affected by the type of interface environment at the Au-TiS_2 interface: the dislocation lines run along the edges of L-islands and perpendicular to he edges of R-islands, as indicated by arrows. The images were obtained at room temperature and correspond to an area of 150 x 150 nm^2 (a) and 260 x 260 nm^2 (c); insets: 42 nm x 29 nm (b) and 94 nm x 60 nm (d)

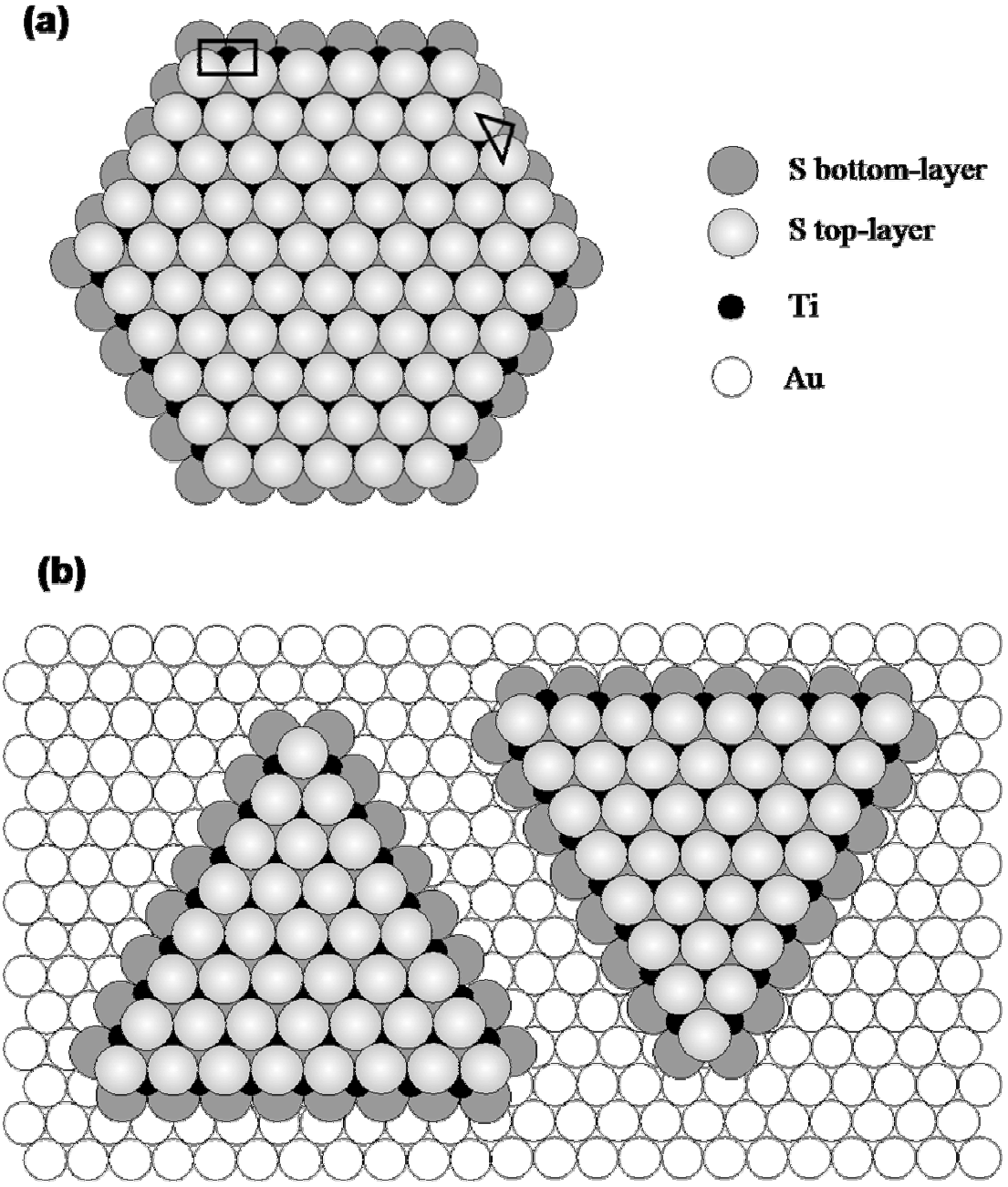

Figure 5: (a) Schematic ball model of a hypothetic hexagonal S-Ti-S island illustrating the existence of two different edge terminations: the (10-10) edge, as indicated by a triangle, and the (-1010) edge as indicated by a rectangle. Triangular islands develop if one edge termination is favored over the other (e.g. the (-1010) for the triangular islands shown in b); (b) a stacking fault within the S layers leads to two island orientations which are rotated by 60 degrees with respect to each other. They exhibit a different edge environment at the Au-S interface which makes them energetically different.

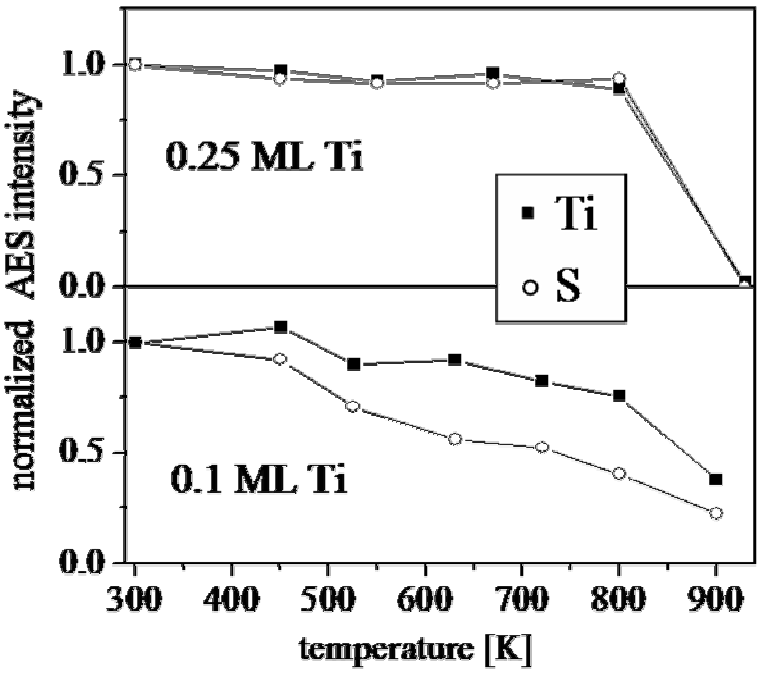

Figure 6: Ti_{418}/Au_{239} and S_{150}/Au_{239} AES peak ratios versus annealing temperature as a function of the initial Ti coverage. The initial sulphur coverage in each case is 0.5 ML. Top: 0.25 ML Ti (stoichiometric ratio); bottom: 0.1 ML Ti (sulphur-rich condition).

IV

Submitted to: Phys Rev B, June 2, 2004
Revised, September 8, 2004

Surface alloying of immiscible metals: Mo on Au(111) studied by STM

Monika M. Biener[1,2], Juergen Biener[3,4], Richard Schalek[3], and Cynthia M. Friend[1,2,†]
[1]Department of Chemistry and
[2]Division of Engineering and Applied Sciences and
[3]Center for Imaging and Mesoscale Structures
Harvard University
12 Oxford Street, Cambridge, Massachusetts 02138 USA
[4] present address: Nanoscale Synthesis and Characterization Laboratory
Lawrence Livermore National Laboratory
7000 East Ave, Livermore, California 94550 USA
[†]Author to whom correspondence should be sent

Abstract

Alloy formation and growth of regular arrays of Mo nanostructures were discovered during studies of Mo growth on Au(111) surfaces. The behavior of Mo deposited via physical vapor deposition was studied as a function of temperature using scanning tunneling microscopy (STM) and Auger electron spectroscopy (AES). Between 300 K and 450 K, regular arrays of Mo clusters form by preferential nucleation of Mo at elbow sites of the herringbone reconstruction. The Mo clusters are 1 or 2 ML high, and are stable upon annealing up to at least 600 K. For deposition temperatures at or above 525 K, substitutional surface alloying competes with nucleation on terrace sites. The formation of a surface alloy is inferred from the evolution of a serrated step-edge morphology caused by attachment of ejected Au atoms, and a decrease of the Mo surface coverage, as well as the appearance of vacancy islands in the Au surface after chemically-driven dealloying of Mo. The formation of a Mo-Au surface alloy is quite remarkable as Mo and Au are bulk immiscible. Even surface alloying would not be expected from the viewpoint of stress relaxation.

I. INTRODUCTION

Recently, the formation of two-dimensional surface alloys has attracted considerable interest due to the technological relevance in various fields such as heterogeneous catalysis, corrosion, surface hardening, and bonding.[1-21] Surface alloying is a promising means to modify the characteristics of a surface and, thus, to design surfaces with unique electronic, catalytic and mechanical properties. The formation of surface alloys is not limited to metal combinations which are miscible in the bulk, but is also observed for a variety of immiscible metal combinations, such as noble metals (Cu, Ag, Au) on refractory metals (Mo, W) and vice versa.[1, 3, 4, 7, 10, 11, 15]

Although bulk alloying is well understood, the driving forces for the formation of surface alloys are still a matter of investigation, in particular in the case of immiscible systems. Various models have been proposed in the literature. For example, Tersoff [5] attributed the formation of surface alloys between immiscible elements with an atomic size mismatch, such as Au on Ni, to a reduced strain energy of the misfitting atoms at the surface relative to the bulk. In case of the Cu/W(100) system, the formation of a substitutional surface alloy has been explained in terms of a c(2x2)/W(100) vacancy structure, stabilized by Cu.[4] More recently, first principles calculations revealed that surface alloying of noble metals (Cu, Ag, Au) with W(001) and Mo(001) surfaces is caused by the difference in electronegativity.[7]

Recently, we investigated the deposition of Mo on Au(111) from a $Mo(CO)_6$ precursor. The chemical vapor deposition (CVD) approach leads to preferential nucleation of Mo clusters at step edges. Although Mo/Au is a bulk immiscible system, there is evidence for alloying/intermixing based on the observation of holes that develop in the Au substrate after Mo deposition.[22, 23] Further evidence for the intermixing of Mo and Au is that the deposited Mo clusters exhibit a reduced reactivity towards dissociation of O_2 or CO compared to bulk Mo.[1] The results discussed above are also consistent with recent DFT calculations which predict that Mo on Au(111) prefers to be embedded in the Au surface rather than being adsorbed on the surface.[1, 24] However, Mo-Au intermixing should further increase the tensile stress of the Au(111) surface (atomic size mismatch of ~5%) and therefore make surface alloying unfavourable.[5, 25]

The combination of its inertness and its regular dislocation pattern (known as herringbone reconstruction) makes the Au(111) surface an ideal template for self-organized growth of nanostructures. The reconstruction mechanism has been described in more detail elsewhere.[26, 27] Briefly, the Au(111) surface is uniaxially contracted (4.2%) along the close-packed [1-10] directions leading to fcc and hcp stacking regions that are separated by dislocation lines. In addition, a regular alternation of uniaxially contracted domains allows a more isotropic contraction of the surface layer. This leads to the well known zig-zag (chevron or herringbone) pattern, where the bending points (elbows) form a periodic network of dislocations. Indeed, previous studies of the physical vapor deposition (PVD) of Fe[28], Co[29], Mo[30] and Ni[31] on the Au(111) herringbone have demonstrated that preferential nucleation of these metals occurs at the elbows.

In the present paper, we describe the formation of a substitutional Mo-Au surface alloy via PVD of Mo on Au(111) as a function of the deposition temperature. The Mo induced changes of the surface morphology and surface composition are characterized by scanning tunneling microscopy (STM) and Auger electron spectroscopy (AES). Our results shed new light on the reduced reactivity of Mo clusters on Au(111) surfaces.

II. EXPERIMENTAL

All experiments were performed in a commercial ultrahigh vacuum (UHV) system with a base pressure of $5x10^{-11}$ mbar. The system has separate compartments for sample preparation, e.g. Mo evaporation, and sample characterization. The latter is equipped with commercial instrumentation for scanning probe microscopy (SPM) (Omicron), Auger electron spectroscopy (AES) and low energy electron diffraction (LEED). The Au(111) sample was cleaned by cycles of Ar^+ sputtering at room temperature (60 min / 1000 eV / 4 μA) and annealing (10 min at 900 K followed by one hour at 700 K). This procedure was repeated until no contaminants were detected by means of AES. The sample was radiatively heated, and the temperature was calibrated using a Cr-Al thermocouple attached to the sample holder.

Molybdenum (Goodfellow, 99.9%) was evaporated from rod material (1.5 mm diameter) using an electron beam evaporator (Omicron) (900 V / ~ 65 mA). The deposition rate was monitored continuously by a flux monitor measuring the ion flux, which is proportional to the flux of evaporated atoms. Initially the deposition rate was calibrated using

a quartz thickness monitor. All preparations in this publication were performed using a flux of ~0.25 to 0.75 ML Mo min^{-1}. The results turned out to be independent from the flux in the used range (this is consistent with the rate dependence of the two competing mechanisms with respect to the deposition rate: surface alloying and cluster nucleation at elbow sites, are both first order with respect to the concentration of free Mo atoms as the rate limiting step is a place exchange in both cases). Using the flux monitor to determine the exposure, a specific coverage could be achieved with a reproducibility of ± 10 %. Nitrogen dioxide (Matheson, 99.5 %) was used for oxidation-induced dealloying. The purity of NO_2 was periodically checked with a residual gas analyzer.

STM images were collected at room temperature and Z-channel and I-channel images were obtained simultaneously. Etched $Pt_{0.8}$ $Ir_{0.2}$ tips from Molecular Imaging were used for imaging.

The surface Mo coverage was estimated by STM. Complementary, AES was used to determine the total Mo coverage (surface and subsurface species). However, quantitative evaluation of Auger electron spectra strongly depends on a detailed knowledge of the depth distribution of Mo due to the finite escape depth of AES electrons (~5 Å). To avoid the ambiguities associated with the unknown depth distribution of Mo in our experiment, we utilize the fact that Mo can be de-alloyed by NO_2 induced oxidation;[22] the resulting single layer MoO_3 islands, which nucleate *on top* of the Au(111) surface, are used to asses the total Mo coverage by means of AES. Using this approach we are able to estimate both the surface and subsurface Mo coverage.

III. RESULTS AND DISCUSSIONS

Well-ordered arrays of Mo nanoclusters form on the reconstructed Au(111) surface using PVD to deposit Mo at room temperature (Fig. 1), in agreement with previous work.[30] The elbow sites of the herringbone reconstruction of the Au(111) surface serve as selective nucleation sites. The step edges are also decorated by small clusters, while retaining relatively straight shapes. The height profile (Fig. 1, bottom) along the indicated line demonstrates that the apparent height of the Mo clusters is either ~ 2.5 Å or 5 Å,

corresponding to monolayer or double layer features, respectively. Approximately one third of the total Mo coverage is found in the second layer. The diameter of the clusters is in the range of 3-5 nm.

The preferential nucleation of metals at the elbow sites of the reconstructed Au(111) surface is a common phenomenon and was previously observed for Fe[28], Co[29] and Ni[31]. It has been suggested that the nucleation is initiated via a site selective place exchange by impinging metal atoms at the elbows sites of the herringbone reconstruction,[32] i.e. the formation of a local surface alloy. The elbow sites are expected to be the most reactive sites for place exchange due to the under-coordinated nature of gold atoms at these sites. This place exchange mechanism should be active for all metals which exhibit higher values of surface free energy and heat of evaporation compared to those of Au. Since Mo has a surface free energy of 2.88 Jm^{-2} (surface free energy of Au = 1.62 Jm^{-2})[33] and a heat of evaporation of 6153 J/g (heat of evaporation of Au = 1738 J/g) a selective nucleation of Mo on the elbow sites via place exchange can be expected.

The decoration of the elbow sites by Mo clusters is accompanied by a modification of the characteristic herringbone pattern towards a more triangular dislocation structure (Fig. 1b inset). Similar changes of the herringbone pattern have been reported for adsorption of K and Na on Au(111) and have been explained by an adatom-induced weakening of the interaction between the first two Au layers. This causes a further increase of the atomic density of the topmost layer as evidenced by the higher density of dislocation lines.[34, 35]

Changes in the morphology of the surface, indicative of dissolution of Mo into the Au, are observed when Mo is deposited at 450 K (Fig. 2). Specifically, the number density of Mo clusters at step edges decreases while the average cluster size remains essentially the same. In addition, some holes (irregularities) in the step edges are also observed (Fig. 2 inset). These observations are consistent with the formation of a Mo-Au alloy. The denuding of the step edges of Mo suggests that Mo dissolves into Au at the step, while the appearance of holes in the Au step edge suggests the incorporation of Au into Mo nanoclusters. Alternatively, the holes could be caused by entropy-driven bulk vacancy formation during annealing. Upon subsequent cooling these vacancies would then be filled again by Au atoms from the step edges resulting in a retreating step edge. Mo clusters might cause a pinning of the step edges, possibly leading to the observed holes.[36] However, we also image these holes

at 420 K after Mo deposition via CVD at 420 K. Thus, we believe that the holes are an indication for surface alloying, specifically in view of the observations discussed below.

More dramatic changes in the surface morphology that are indicative of alloy formation are observed when Mo is deposited at or above 525 K (Fig. 3). The step edges of the gold surface are highly irregular. Furthermore, the Mo surface coverage as determined by STM decreases by more than 50 % using the same nominal Mo exposure, as discussed in more detail below. Finally, no two-layer high Mo clusters are found when Mo is deposited above 525 K, even though the diameters of Mo clusters remain unchanged.

The formation of a serrated step edge shape upon metal deposition has previously been reported for other metal-metal systems, for example Pd on Cu or Ag, and Au on Ag, and is generally explained by substitutional surface alloying where the ejected substrate metal atoms diffuse to nearby step edges.[16, 18-20] In some systems the expelled substrate atoms also nucleate on terrace sites and form new substrate islands, e.g. Ni, Rh and Pt on Au, and Au on Ni and Cu,[2, 8, 13, 16, 17]

Following this interpretation, we attribute our observation of a serrated step edge morphology (see Fig. 3) to the formation of a substitutional Mo-Au surface alloy. The Au atoms released by place exchange during alloying attach themselves to step edges (nucleation of Au islands on terraces was not observed), leading to step flow growth of existing terraces. The position of the original straight step edges (before deposition) can occasionally be pinpointed by vacancy line defects, as demonstrated by the example shown in Fig. 3a. For better visualization, a magnification of the structure in the vicinity of a vacancy line defect is shown in Fig. 3b. The serrated shape of the step edges after Mo deposition indicates a diffusion-limited aggregation (DLA) process with some local relaxation.[37] Even at 525 K, the diffusion along the step edges seems to be too slow to allow for complete relaxation towards straight step edges typical for well-annealed Au(111) surfaces. This might indicate that the step edge diffusion barrier increases by the formation of the Au-Mo surface alloy. Similar behavior has been observed for Ag-Co on Ru(0001).[38]

The stability of the herringbone pattern during surface alloying is surprising as one would expect a further contraction of the herringbone pattern due to the atomic size mismatch of Mo and Au. However, a similar observation was reported for the Pt/Au(111) system where

Pt-Au place exchange did not perturb the reconstruction pattern.[2] A possible explanation for this behavior would be the pinning of the dislocation pattern by Mo clusters.

The newly developing terrace areas exhibit a characteristic, highly disordered dislocation pattern (Fig. 3c, Fig. 3e), in contrast to the regular herringbone pattern observed on the original terrace areas (Fig. 3c, Fig. 3d). Although the herringbone reconstruction is thermodynamically the most stable form of the Au(111) surface, there is an activation barrier that prevents spontaneous reconstruction at 300 K. Thus the Au atoms within the newly developing, disordered terrace areas might still be trapped in a meta-stable state, even at 525 K. Alternatively, the relaxation towards a regular reconstruction pattern could be hindered by incorporated molybdenum pinning sites. It should be emphasized that the observation of a dislocation pattern characteristic of gold, even though disordered, further corroborates the interpretation that the step edges grow by attachment of expelled Au atoms, rather than by attachment of diffusing Mo atoms.

The observation of Mo clusters on the newly developing terrace areas proves that these surface areas were formed *during* Mo deposition. The local cluster density on newly developing terrace areas can be used to track the time-dependent evolution of the step morphology during Mo deposition: areas, which developed late during the deposition process, exhibit a low cluster density, and vice versa.

The degree of surface alloy formation increases with increasing deposition temperature as evidenced by the decreasing fraction of the deposited Mo found in Mo clusters. The surface morphology after Mo deposition at 600 K (Fig. 4) is similar to that observed after deposition at 525 K (Fig. 3); however, the number density of Mo nanostructures is lower for the deposition temperature of 600 K. An apparent Mo surface coverage of only 0.1 ML was determined by STM (Fig. 4) after a nominal exposure of 0.3 ML at 600 K. As the Mo/Au AES peak ratio decreases only by 20% compared to AES data obtained after deposition at room temperature the majority of the alloyed molybdenum seems to be confined near the surface. Substitutional Mo is expected to be trapped at defect sites such as the herringbone dislocation lines. Indeed, small protrusions on the herringbone dislocation lines can be observed in the STM image displayed in Fig. 4. Similar features were reported for Rh on Au(111), and were attributed to the structural and electronic relaxation of Au atoms surrounding groups of one or several Rh atoms which are incorporated in the

surface.[13] However, our STM resolution is insufficient to determine the atomic structure of these features.

The observation of vacancy islands on the Au surface after oxidation provides supporting evidence for the formation of a Mo-Au surface alloy (Fig. 5). As reported earlier, Mo clusters on Au(111) can be oxidized towards single layer MoO_3 islands by NO_2 exposure.[22, 39] Similarly, oxidation of a Mo-Au surface alloy by NO_2 exposure leads to MoO_3 formation and generation of vacancies. The latter diffuse and aggregate into vacancy islands. These vacancy islands either annihilate at step edges, or are stabilized by nucleation of MoO_3 islands (Fig. 6). Figure 7 shows a STM image of a vacancy island stabilized by MoO_3 which was observed after deposition of 0.3 ML Mo and subsequent oxidation by a 20 L NO_2 exposure at 525 K: MoO_3 island "A" is *on* the Au terrace, whereas island "C" is *in* the vacancy island "B". As shown in the line scan, the heights of the MoO_3 island located *in* an Au vacancy island (C) and the MoO_3 island *on* the Au terrace (A) are identical with respect to the underlying Au surface. The fact that Mo segregates to the surface during NO_2 exposure as evidenced by the observation of vacancy islands confirms that the alloyed molybdenum is confined in a shallow surface area. As a consequence, the oxygen-driven de-alloying can be employed to assess the total Mo coverage (see section "experimental").

As discussed above, the Mo surface coverage detected by STM decreases with increasing deposition temperature, consistent with the formation of a Mo-Au surface alloy. The variation of the Mo surface coverage, as determined by STM, versus deposition temperature is summarized in Fig. 5 (open symbols). A fluence of 0.3 ML was used for all preparations. In the temperature range from 450 K to 600 K, the Mo surface coverage as determined by STM decreases by approx. 65%. This decrease is *not* caused by a decreasing sticking coefficient of Mo with increasing deposition temperature, as the Mo deficit can be detected by STM and AES *after* oxidation-driven de-alloying (see Fig. 5, filled symbols).

The formation of a Mo-Au surface alloy is an activated process as demonstrated by the dependence of the Mo surface coverage on the deposition temperature. A similar temperature dependence was reported for Rh on Au(111)[13]and Ag on Cu(100)[3]. However, once Mo clusters are formed via deposition at room temperature, they are resistant to alloying up to at least 600 K: The morphology of the Mo-covered Au sample shown in Fig. 1 does not change after annealing at 600 K for 10 minutes (not shown) and the Mo_{187}/Au_{239} AES peak

ratio decreases by only 10 %, indicating a negligible place exchange between Mo and Au. This suggests that the Mo-Mo interactions are strong enough to suppress the formation of an alloy, even at 600 K. Only individual Mo atoms impinging on the surface at or above 525 K can surmount the activation barrier for surface alloying. Furthermore the thermal stability of Mo clusters prepared at room temperature excludes that the decreasing Mo surface coverage with increasing deposition temperature is caused by a simple sinking of the clusters into the substrate.

As previously reported, only some intermixing was observed during CVD of Mo at 450 K or 500 K using $Mo(CO)_6$ as a precursor.[22] In the case of CVD, the decomposition of the precursor species is auto-catalyzed by Mo deposited via thermal decomposition, and the Mo atoms released are immediately stabilized by formation of Mo-Mo bonds and thus no longer available for surface alloying. The formation of etch holes at Au step edges between neighboring Mo clusters was observed, similar to the results after PVD of Mo at 450 K described above (fig. 2), indicating the incorporation of Au atoms into Mo clusters. The surface alloying observed in the present study further supports Mo-Au intermixing and thus allows to rationalize the reduced reactivity of Mo nanoclusters on Au(111) surfaces.

Surface alloying of Mo on Au(111) is remarkable as the two elements are bulk immiscible. Our experimental results are in agreement with recent DFT calculations which suggest that intermixing or site exchange at the Mo/Au(111) interface is energetically more stable than Mo bound *on* the Au(111) surface.[1, 24] Furthermore, surface phase diagrams constructed from calculated surface energies reveal a positive surface segregation energy (Mo should dissolve in the substrate) and a positive surface alloy mixing energy (phase separation).[40, 41] Another approach to explaining surface alloying of bulk immiscible elements is purely based on strain energies.[5, 25] However, according to this approach Mo-Au intermixing should further increase the intrinsic tensile stress of the Au(111) surface as Mo atoms are ~ 5% smaller than Au atoms. Thus, surface alloying should be unfavorable due to atomic size mismatch. This is consistent with the fact that we do not observe a segregation of an alloy phase and the reconstructed surface, as reported for other systems.[25] Segregation can be expected if the intrinsic tensile surface stress can be reduced by two competing mechanisms: surface alloying and surface reconstruction. As Mo-Au intermixing further *increases* the tensile stress, phase segregation is not favorable.

From the viewpoint of thermodynamics the formation of a Mo-Au surface alloy might be driven by the supersaturation of Mo atoms on the surface *during* Mo deposition. The supersaturation is equivalent to an increased chemical potential of Mo which might drive surface alloying despite increasing the surface stress. In case of the present system surface alloying is probably facilitated by the reconstruction of the Au(111) surface due to the existence of undercoordinated Au atoms.

IV. CONCLUSIONS

The formation of a substitutional surface alloy was observed after deposition of Mo on Au(111) at temperatures between 525 K and 600 K. The observation of the ejected Au, which agglomerates at step edges and the formation of Au vacancy islands upon oxidation of Mo are evidence for alloy formation. Furthermore the Mo surface coverage as determined by STM significantly drops with respect to the total coverage. Surface alloying is an activated process, and is only observed for deposition temperatures at or above 525 K. However, once Mo clusters are formed the Mo-Mo bond is strong enough to prevent alloy formation even at 600 K. Our results are consistent with recent theoretical work on Mo/Au(111),[1, 24, 40, 41] but contrary to a stress relaxation model.[5, 25]

ACKNOWLEDGEMENTS

We gratefully acknowledge the support of this work by the US Department of Energy, Basic Energy Science, under grant number DE-FG02-84ER13289 and by the Harvard University NSEC, funded by the National Science Foundation, grant no. PHY-01-17795. J.B. acknowledges current support under the auspices of the U. S. Department of Energy by the University of California, Lawrence Livermore National Laboratory, under Contract No. W-7405-Eng-48.

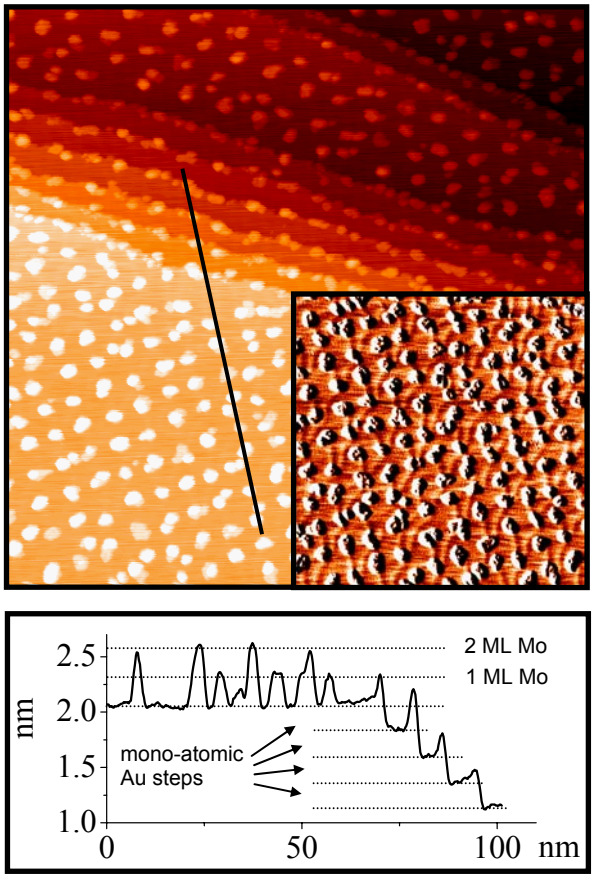

FIG. 1:
STM image (Z-channel) showing Mo clusters on Au(111) after deposition of 0.3 ML of Mo at room temperature. The clusters nucleate predominantly on the terrace at the elbows of the herringbone reconstruction and are one or two monolayers high (see line scan along the indicated line). The inset illustrates the modification of the herringbone pattern towards a more triangular structure. The image was obtained at room temperature and corresponds to an area of 150 nm x 150 nm (inset 85 nm x 85 nm).

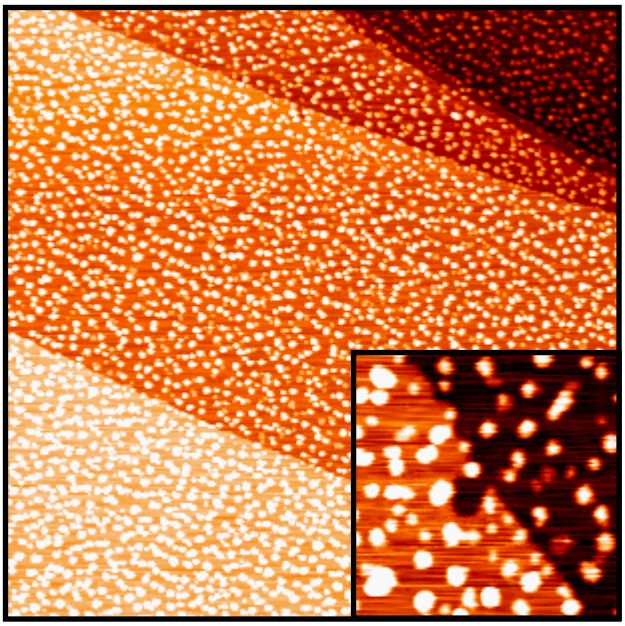

FIG. 2:

STM image (Z-channel) showing Mo clusters on Au(111) after deposition of 0.3 ML of Mo at a substrate temperature of 450 K. Substrate step edges are straight; occasionally etch holes were observed (see inset) The image was obtained at room temperature and corresponds to an area of 380 nm x 380 nm (inset 50 nm x 50 nm)

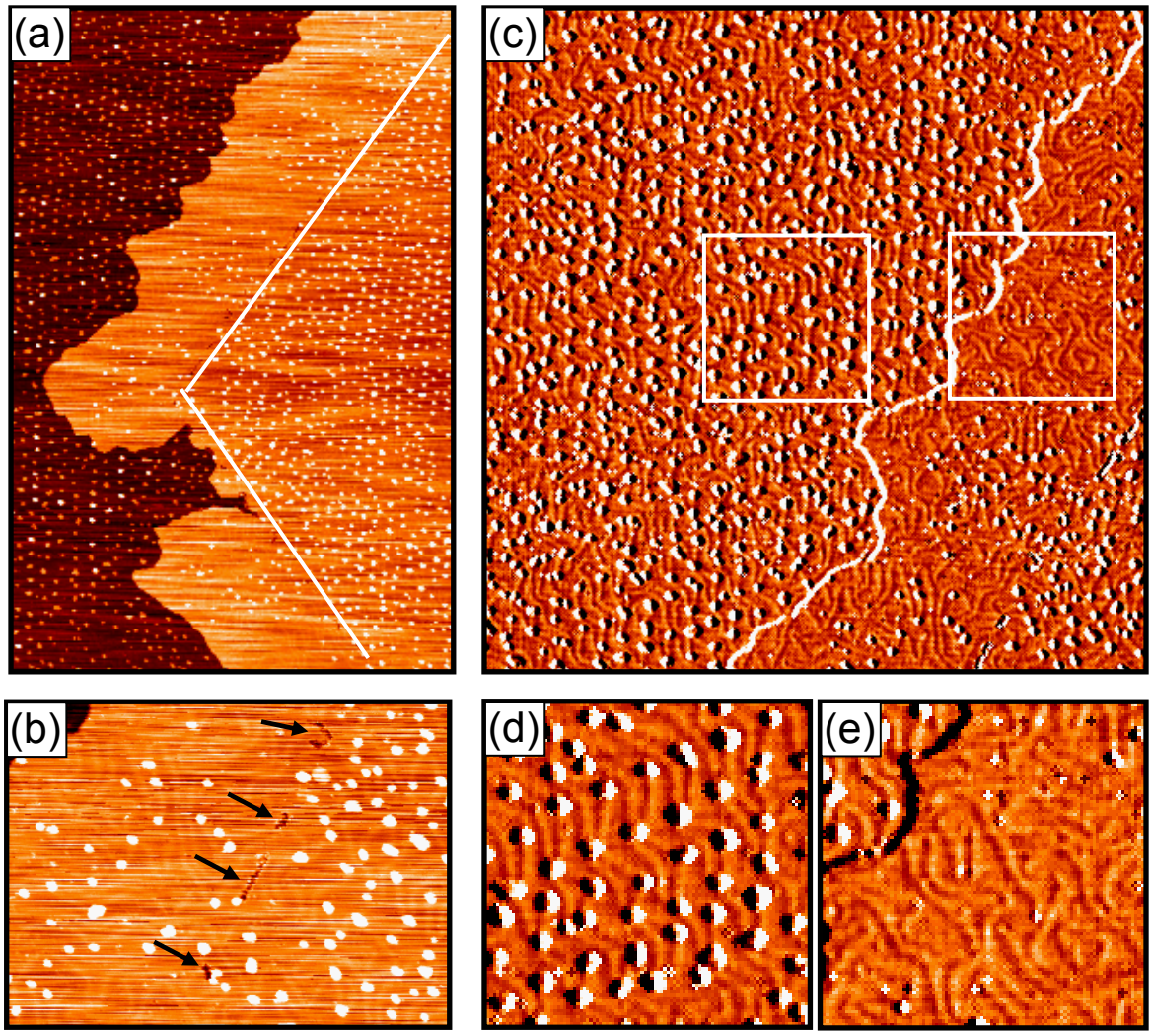

FIG. 3:
STM images showing changes in morphology after deposition of 0.3 ML Mo at 525 K. (a): Z-channel image, illustrating the serrated step edge morphology; the straight lines serve as visual guide for the vacancy line defects which mark the position of the original step edge. (b): close-up of the same area, arrows indicate the position of the line defect. (c): I-channel image, illustrating the distortion of the herringbone pattern on newly developing terrace areas with a close-up (e), in contrast to original terrace areas which exhibit a well ordered herringbone pattern (d). The images were obtained at room temperature and correspond to an area of (a): 420 nm x 280 nm, (b): 110 nm x 80 nm, (c): 250 nm x 250 nm, (d) and (e): 65 nm x 65 nm

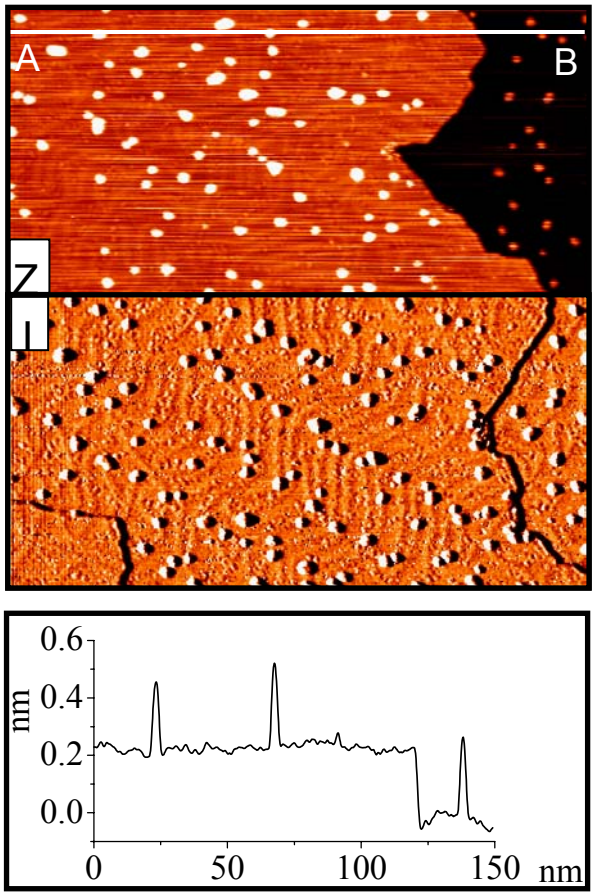

FIG. 4:

STM image (top: Z-channel, middle: I-channel) showing Mo clusters on Au(111) after deposition of 0.3 ML Mo at 600 K. The image corresponds to an area of 150 nm x 150 nm. A height profile from A to B is shown in the bottom. Small defects in the herringbone structure can be identified in the I-channel.

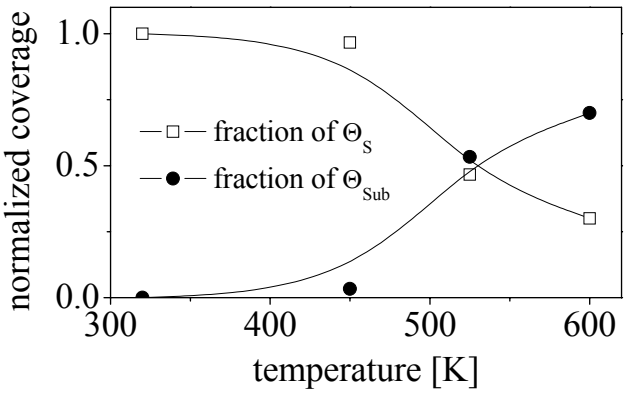

FIG. 5:

Mo surface coverage (open symbols) on Au(111), as determined by STM, and Mo subsurface fraction (filled symbols) for different deposition temperatures. The decrease in Mo surface coverage with increasing deposition temperature is *not* caused by a decreasing sticking coefficient of Mo, as the Mo deficit can be detected by STM and AES after oxidation-driven de-alloying. The lines serve only as optical guide to emphasize the observed trend.

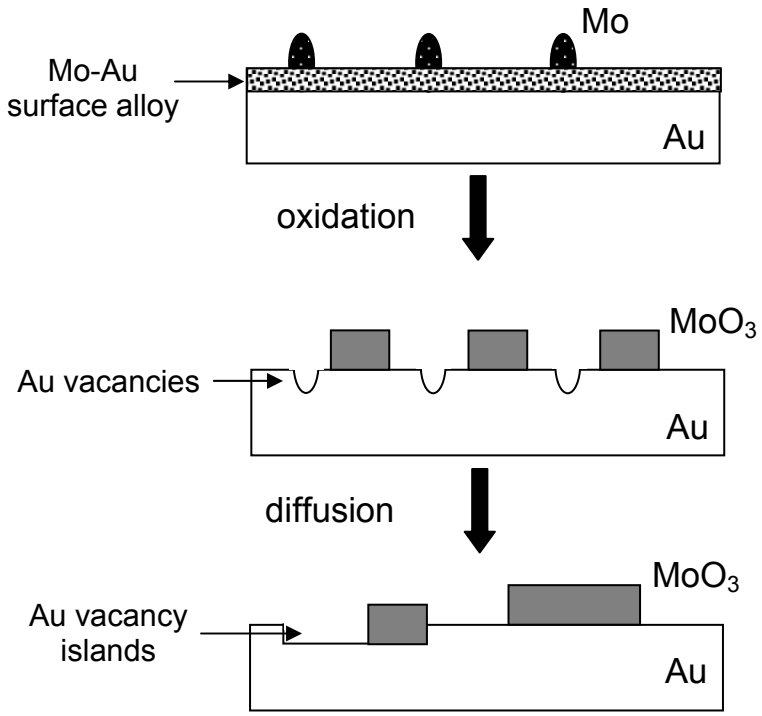

FIG. 6:

Schematic of de-alloying of Mo on Au(111) and the formation of associated vacancy islands driven by oxidation. The Mo-Au surface alloy (a) can be oxidized to MoO_3 and thereby generated vacancies (b) can diffuse and aggregate into vacancy islands. These vacancy islands either annihilate at step edges, or are stabilized by nucleation of MoO_3 islands (c).

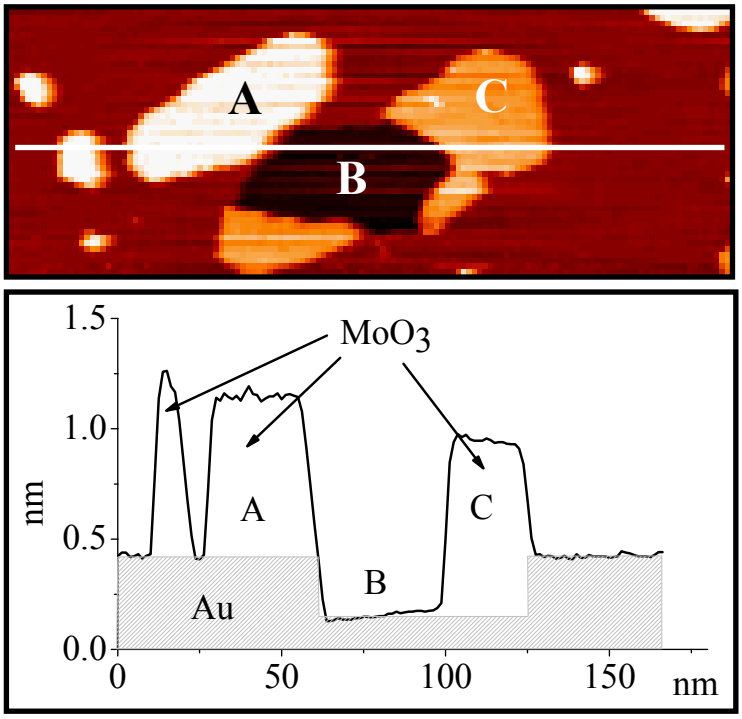

FIG. 7:

STM image (Z-channel) showing a vacancy island stabilized by MoO_3, after deposition of 0.3 ML Mo on Au(111) at 525 K and subsequent oxidation by exposure to NO_2. Island "A" is *on* the Au terrace, whereas island "C" is *in* the vacancy island "B". A height profile along the indicated line shows that island A and island C exhibit identical height with respect to the underlying Au. The image was obtained at room temperature and corresponds to an area of 180 nm x 60 nm.

References

[1] P. Liu, J. A. Rodriguez, J. T. Muckermann, et al., Phys. Rev. B **67**, 155416 (2003).

[2] M. O. Pedersen, S. Helveg, A. Ruban, et al., Surf. Sci. **426**, 395 (1999).

[3] P. T. Sprunger, E. Laegsgaard, and F. Besenbacher, Phys. Rev. B-Condensed Matter **54**, 8163 (1996).

[4] P. Hu, A. Wander, L. Morales de a Garza, et al., Surf. Sci. Lett. **286**, L542 (1993).

[5] J. Tersoff, Phys. Rev. B **74**, 434 (1995).

[6] G. Bozzolo, R. Ibanezmeier, and J. Ferrante, Phys. Rev. B **51**, 7207 (1995).

[7] X. K. Shu, P. Jiang, and J. G. Che, Surf. Sci. **545**, 199 (2003).

[8] W. G. Cullen and P. N. First, Surf. Sci. **420**, 53 (1999).

[9] Y.-R. Tzeng, H. Wu, K.-D. Shiang, et al., Phys. Rev. B **48**, 5549 (1993).

[10] G. A. Attard and D. A. King, Surf. Sci **188**, 589 (1987).

[11] H. Takahashi, M. Sasaki, S. Suzuki, et al., Surf. Sci. **304**, 65 (1993).

[12] D. O. Boerma, G. Dorenbos, G. H. Wheatley, et al., Surf. Sci. **307-309**, 674 (1993).

[13] E. I. Altman and R. J. Colton, Surf. Sci. Lett. **304**, L400 (1993).

[14] J. de la Figuera, J. E. Prieto, C. Ocal, et al., Surf. Sci. **307-309**, 538 (1993).

[15] S. H. Overbury and D. R. Mullins, J. Vac. Sci. Technol. A **7**, 1942 (1989).

[16] D. Chambliss, J. Wilson, and S. Chiang, J. Vac. Sci. Technol. A **10**, 1993 (1992).

[17] L. P. Nielsen, F. Besenbacher, I. Stensgaard, et al., Phys. Rev. B **71**, 754 (1993).

[18] P. W. Murray, S. Thorshaug, I. Stensgaard, et al., Phys. Rev. B-Condensed Matter **55**, 1380 (1997).

[19] E. S. Hirschorn, D. S. Lin, E. D. Hansen, et al., Surf. Sci. **323**, L 299 (1995).

[20] P. W. Murray, I. Stensgaard, E. Laegsgaard, et al., Phys. Rev. B-Condensed Matter **52**, 14404 (1995).

[21] L. P. Nielsen, I. Stensgaard, F. Besenbacher, et al., surface review and letters **3**, 1713 (1994).

[22] M. M. Biener, J. Biener, R. Schalek, et al., J. Chem. Phys. (submitted).

[23] Song Z., Cai T. H., J. A. Rodriguez, et al., J. Phys. Chem. **107**, 1036 (2003).

[24] P. Liu, J. A. Rodriguez, J. T. Muckermann, et al., Surf. Sci. Lett. **530**, L313 (2003).

[25] M. Batzill and B. E. Koel, Eurohys. Lett. **64**, 70 (2003).

[26] C. Woell, R. J. Chiang, J. Wilson, et al., Phys. Rev. B **39**, 7988 (1989).

[27] J. V. Barth, H. Brune, G. Ertl, et al., Phys. Rev. B **42**, 9307 (1990).

[28] J. A. Stroscio, D. T. Pierce, R. A. Dragoset, et al., J. Vac. Sci. Technol. A **10**, 1981 (1992).

[29] B. Voigtlaender, G. Meyer, and N. Amer, Phys. Rev. B **44**, 10354 (1991).

[30] S. Helveg, J. V. Lauritsen, E. Laegsgaard, et al., Phys. Rev. Lett. **84**, 951 (2000).

[31] D. Chambliss, R. Wilson, and S. Chiang, Phys. Rev. Let. **66**, 1721 (1991).

[32] J. A. Meyer, I. D. Baikie, E. Kopatzki, et al., Surf. Sci. **365**, L647 (1996).

[33] L. Z. Mezey and J. Giber, Jap. J. Appl. Phys. **21**, 1569 (1982).

[34] J. V. Barth, R. J. Behm, and G. Ertl, Surf. Sci. Lett. **302**, L319 (1993).

[35] J. V. Barth, R. J. Behm, and G. Ertl, Surf. Sci. **341**, 62 (1995).

[36] B. Poelsema, J. B. Hannon, N. C. Bartelt, et al., Appl. Phys. Lett. **84**, 2551 (2004).

[37] A.-L. Barabasi and H. E. Stanley, *Fractal concepts in surface growth* (Cambridge University Press, Cambridge, 1995).

[38] R. Q. Hwang, Phys. Rev. Lett. **76**, 4757 (1996).

[39] M. M. Biener and C. M. Friend, Surf. Sci. Lett. **559**, L173 (2004).

[40] A. V. Ruban, H. L. Skriver, and J. K. Norskov, Chemical Physics Of Solid Surfaces **10**, 1 (2002).

[41] A. Christensen, A. V. Ruban, P. Stoltze, et al., Phys. Rev. B-Condensed Matter **56**, 5822 (1997).

V

Submitted to Langmuir
October 22, 2004

Revisiting the S-Au(111) interaction: Static or dynamic?

Monika M. Biener[1,2], Juergen Biener[3,4], and Cynthia M. Friend[1,2,*]
[1]Department of Chemistry and
[2]Division of Engineering and Applied Sciences and
[3]Center for Imaging and Mesoscale Structures
Harvard University
12 Oxford Street, Cambridge, Massachusetts 02138 USA
[4]Current address: Nanoscale Synthesis and Characterization Laboratory
Lawrence Livermore National Laboratory
7000 East Ave, Livermore, California 94550 USA

[*]corresponding author

The Au-S interaction is probably the most intensively studied interaction of Au surfaces with non-metals as, for example, it plays an important role in Au ore formation [1], and controls the structure and dynamics of thiol-based self-assembled-monolayers (SAMs) [2-4]. Various S-induced surface structures on Au(111) were recently reported for different conditions and predominantly interpreted in terms of a static Au surface. Here we demonstrate that the Au(111) surface exhibits a very dynamic character upon interaction with adsorbed sulfur: large-scale surface restructuring and incorporation of Au atoms into a growing 2D AuS phase were in-situ observed. These results provide new insight into the Au-S surface chemistry.

Gold is considered to be the most noble of all metals. Traditionally gold is widely used in jewellery, however, due to its unique blend of properties gold also becomes an increasingly important material in industrial applications. For example, the high electronic conductivity in combination with corrosion resistance makes gold-plated contacts an essential part in microelectronics. Due to its chemical inertness gold is also an attractive substrate for surface science studies, for instance gold films are widely used as substrate for alkanethiol-based self-assembled monolayers (SAMs) [2-4]. However, the chemical inertness typically observed for Au does not imply a general inability to form stable bonds with non-metals but is rather a consequence of high reaction barriers [5]. Gold can, for example, exhibit very interesting catalytic properties if dispersed, and indeed gold-based catalysts are being developed for industrial oxidation processes [6, 7].

In the present work we focus on the dynamics of the Au surface as affected by the Au-S interaction, which is one of the most relevant Au-non-metal interactions.
Real-time scanning tunnelling microscopy (STM) was employed to directly monitor mass-transport involved in Au-S surface interaction. Specifically, we address the nature of the S-induced rectangular surface features on Au(111), which were observed under a wide variety of experimental conditions [8-12] and predominantly attributed to the formation of S_8 molecules adsorbed on the surface. In contrast, our experiments provide strong evidence that these rectangular structures arise from the formation of a 2D AuS phase which involves a dynamic rearrangement of the surface landscape and large scale mass transport.

All experiments were performed in an ultrahigh vacuum (UHV) system with a base pressure of 4×10^{-10} torr. The system is equipped with a home-made "beetle-type" Scanning Tunneling Microscope (STM) and commercial instrumentation for Auger Electron Spectroscopy (AES) and Low energy Electron Diffraction (LEED). The sample was radiatively heated via a tungsten filament located behind the sample. The temperature was monitored by a chromel/alumel thermocouple affixed to the sample holder. The Au sample was cleaned by cycles of Ar^+ sputtering (1000eV, ~5 μA) at 300 K, followed by annealing to 700 K for 10 minutes and 600 K for 60 minutes. Following this procedure, the characteristic Au(111)-(22x√3) "herringbone" reconstruction was observed by LEED and STM. The Au sample used for these experiments exhibits many surface defects, most likely partial

Shockley dislocations [13] introduced by the gentle annealing procedures used in the present study. SO_2 ("Matheson", anhydyrous grade) served as a source of sulfur, and was introduced by chamber backfilling. Only a small fraction of the admitted SO_2 molecules decomposes on the Au(111) surface and deposits sulfur. The sulfur coverage was monitored by AES and calibrated relative to the S induced ($\sqrt{3}$x$\sqrt{3}$)R30° LEED pattern corresponding to a S coverage of ~0.3 ML. At any point of the experiment, sulfur is the only species on the surface detected by AES. The oxygen released by SO_2 decomposition seems to be removed via an abstraction reaction with excess SO_2 [14]. In order to rule out effects due to electron-induced reactions, the experiments were reproduced with the ion gauge turned off. All STM images shown in this work were collected at room temperature using $Pt_{0.8}$ $Ir_{0.2}$ tips. The STM scanner was calibrated against the unit cell of the Au(111) surface.

The clean Au(111) surface exhibits a characteristic "herringbone" reconstruction pattern that is caused by the presence of tensile surface stress. This tensile stress drives the incorporation of an additional 4% of Au atoms in the surface layer leading to a uniaxial contraction along the close-packed <110> directions [15, 16]. The resulting fcc and hcp stacking regions are separated by rows of bridging Au atoms which appear as ridges in STM images. A regular arrangement of rotational domains of uniaxially contracted areas allows for a more isotropic stress distribution and gives rise to the observation of the characteristic herringbone pattern of the clean Au(111) surface (Fig. 1a).

The surface stress of the clean Au(111) surface is strongly modified by the interaction with adsorbed sulfur atoms, which leads to a relaxation of the surface layer in the low coverage regime, and the formation of a two-dimensional AuS phase at higher coverage. The relaxation of the stress-induced reconstruction of the clean Au(111) surface with increasing sulfur coverage was monitored by real-time STM (Fig. 1). Our experiments reveal that sulfur coverages as low as 0.05 ML significantly modify the reconstruction pattern of the clean surface even at room temperature. The sulphur coverage is determined using Auger electron spectroscopy (AES). According to a simple model proposed by Ibach [17], such an adsorbate-induced modification of the surface stress can qualitatively be explained by charge being transferred from the bonds between the substrate surface atoms to the adsorbate atoms, thereby creating compressive surface stress. The appearance of serrated step edges upon sulfur adsorption indicates that the compressive stress is high enough to drive the ejection of

Au atoms, which in turn agglomerate at ascending step edges; diffusion across descending steps at room temperature is hindered by the existence of a Schwoebel barrier. The experimentally observed change in the step edge position during sulphur adsorption is consistent with the amount of Au expected based on the amount of excess Au in the reconstruction (4%).

It is quite remarkable that a sulfur coverage of only 0.1 ML is sufficient to completely lift the herringbone reconstruction at room temperature and thus drives a lateral expansion of the Au surface layer by 4%. The expansion/contraction of nanoporous metals in response to modification of the charge density in the surface layer has recently attracted much interest due to potential actuator and sensor applications [18-20]. In this case, the modification of the charge density was achieved by applying an external electrical field rather than by an adsorbate as in the present study.

The unreconstructed Au(111) surface is stable up to a sulfur coverage of 0.3 ML where sulfur forms an ordered ($\sqrt{3}x\sqrt{3}$)R30° adlayer, as verified by LEED (adsorbed S is too mobile to be imaged by STM). Above this coverage we observe a dynamic rearrangement of the Au surface caused by formation of a 2D AuS overlayer phase (Fig. 2). The nucleation of small irregularly shaped islands is accompanied by the formation of monoatomic etch pits, finally leading to a sponge-like surface morphology with a sulfur saturation coverage of 0.6 ML. These observations reveal massive mass transport: Au atoms are removed from the surface layer, thereby creating pits, and incorporated into the growing AuS islands.

The appearance of etch pits suggests that S continues to weaken the Au-Au bonds with increasing S coverage, finally reaching a point where the energy necessary to remove Au atoms from the surface layer is overcompensated by the energy released by the formation of mobile Au-S species. This indicates that the Au-S bond must be relatively strong, at least strong enough to compensate the energy costs accompanied by the removal of Au atoms from regular surface lattice sites. Indeed, stable gold sulfide clusters $(Au_2S)_n$, n = 1, 2, have been identified by *ab initio* calculations [21]. It is interesting that a preferred etching of Au step-edge atoms in *not* observed. The mobilization of Au surface atoms by the interaction with sulfur or sulfur-containing molecules seems to be a general phenomenon: For example, the formation

of vacancies and etch pits has also been observed during the preparation of alkanethiol-based SAMs on Au(111) [2, 3, 22, 23], as well as during the interaction of cysteine with Au(110) [24].

Significant changes in the surface morphology are observed during annealing at 450 K: the sponge-like AuS phase formed at room temperature is transformed into an ordered two-dimensional AuS overlayer which produces a very complex, but well-defined LEED pattern (Fig. 3). Simultaneously large Au vacancy islands of monoatomic depth develop by Ostwald ripening of the irregular etch pits created during formation of the AuS phase at 300 K. Both terraces and vacancy islands are uniformly covered by the 2D AuS phase based on high-resolution STM images.

The AuS overlayer exhibits a 1:1 stoichiometry: AES indicates a sulfur coverage of 0.5 ML, i.e. the sulfur coverage decreases by ~20% during annealing, in excellent agreement with the results obtained by a radioactive ^{35}S tracer-technique [25]; the number of Au atoms incorporated in the 2D AuS phase was estimated to be 0.5 ML by determining the surface area covered by vacancy islands.

High-resolution STM images of the ordered 2D AuS phase reveal a quasi-rectangular unit cell, with lattice parameters of (8.8 Å ± 0.4) x (8.2 ± 0.4) $Å^2$ and 82° ± 4° (Fig. 3b, insert). This seems to be a favourable surface structure under a wide variety of experimental conditions. For example, very similar sulfur-induced surface structures on Au(111) were observed by STM after treatment with aqueous solutions of Na_2S or H_2S [8-12]. The interpretation of these rectangular surface features is controversial although a model of adsorbed S_8 molecules was preferred by the majority of authors. However, the mobilization and incorporation of Au atoms into the growing 2D sulfide phase as revealed by our STM experiments clearly rules out the simple sulfur adlayer model. The complex LEED pattern shown in Fig. 3a is consistent with the STM results and can be interpreted in terms of an incommensurate AuS phase with a quasi-rectangular unit cell. Interestingly, an early study reported a similar LEED pattern from Au(111) surfaces treated with H_2S/H_2 gas mixtures at elevated temperatures [25].

Our results thus suggest a new picture of the S-Au(111) interaction: S-induced perturbation of the Au surface charge density causes a stress relaxation at low S-coverages

and a dynamic restructuring of the surface landscape during formation of a 2D AuS at higher coverages. The incorporation of stoichiometric amounts of metal atoms in adsorbate-induced surface structures is not unique to the S/Au(111) interaction but has also been observed for a variety of other systems, such as S/Ni(111) [26], O/Ag(110) and O/Cu(110) [27]. In the latter two cases, however, the metal atoms (Ag, Cu respectively) appear to be supplied from the energetically less favourable step edge sites. In general, adsorbate-induced mass transport and formation of stoichiometric metal-adsorbate surface structures requires that the metal adsorbate interaction is strong enough to compensate the energy cost of removing metal atoms from regular lattice sites. Thus the AuS formation observed in the present study directly reflects the strength of the Au-S interaction.

The observed phenomena provide a basis for potential sensor or actuator applications: In materials with a high surface-to-volume ratio, such as nanoporous gold, the large S-induced expansion of the Au surface layer (4%) should lead to macroscopically observable dimension changes. Another interesting outlook is the synthesis of single-layer transition-metal disulfide structures using the 2D AuS phase as a sulphur reservoir. Using this approach, we recently demonstrated the preparation of single-layer MoS_2 and TiS_2 structures on Au(111) [28, 29]. Transition metal dichalcogenides are very promising candidates for high mobility flexible inorganic FETs [30].

Acknowledgements:

We gratefully acknowledge the support of this work under the auspices of the Harvard MRSEC supported by NSF Grant no. DMR-02-13805. J. B. acknowledges current support under the auspices of the U. S. Department of Energy by the University of California, Lawrence Livermore National Laboratory, under Contract No. W-7405-Eng-48.

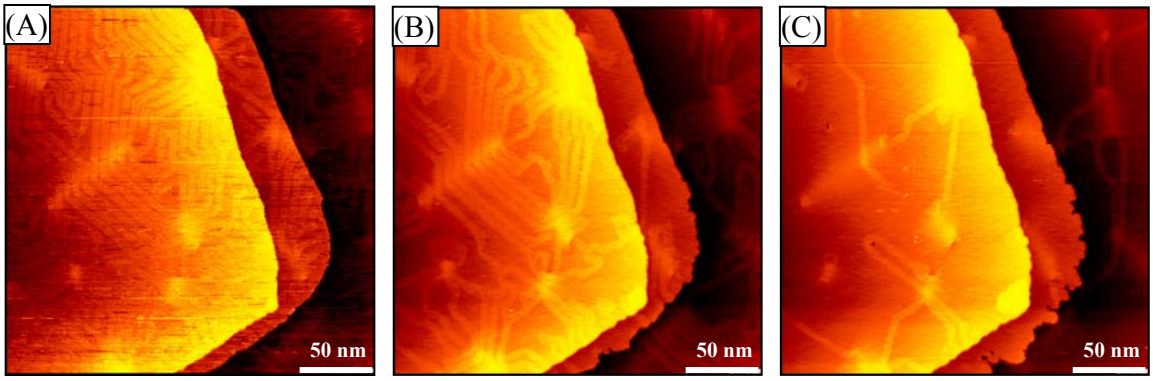

Fig. 1:

Sulfur-induced modification of the Au herringbone reconstruction illustrated by constant-current STM images. (A) Typical herringbone reconstruction pattern of the clean Au(111) surface caused by uni-axial compression of the surface layer by 4%. Note that the elbow sites of the herringbone reconstruction are preferentially aligned along defects (partial Shockley dislocations) that appear as bright spots in the image. (B) A sulfur coverage of 0.05 ML is sufficient to partially lift the herringbone reconstruction. This indicates that adsorbed sulfur atoms decrease the charge density between Au surface atoms thereby turning the tensile surface stress of the clean Au surface into a compressive surface stress. This drives the ejection of Au atoms, which agglomerate at ascending steps as indicated by the appearance of serrated step edges. (C) Lifting of the reconstruction is almost complete reaching a S coverage of 0.1 ML, and corresponds to a lateral expansion of the Au surface layer by 4%. Note the increased serration of the step edges.

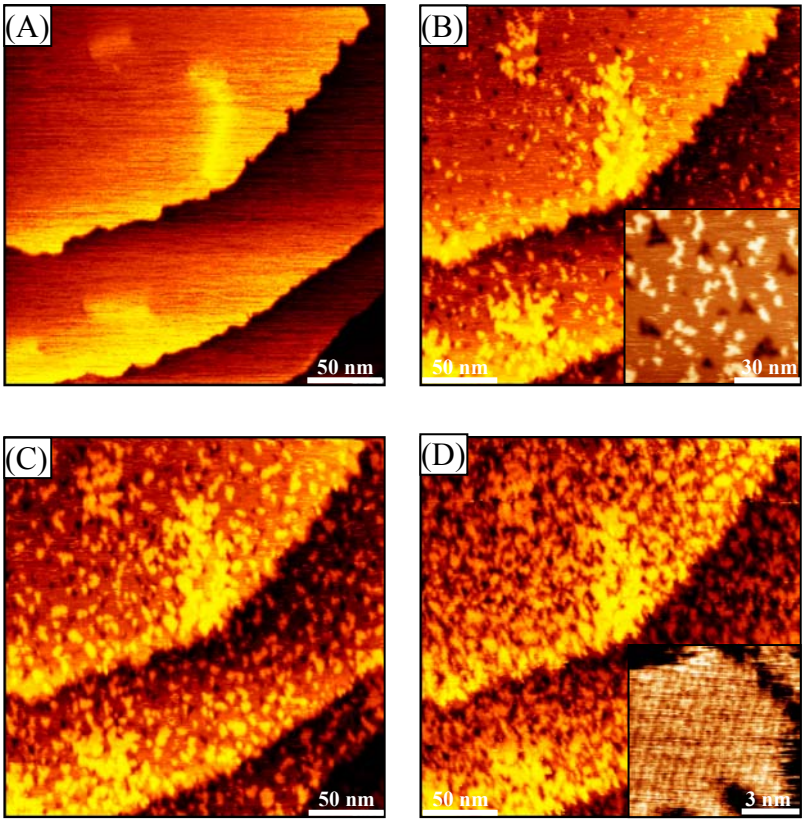

Fig. 2:

Dynamics of the formation of a 2D AuS overlayer captured by real-time STM during continuous SO_2 exposure at room temperature. (A) unreconstructed Au(111) surface with a sulfur coverage of 0.3 ML. The sulfur forms an ordered ($\sqrt{3}$x$\sqrt{3}$)R30° adlayer as observed by LEED. This adlayer is not observable by STM. (B) Early stage of S-induced corrosion/etching of the Au(111) surface. Dark areas (emphasized in the close-up) correspond to monoatomic etch pits. Simultaneously small AuS clusters nucleate on terraces, preferentially at defect sites. (C) The number of both pits and AuS clusters increases with increasing S-coverage. (D) The reaction is completed once the S coverage reaches a value of 0.6 ML. At this point the surface is covered with a sponge-like gold sulfide overlayer exhibiting short-range order as demonstrated by the inset.

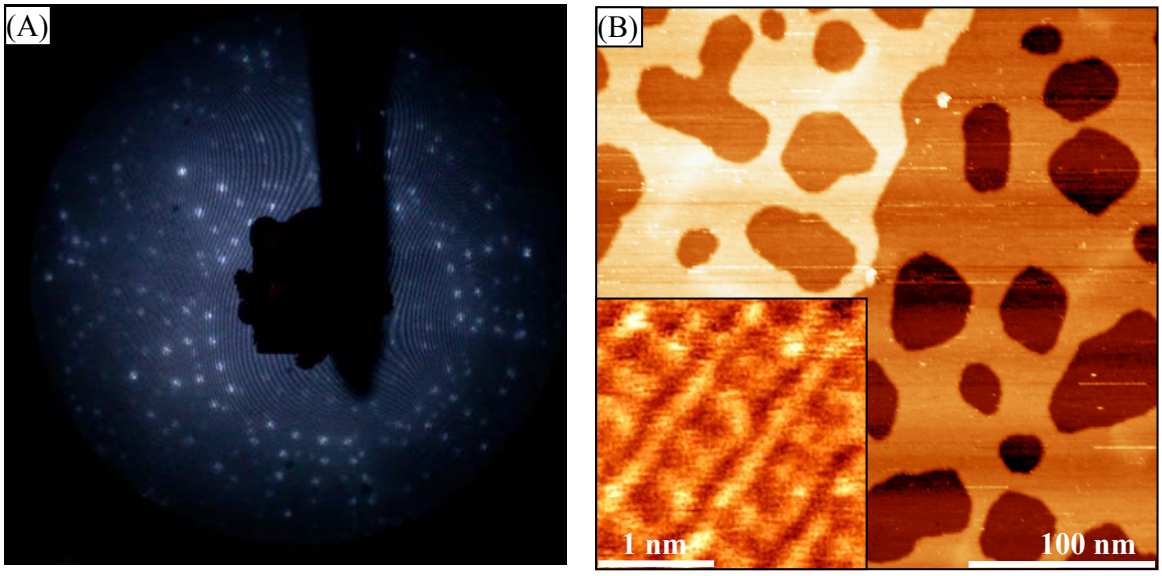

Fig. 3:

A well ordered 2D-AuS phase develops during annealing to 450 K. (A) The structure exhibits a very complex LEED pattern which can be explained by an incommensurate structure with a nearly quadratic unit cell. (B) STM reveals the formation of large vacancy islands by Oswald ripening which cover about 50% of the surface, thus indicating the incorporation of 0.5 ML of Au atoms into the 2D AuS phase. The 2D AuS phase exhibits a quasi-rectangular structure (inset), and uniformly covers both vacancy islands and terrace areas.

References:

(1) Phillips, G. N., Evans, K. A., *Nature*, **2004,** *429*, 860.

(2) Poirier, G. E., *Chem. Rev.*, **1997,** *97*, 1117.

(3) Poirier, G. E., Pylant, E. D., *Science*, **1996,** *272*, 1145.

(4) Ulman, A., *Chem. Rev.*, **1996,** *96*, 1533-1554.

(5) Hammer, B., Norskov, J. K., *Nature*, **1995,** *376*, 238.

(6) Valden, M., Lai, X., Goodman, D. W., *Science*, **1998,** *281*, 1647-1650.

(7) Haruta, M., *Catal. Today*, **1997,** *36*, 153-166.

(8) McCarley, R. L., Kim, Y. T., Bard, J., *J. Phys. Chem.*, **1992,** *97*, 211.

(9) Vericat, C., Vela, M. E., Andreasen, G. A., Salvarezza, R. C., *Phys. Rev. Lett.*, **2003,** *90*, 075506.

(10) Vericat, C., Vela, M. E., Andreasen, G., Salvarezza, R. C., Vazquez, L., Martin-Gago, J. A., *Langmuir*, **2001,** *17*, 4919-4924.

(11) Vericat, C., Andersen, J. N., Vela, M. E., Salvarezza, R. C., *J. Phys. Chem. B*, **2000,** *104*, 302-307.

(12) Gao, X., Zhang, Y., Weaver, M. J., *J. Phys. Chem.*, **1992,** *96*, 4156.

(13) de la Fuente, O. R., Zimmerman, J. A., Gonzalez, M. A., de la Figuera, J., Hamilton, J. C., Pai, W. W., Rojo, J. M., *Phys. Rev. Lett.*, **2002,** *8803*, 6101.

(14) Biener, M. M., Biener, J., Friend, C. M., *in preparation*.

(15) Woell, C., Chiang, R. J., Wilson, J., Lippel, P. H., *Phys. Rev. B*, **1989,** *39*, 7988.

(16) Barth, J. V., Brune, H., Ertl, G., Behm, R. J., *Phys. Rev. B*, **1990,** *42*, 9307.

(17) Ibach, H., *Surf. Sci. Rep.*, **1997,** *29*, 193.

(18) Gleiter, H., Weissmueller, J., Wollersheim, O., Wuerschum, R., *Acta mater.*, **2001,** *737*, 745.

(19) Weissmueller, J., Viswanath, R. N., Kramer, D., Zimmer, P., Wuerschum, R., Gleiter, H., *Science*, **2003,** *300*, 312.

(20) Kramer, D., Viswanath, R. N., Weissmueller, J., *Nanoletters*, **2004,** *4*, 793.

(21) Bagaturyants, A. A., Safonov, A. A., Stoll, H., Werner, H. J., *J. Chem. Phys.*, **1998,** *109*, 3096.

(22) Poirier, G. E., *Langmuir*, **1997,** *13*, 2026.

(23) Chailapakul, O., Sun, L., Xu, C., Crooks, R. M., *J. am. chem. soc.*, **1993,** *115*, 12459.

(24) Kuehnle, A., Linderoth, T. R., Hammer, B., Besenbacher, F., *Nature*, **2002,** *415*, 891.

(25) Kostelitz, M., Domange, J. L., Oudar, J., *Surf. Sci.*, **1972,** *34*, 431-449.

(26) Ruan, L., Stensgaard, I., Besenbacher, F., Laegsgaard, E., *Phys. Rev. Lett.*, **1993,** *71*, 2963.

(27) Guo, X. C., Madix, R. J., *Acc. Chem. Res.*, **2003,** *36*, 471-480.

(28) Biener, M. M., Biener, J., Friend, C. M., *in preparation*.

(29) Biener, M. M., Biener, J., Friend, C. M., *in preparation*.

(30) Podzorov, V., Gershenson, M. E., *Appl. Phys. Lett.*, **2004,** *84*, 3301.

VI

November 09, 2004

submitted to J. Am. Chem. Soc.

Sulfur-induced corrosion of Au(111) studied by real-time STM

Monika M. Biener[1,2], Juergen Biener[3,4] and Cynthia M. Friend[1,2,†]
[1]Department of Chemistry and
[2]Division of Engineering and Applied Sciences and
[3]Center for Imaging and Mesoscale Structures
Harvard University
12 Oxford Street, Cambridge, Massachusetts 02138 USA
[4]Nanoscale Synthesis and Characterization Laboratory
Lawrence Livermore National Laboratory
7000 East Ave, Livermore, CA 94550 USA

[†]Author to whom correspondence should be sent

Abstract

The interaction of sulfur with gold surfaces has attracted considerable interest due to numerous technological applications such as the formation of self-assembled monolayers (SAMs), use as a corrosion inhibitor, and as a chemical sensor.[1-3] In this work, the interaction of sulfur with Au(111) at two different temperatures (300 K and 420 K) was studied by real-time scanning tunnelling microscopy (STM), low energy electron diffraction (LEED) and Auger electron spectroscopy (AES). In the low coverage regime (< 0.1 monolayer), S modifies the surface stress leading to a lateral expansion of the Au surface layer. An ordered ($\sqrt{3}$x$\sqrt{3}$)R30° sulfur adlayer develops as the coverage reaches ~0.3 ML. With further increasing S coverage the Au(111) surface undergoes a dynamic rearrangement while forming a two-dimensional AuS phase: gold surface atoms are removed from regular terrace sites and incorporated into the growing gold sulfide phase resulting in the appearance of pits and irregularly shaped AuS islands. Gold sulfide prepared at room temperature exhibits short-range order; an incommensurate, long-range ordered AuS phase develops upon annealing at 450 – 525 K. Higher temperatures lead to decomposition of the AuS corrosion film. Formation of an ordered AuS phase via rapid step retraction rather than etch pit formation is observed during S-interaction with Au(111) surfaces *at* 420 K. Our results shed new light on the S-Au(111) interaction.

Introduction

Au is an important material in microelectronics due to its high electrical conductivity in combination with corrosion resistance. The noble character of Au does not imply a general inability to form stable bonds with non-metals but is rather a consequence of high reaction barriers towards dissociation reactions.[4] However, under certain circumstances Au surfaces can exhibit a high catalytic reactivity, and indeed Au-based catalysts are being developed for industrial oxidation processes.[5, 6] The Au-S interaction is probably the most intensively studied interaction of Au surfaces with a non-metal as it is important in numerous technological applications: Au ore formation,[7] thiol-based self-assembled monolayers (SAMs),[3, 8, 9] and corrosion inhibition, to name only a few. Furthermore, the increase of the electrical resistivity of thin gold films upon adsorption of certain sulphur-containing gases can be exploited to design sensors which allow the detection of minute traces of those species in gaseous mixtures.[2, 10] However, an atomic level picture of the underlying mechanism for the resistivity change has not been given yet, although numerous studies on the S/Au(111) interaction have been performed in recent years.

A very complex picture of the S/Au(111) interaction has emerged as demonstrated by the variety of surface structures formed when S is adsorbed under different experimental conditions.[1, 11-19] The majority of these structures were interpreted in terms of a "classic" surface model, where the positions of the Au atoms remain essentially unperturbed upon interaction with S. A common structure is the $(\sqrt{3}x\sqrt{3})R30°$ S adlayer with a coverage of 0.33 ML[1, 11, 13-15, 18] where sulfur atoms occupy threefold-hollow sites. This is also a commonly observed structure for alkanethiolate based SAMs on Au(111).[3] Ordered arrays of rectangular structures were observed at higher S coverages,[1, 11, 12, 14, 15] which were predominantly attributed to adsorbed S_8 species.

In the present study we used real-time STM in combination with low energy electron diffraction (LEED) and Auger electron spectroscopy (AES) to investigate both low and high S-coverage regimes. Real-time STM provides us with nano-scale, time resolved information and reveals the very dynamic character of the Au(111) surface upon interaction with sulfur, such as large-scale mass transport and incorporation of Au atoms in a growing AuS phase. In view of the typically observed inertness of Au surfaces the S-induced corrosion and

mobilization of Au atoms is surprising and sheds new light on the nature of the Au-S interaction.

Experimental

All experiments were performed in an ultrahigh vacuum (UHV) system with a base pressure of $4x10^{-10}$ torr. The system is equipped with a home-made "beetle-type" STM and commercial instrumentation for AES and LEED. The sample was radiatively heated via a tungsten filament located behind the sample, and the temperature was monitored by a chromel/alumel thermocouple affixed to the sample holder. To account for the temperature gradient of the sample holder versus the crystal a calibration was performed using a thermocouple directly mounted to the crystal.

The Au sample was cleaned by cycles of Ar^+ sputtering (1000eV, ~5 μA) at 300 K, followed by annealing to 700 K for 10 minutes and 600 K for 60 minutes. This procedure was repeated several times until no contaminants were detected using AES. Following this procedure, the characteristic Au(111)-(22x√3) "herringbone" reconstruction was observed by LEED and STM. The Au sample used for the experiments of the present study exhibits many surface defects (see fig. 1 and 4), most likely partial Shockley dislocations[20] introduced by the gentle annealing procedures.

SO_2 (Matheson, anhydyrous grade) served as a source of sulfur, and was introduced using a leak valve such that a steady-state chamber pressure of $2x10^{-7}$ torr was maintained. Gas lines were evacuated before each dose. All exposures are given in uncorrected ion gauge readings using units of Langmuir ($1L=10^{-6}$ torr•s). Only a small fraction of the SO_2 molecules that impinge on the surface decomposes and deposits sulfur. The sulfur coverage was monitored by AES and calibrated relative to the (√3x√3)R30° LEED pattern which corresponds to a S coverage of 0.33 ML. The exposure of the surface to SO_2 was interrupted at various times and the surface examined using AES. The only species detected on the surface at all times was sulphur; oxygen, if any, was below the detection limit of AES. The oxygen released by SO_2 decomposition seems to be removed via an abstraction reaction with excess SO_2.[21] In order to rule out effects due to electron-induced reactions, the experiments were reproduced with the ion gauge turned off.

All STM images shown in this work were collected at room temperature or 420 K (if indicated) using $Pt_{0.8}$ $Ir_{0.2}$ tips. The tunneling bias was set in the range of +60 mV to +1.0 V. The STM scanner was calibrated against the unit cell of the Au(111) surface. Real-time STM images were collected during continuous SO_2 exposure. We observe the same S induced changes irrespective of whether the SO_2 exposure was prior to or during scanning.

Results and Discussion

The dynamic rearrangement of Au(111) surfaces with increasing S coverage at room temperature was captured by real-time STM imaging. The sequence of images displayed in figure 1 reveals a lifting of the herringbone reconstruction in the low S coverage regime followed by the formation of a 2D AuS phase at higher S coverages. The clean Au(111) surface exhibits a characteristic reconstruction pattern (fig. 1a, insert) that is caused by the incorporation of an additional 4% of Au atoms in the surface layer to reduce the tensile surface stress as described in detail elsewhere.[22, 23] This Au(111)-(√3x22) herringbone reconstruction is also signified by the presence of characteristic satellites spots in the LEED pattern shown in figure 2a.[24]

The surface stress of the clean Au(111) surface is modified upon sulfur adsorption. As a consequence, the herringbone reconstruction is lifted, even at S coverages as low as 0.1 ML. Au atoms, which are expelled during the surface relaxation, agglomerate at the step edges thus causing a serrated (wavy) step-edge appearance (fig. 1b). Simultaneously the satellite spots in the LEED pattern associated with the herringbone structure disappear (fig 2b). The ejection of Au atoms revealed by STM indicates that S adsorption reverses the surface stress from tensile to compressive.

The origin of adsorbate-induced compressive surface stress can be understood in terms of a charge transfer from substrate surface bonds to the adsorbate atoms.[25] This in turn drives the ejection of Au atoms, which agglomerate at ascending step edges. Diffusion across descending steps at room temperature is hindered by the existence of a “Schwoebel” barrier. The amount of Au atoms as judged by the observed change in the step edge position during sulfur adsorption is consistent with the expected amount of ejected Au atoms (4%). The

lifting of the Au(111) reconstruction by small amounts of strongly (specifically) adsorbed anions is also a common observation in electrochemical environments.[26]

An ordered (√3x√3)R30° sulfur adlayer develops as the S coverage approaches ~0.3 ML as inferred from the observation of a well-defined (√3x√3)R30° LEED pattern. As the LEED pattern develops, fractional-order spot-splitting is observed (figure 2c). Splitting of fractional-order spots can be explained by ordered arrays of antiphase domains[27], where the amount of splitting correlates with the domain size. The amount of splitting in our case corresponds to a (5x5) superlattice of the (√3x√3)R30° structure. The fractional-order spot-splitting disappears as the S coverage approaches 0.33 ML (fig. 2d).

The (√3x√3)R30° S adlayer observed by LEED is not observed using STM. Instead, atomically-resolved images of the Au surface were repeatedly obtained (figure 2c inset). These data indicate that the sulfur in the (√3x√3)R30° adlayer is too mobile to be imaged under the tunneling conditions used in the present work (see experimental). This is consistent with the streaky appearance of the STM images obtained in this coverage regime. A similar result was reported for K and Na (√3x√3)R30° adlayer phases on Au(111).[28, 29] However, the Au(111)-(√3x√3)R30°-S phase has been imaged by STM in an electrochemical environment.[1, 11, 14, 15]

Upon further increasing sulfur coverage we observe a dynamic surface restructuring caused by formation of a 2D AuS phase (figure 1d-f): small irregularly shaped islands start to nucleate, preferentially at defects, and monoatomic etch pits develop. Both pits and islands appear on terraces, and their density increases with increasing S-coverage (Fig. 1e). These observations indicate that there is massive mass transport: Au atoms are removed from regular terrace sites, thereby creating pits, and incorporated into the growing AuS phase. Finally the surface is completely covered with a 2D gold sulfide phase (Fig.1f) which exhibits a sponge-like morphology and passivates the Au surface against further corrosion. The S saturation coverage is 0.6 ML. The (√3x√3)R30° LEED pattern disappears (figure 2e) upon the formation of the first clusters, and a diffuse LEED pattern indicating missing long-range order is obtained.

The appearance of etch pits suggests that S continues to weaken the Au-Au bonds with increasing S coverage, finally reaching a point where the energy necessary to remove Au atoms from regular lattice sites is overcompensated by the energy released by the formation of mobile Au-S species. This demonstrates that the Au-S bond is strong enough to drive the corrosion of Au. Indeed, stable gold sulfide clusters $(Au_2S)_n$, n = 1, 2, have been identified by ab initio calculations.[30] It is interesting that a preferred etching of Au step-edge atoms is not observed (see below).

The mobilization of Au surface atoms by the interaction with sulfur or sulfur-containing molecules seems to be a general phenomenon: For example, the formation of 2D vacancy islands of monoatomic depth has also been observed during the preparation of alkanethiol-based SAMs on Au(111).[8, 9, 31, 32] The driving force for the formation of these structures was, however, not clear; it was speculated that the vacancies may be related to a thiol-induced surface restructuring that enhances the Au surface diffusion rate. Mobilization of Au atoms and vacancy formation has also been observed during the interaction of cysteine with Au(110) surfaces.[33]

Significant changes in the surface topography are observed upon annealing: the sponge-like AuS phase formed at room temperature is transformed into an ordered two-dimensional AuS phase which produces a very complex, but well-defined LEED pattern (figure 2e). Simultaneously, large vacancy islands of monoatomic depth develop by Ostwald ripening of the irregular etch pits created during formation of the AuS phase at room temperature. Figure 3 shows the changes in the surface morphology as a function of the annealing temperature. Ring-like structures with some short-range order are observed after annealing to 420 K, and long-range order develops during annealing to 450 K. The growing vacancy islands are of monoatomic depth and both terraces and vacancy islands are uniformly covered by the AuS phase, based on the fact that the STM images are the same in vacancies and on terraces. The development of long-range order is further emphasized by the observation of a well-defined, complex LEED pattern (figure 2e).

The well-ordered AuS overlayer obtained after annealing exhibits a 1:1 stoichiometry: AES indicates a sulfur coverage of 0.5 ML, i.e. the sulfur coverage decreases by ~20% during annealing, in excellent agreement with the results obtained by a radioactive ^{35}S tracer-

technique;[16, 17] the number of Au atoms incorporated in the 2D AuS phase was estimated to be 0.5 ML by determining the surface area covered by vacancy islands.

High-resolution STM images of the ordered 2D AuS phase reveal a quasi-rectangular unit cell, with lattice parameters of (8.8 ± 0.4) x (8.2 ± 0.4) $Å^2$ and an angle of 82° ± 4° between the lattice vectors (Figure 3e).The complex LEED pattern (figure 2f) is consistent with the STM results and can be interpreted in terms of an incommensurate AuS phase with a quasi-rectangular unit cell and 6 rotational domains. The orientation of one unit cell axes is rotated by ~7 degrees relative to the [110] direction of the Au substrate. This is consistent with the arrangement of rotational domains to each other as observed by STM. Interestingly, an early study reported a similar LEED pattern from Au(111) surfaces treated with H_2S/H_2 gas mixtures at elevated temperatures.[16, 17]

The ordered AuS phase described above seems to be a favorable configuration as very similar sulfur-induced surface structures on Au(111) have been prepared by electrooxidation in aqueous solutions of Na_2S or H_2S at room temperature.[1, 11, 12, 14, 15] The interpretation of these rectangular surface features is controversial although a model of adsorbed S_8 molecules was preferred by the majority of authors. However, the S-induced mobilization of Au atoms revealed by the present study clearly rules out a simple sulfur adlayer model.

In contrast to the UHV experiments presented here the ordered AuS phase develops without annealing in an electrochemical environment thus suggesting an increased surface mobility under these conditions. An anion-enhanced surface mobility is a common phenomenon in electrochemistry, and is indeed the basis of the so-called electrochemical annealing.[26, 34] It has been suggested that the increased mobility of Au surface atoms is caused by the anion-induced weakening of Au-Au surface bonds. This effect is more pronounced the more positive the potential and/or the stronger the anion-Au interaction.[26] Since the Au-S interaction is very strong, as demonstrated by the observed etching, it is not surprising that the ordered AuS phase can be formed in an electrochemical environment even at room temperature. However, the mass transport involved in the S-Au(111) interaction has not been reported earlier, and the majority of S-induced surface structures were consequently interpreted in terms of a simple adlayer surface model, where the positions of the Au atoms remain essentially unperturbed upon interaction with S.

The dynamic rearrangement of the Au surface upon interaction with S was further investigated by real-time scanning *at* 420 K. Figure 4 shows a series of STM images collected from a Au(111) surface as a function of increasing S coverage at 420 K. Using a defect (see arrow in fig. 4a) as reference point allows us to track changes in the step edge morphology during interaction with S. In the low coverage regime, the S-induced surface modifications are very similar to those observed during the corresponding room temperature experiments: the herringbone reconstruction is lifted, and Au atoms are ejected and agglomerate at step edges. Diffusion along step edges is fast at 420 K, and thus the step edges remain relatively straight (fig 4b), in contrast to the serrated step edge morphology observed during room temperature experiments (fig 1b). However, in the high coverage regime (~0.3 ML to ~0.5 ML) we detect a sudden retraction of step edges (figures 4c-f) rather than the etch pit and island formation observed at RT. After the step-edge position becomes stable again, indicating equilibrium, a S coverage of 0.5 ML was measured by AES (at 420 K). Despite missing evidence for AuS formation *at* 420K (except Au mobilization evidenced by step-retraction), the long-range ordered AuS phase described above is observed via LEED and STM *after* cooling the sample to room temperature (data not shown).

The sudden retraction of steps upon reaching a sulfur coverage of ~0.3 ML at 420 K is in contrast to the development of etch pits and islands at 300 K. The appearance of etch pits at 300 K indicates that Au atoms are pulled out of regular terrace sites, driven by the formation of stable AuS complexes which then nucleate to form irregularly shaped AuS islands. In contrast, at 420 K Au atoms in the surface layer seem to be mobile enough to annihilate any arising vacancy structure on the time scale of the experiment (~ 2 min per frame), which leads to the impression of retracting step-edges. An alternative explanation would be that Au atoms are indeed supplied from weaker bound step edges sites. In this case, the absence of preferred step-edge etching at room temperature would indicate step-edge passivation by adsorbed AuS species or, alternatively, the development of a sulphur depletion zone at the step edge (diffusion-limited reaction regime).

The fate of the Au atoms which were removed from regular surface sites, but not detected as AuS islands as in the case of the room temperature experiment also needs to be considered. Since the amount of missing Au atoms is certainly too high to be explained in terms of mobile Au adatoms, we conclude that mobile AuS complexes are formed at 420 K.

Upon cooling to room temperature a liquid-solid phase transition seems to take place. Alternatively, a coverage dependent liquid-solid phase transition could take place *at* 420 K, but this would require that the phase transition happens between two scans as otherwise we would have observed intermediate stages of the transition. Anyway, the ordered AuS thus obtained is identical to the AuS phase formed by room temperature reaction and subsequent annealing.

A quantitative analysis of the STM images shown in figure 4 reveals that the steps retract by ~ 0.5 ML equivalents (integrated area over the displacement of the step edges during S exposure). This is in excellent agreement with the surface area covered by vacancy islands after AuS formation at room temperature (figure 3c), and further corroborates our statement that 0.5 ML Au atoms are incorporated in the AuS phase.

The AuS phase is stable up to a temperature of ~ 525 K. During formation of the ordered AuS phase in the temperature range from 450 K to 525 K, the S coverage decreases by approx. 20% from 0.6 ML to 0.5 ML. Higher annealing temperatures cause a rapid decrease of the sulphur coverage. Simultaneously the well-defined LEED pattern (figure 2e) becomes diffuse. Figure 5 shows the S coverage as determined by the S_{150}/Au_{239} AES peak ratio versus annealing temperature.The sample was annealed for 20 minutes at each temperature and subsequently AE spectra were collected at room temperature. The loss of sulfur is most likely caused by the decomposition of the AuS corrosion film, rather than desorption of AuS units. Indeed, it has been reported that Au_2S decomposes into Au and S at temperatures above 490 K.[35]

Our results provide an atomic level picture of the working principle of Au-based sensors[10] for S containing gas species: a 2D AuS corrosion film is formed via massive mass transport at room temperature and decomposes above 525 K thereby restoring the sensing capacity. The AuS forms a pure 2D phase as it passivates the surface against further corrosion. This suggests that sensors with an enhanced sensitivity can be developed on the basis of nanoporous gold as this material exhibits a very high surface to volume ratio.

Conclusion

The results presented provide new insight into the S-Au(111) interaction. Sulfur interacts strongly with the Au(111) surface which leads to stress relaxation in the low S-coverage regime and corrosion involving a dynamic surface restructuring in the high S coverage regime. Specifically, S adsorption lifts the herringbone reconstruction of the Au(111) surface even at a S coverage as low as 0.1 ML. The lifting of the herringbone reconstruction can be explained by a S-induced *weakening* of Au-Au surface bonds, which causes a lateral expansion of the Au surface layer. This reverses the surface stress from tensile to compressive as revealed by the ejection of Au atoms. As the S coverage approaches ~0.3 ML, an ordered (√3x√3)R30° sulfur adlayer develops. The S-induced weakening of Au-Au surface bonds continues with further increasing S coverage, which finally leads to the corrosion of the Au surface: gold surface atoms are removed from regular terrace sites and incorporated into the growing two-dimensional AuS phase resulting in the appearance of etch pits and irregularly shaped AuS islands. The development of the 2D AuS phase passivates the Au surface against further corrosion. Long-range order develops upon annealing at 450 – 525 K, higher temperatures lead to decomposition of the AuS corrosion film. A smooth, long-range ordered AuS phase without vacancy island structures can be prepared by S-interaction with Au(111) surfaces *at* 420 K.

Acknowledgements:

We gratefully acknowledge the support of this work by Harvard University NSEC, funded by the National Science Foundation, grant no. PHY-01-17795.

J. B. acknowledges current support under the auspices of the U. S. Department of Energy by the University of California, Lawrence Livermore National Laboratory, under Contract No. W-7405-Eng-48.

References

(1) Vericat, C., Vela M. E., Andreasen G., Salvarezza R. C., Vazquez L. and Martin-Gago J. A., *Langmuir* **2001**, *17*, 4919-4924.

(2) Yoo, K. S., Sorensen I. W. and Glaunsinger W. S., *J. Vac. Sci. Technol. A* **1994**, *12*, 192-198.

(3) Ulman, A., *Chem. Rev.* **1996**, *96*, 1533-1554.

(4) Hammer, B. and Norskov J. K., *Nature* **1995**, *376*, 238.

(5) Valden, M., Lai X. and Goodman D. W., *Science* **1998**, *281*, 1647-1650.

(6) Haruta, M., *Catal. Today* **1997**, *36*, 153-166.

(7) Phillips, G. N. and Evans K. A., *Nature* **2004**, *429*, 860.

(8) Poirier, G. E., *Langmuir* **1997**, *13*, 2026.

(9) Poirier, G. E., *Chem. Rev.* **1997**, *97*, 1117.

(10) *U.S. Patent No. 4724008*, (Arizona Instrument Corporation, 1988)

(11) Vericat, C., Andersen J. N., Vela M. E. and Salvarezza R. C., *J. Phys. Chem. B* **2000**, *104*, 302-307.

(12) McCarley, R. L., Kim Y. T. and Bard J., *J. Phys. Chem.* **1992**, *97*, 211.

(13) Martin, H., Vericat C., Andreasen G., Creus A. H., Vela M. E. and Salvarezza R. C., *Langmuir* **2001**, *17*, 2334-2339.

(14) Vericat, C., Vela M. E., Andreasen G. A. and Salvarezza R. C., *Phys. Rev. Lett.* **2003**, *90*, 075506.

(15) Gao, X., Zhang Y. and Weaver M. J., *J. Phys. Chem.* **1992**, *96*, 4156.

(16) Kostelitz, M. and Oudar J., *Surf. Sci* **1971**, *27*, 176.

(17) Kostelitz, M., Domange J. L. and Oudar J., *Surf. Sci.* **1972**, *34*, 431-449.

(18) Rodriguez, J. A., Dvorak J., Jirsak T., Gang L., Hrbek J., Aray Y. and Gonzalez C., *J. Am. Chem. Soc.* **2002**, *125*, 276-285.

(19) Touzov, I. and Gorman C. B., *Langmuir* **1997**, *13*, 4850.

(20) de la Fuente, O. R., Zimmerman J. A., Gonzalez M. A., de la Figuera J., Hamilton J. C., Pai W. W. and Rojo J. M., *Phys. Rev. Lett.* **2002**, *8803*, 6101.

(21) Biener, M. M., Biener J. and Friend C. M., *in preparation*

(22) Woell, C., Chiang R. J., Wilson J. and Lippel P. H., *Phys. Rev. B* **1989**, *39*, 7988.

(23) Barth, J. V., Brune H., Ertl G. and Behm R. J., *Phys. Rev. B* **1990**, *42*, 9307.

(24) Murty, M. V. R., Curcic T., Judy A. and Cooper B. H., *Phys. Rev. B* **1999**, *60*, 16956.

(25) Ibach, H., *Surf. Sci. Rep.* **1997**, *29*, 193.

(26) Kolb, D. M., *Prog. Surf. Sci.* **1996**, *51*, 109.

(27) Van Hove, M. A., Weinberg W. H. and Chan C. M., *Low-Electron Energy Diffraction* (Springer-Verlag, 1986).

(28) Barth, J. V., Behm R. J. and Ertl G., *Surf. Sci. Lett.* **1993**, *302*, L319-L324.

(29) Barth, J. V., Schuster R., Behm R. J. and Ertl G., *Surf. Sci.* **1995**, *348*, 280.

(30) Bagaturyants, A. A., Safonov A. A., Stoll H. and Werner H. J., *J. Chem. Phys.* **1998**, *109*, 3096.

(31) Poirier, G. E. and Pylant E. D., *Science* **1996**, *272*, 1145.

(32) Chailapakul, O., Sun L., Xu C. and Crooks R. M., *J. Am. Chem. Soc.* **1993**, *115*, 12459.

(33) Kuehnle, A., Linderoth T. R., Hammer B. and Besenbacher F., *Nature* **2002**, *415*, 891.

(34) Kolb, D. M., *Surf. Sci.* **2001**, *500*, 722.

(35) Ishikawa, K., Isonaga T., Wakita S. and Suzuki Y., *Solid State Ionics* **1995**, *79*, 60.

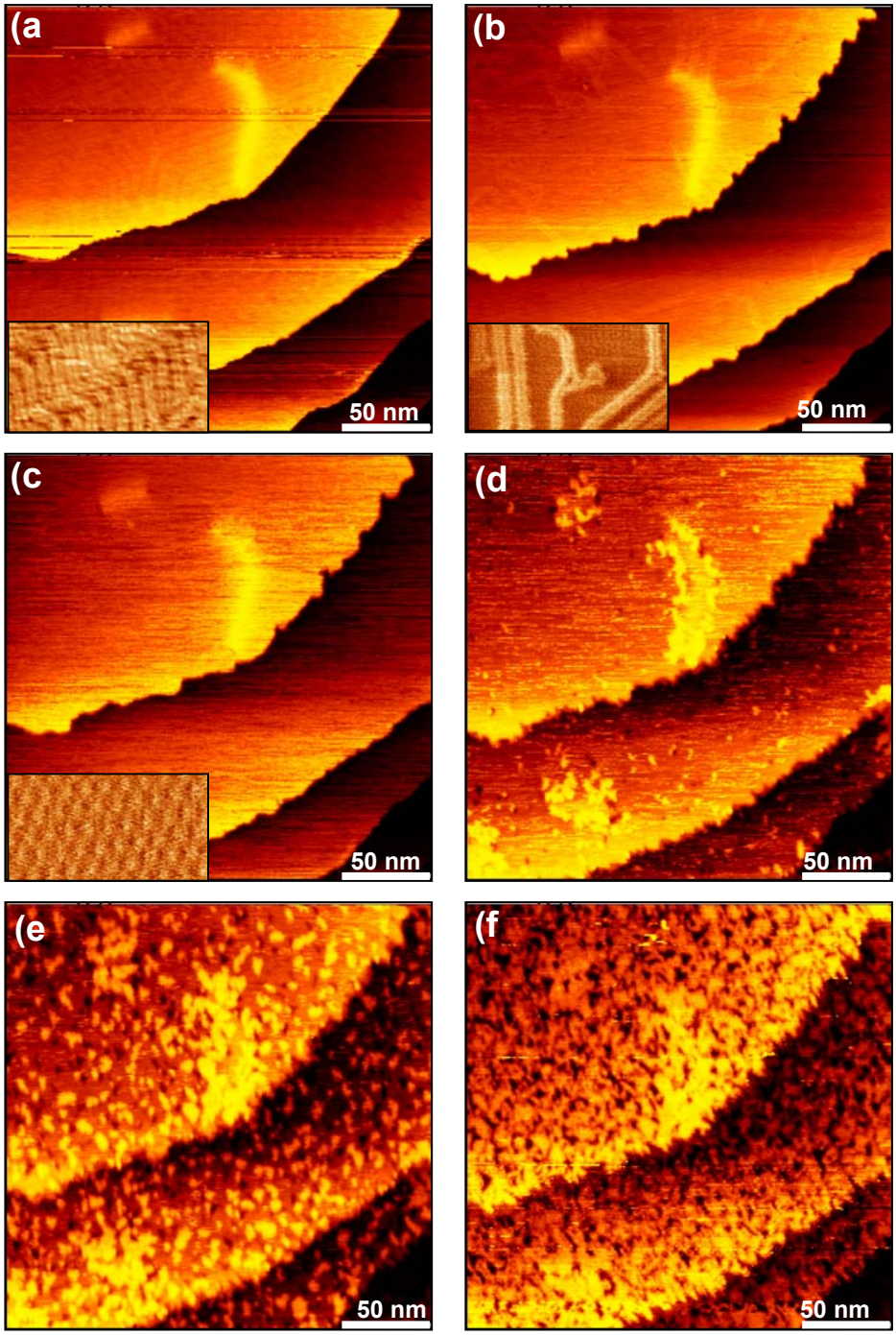

Figure 1: Real-time STM images capturing the dynamics of the S-induced Au corrosion at room temperature. (a) clean Au(111) surface exhibiting the typical herringbone reconstruction pattern (insert, 90 x 50 nm^2) caused by a 4% compression of the surface layer. (b) Even a small sulfur coverage (≤ 0.1 ML) reverses the surface stress from tensile to compressive and thereby drives the ejection of Au atoms. As a consequence the herringbone reconstruction is lifted (see insert, 75 x 40 nm^2). The ejected Au atoms agglomerate at ascending step edges leading to a serrated step edge appearance. (c) The unreconstructed Au(111) surface is stable up to a S coverage of ~ 0.3 ML, where S forms an ordered ($\sqrt{3}$x$\sqrt{3}$)R30° adlayer, which is transparent for STM (see atomically resolved Au surface in inset (2.6 x 1.5 nm^2)), but evident by LEED (fig. 2d). Early stages of the S-induced Au corrosion: (d) monoatomic etch pits and small AuS clusters appear on terraces, and (e) their density increases with increasing S-coverage. (f) At a sulfur coverage of ~0.6 ML the Au surface is covered with a sponge-like gold sulfide phase which passivates the surface against further corrosion.

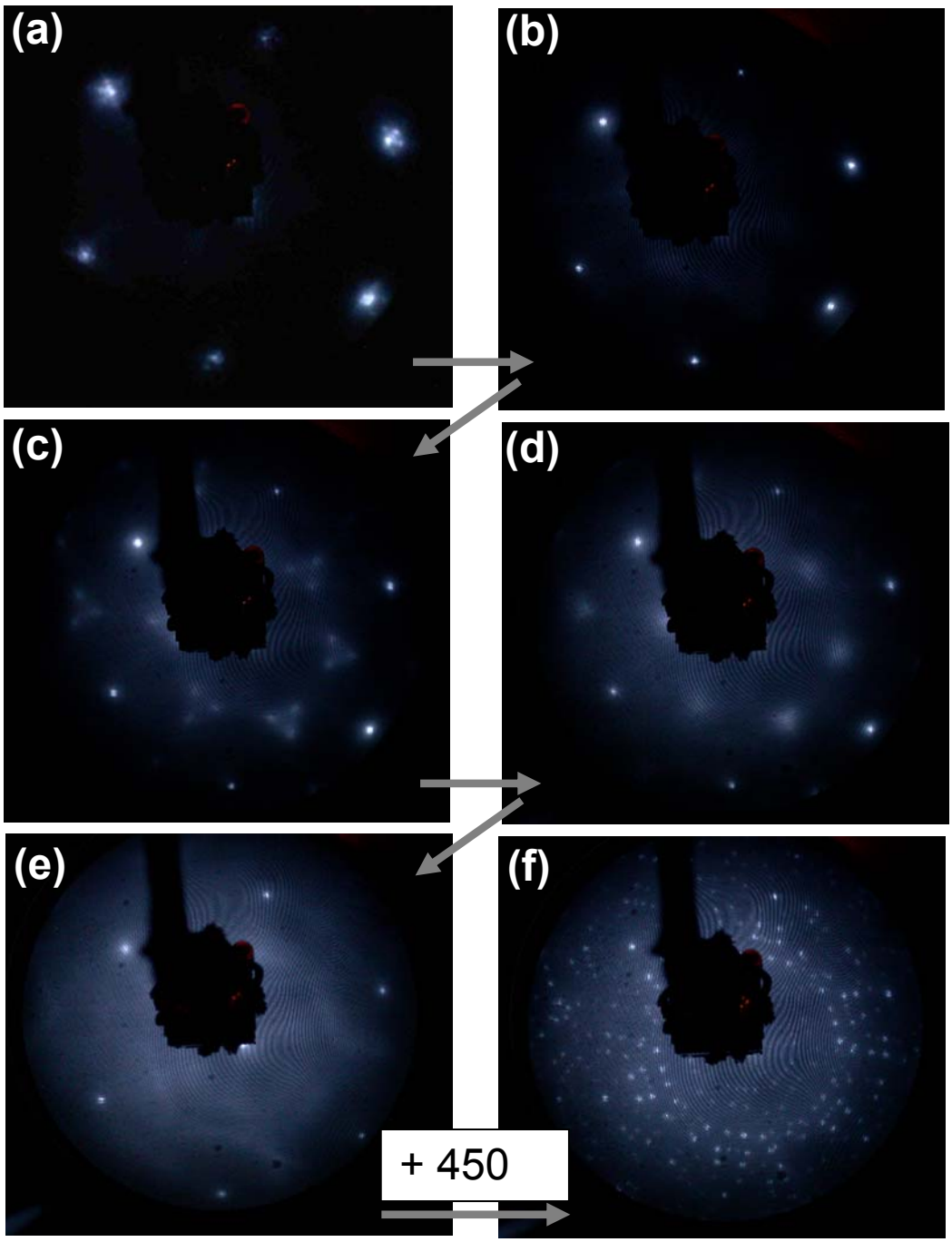

Figure 2: Monitoring the S-induced corrosion of Au(111) by LEED: (a) clean, reconstructed Au(111) surface exhibiting the satellites of the Au(1,1) spots associated with the herringbone reconstruction. (b) The satellites disappear even at a low sulfur coverage (≤ 0.1 ML). (c) A (√3x√3)R30° pattern with split fractional-order spots develops, and (d) transforms into a regular (√3x√3)R30° pattern at a S-coverage of 0.33 ML. (e) With further increasing S coverage the LEED pattern becomes diffuse (0.33 ML < θ_S ≤ 0.6 ML). (f) The well-defined complex LEED pattern observed after annealing to 450 K indicates the formation of an incommensurate AuS phase with long-range order (θ_S ~ 0.5 ML). All LEED images were obtained at an electron beam energy of 68 eV.

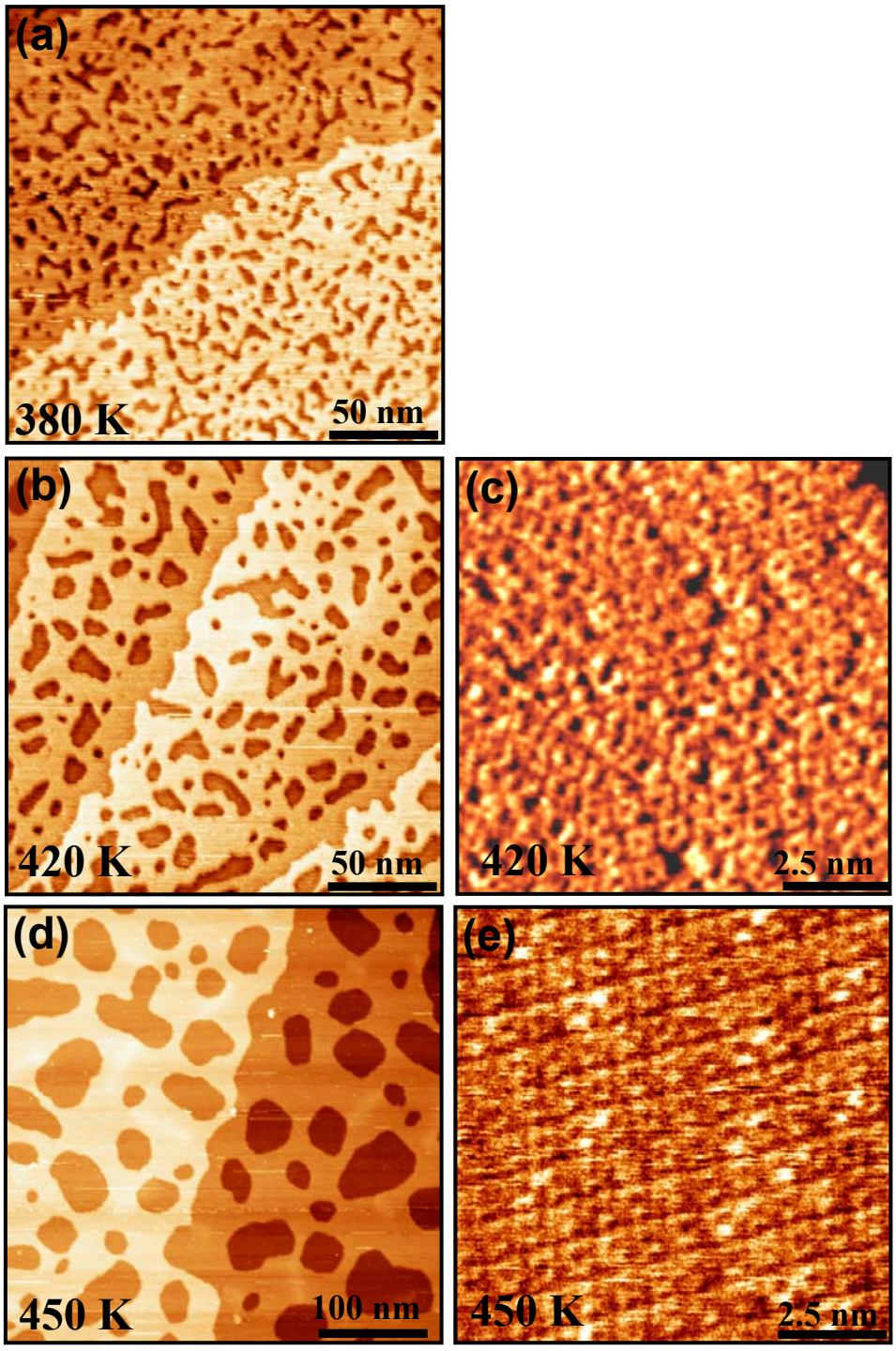

Figure 3: The morphology of the sponge-like AuS phase formed at room temperature (fig 1f) changes upon annealing. STM images were collected at room temperature after 10 min of annealing at 380 K (a), 420 K (b,c), and 450 K (d,e), respectively. With increasing annealing temperature, the original irregular etch pits transform into increasingly larger vacancy islands of monoatomic depth (Oswald ripening). Independent of the annealing temperature, the vacancy islands cover ~50% of the surface area, indicating the incorporation of ~0.5 ML of Au atoms into the 2D AuS phase. (c) After annealing to 420 K, some locally ordered arrays of quasi-rectangular structures can be observed by high-resolution STM. (e) Long-range order develops during annealing at 450 K. The AuS phase uniformly covers both vacancy islands and terrace areas.

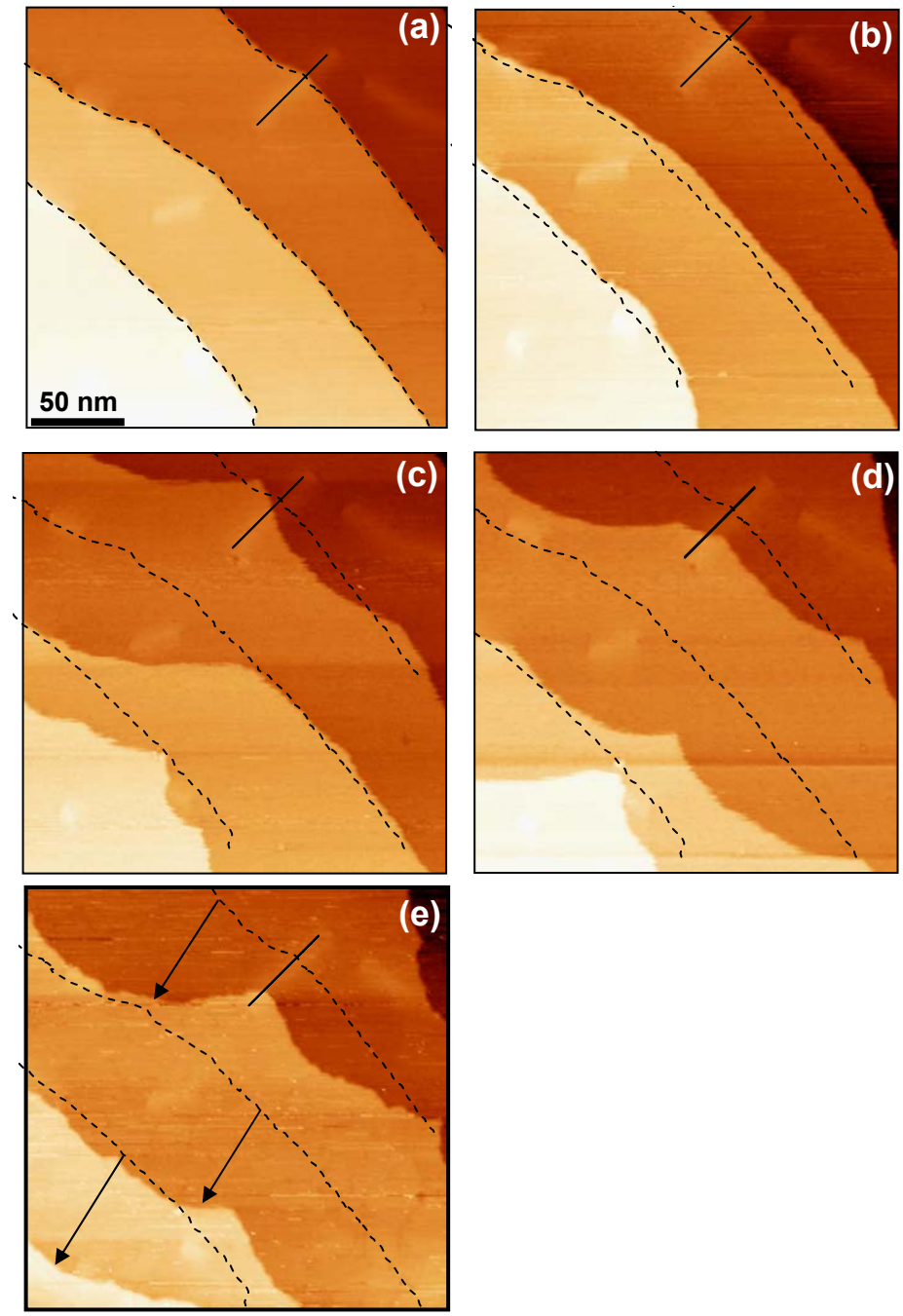

Figure 4: Dynamic restructuring of the surface landscape upon interaction with S *at* 420 K, monitored by real-time STM: A surface defect (marked by the straight line) is used as reference point to track changes in the step morphology with respect to the original step edge structure (dashed lines), and to correct for the thermal drift of the experiment (note the lateral translation of the dashed lines in the different frames). (a) Clean Au(111) surface. (b) Sulfur lifts the reconstruction of the Au surface: the additional Au atoms incorporated in the reconstruction (4%) are ejected and agglomerate at ascending steps as evidenced by the outward flow of the steps. (c,d,e) With increasing S-coverage (0.3 ML to 0.5 ML) the steps suddenly retract indicating the removal of Au atoms from the surface layer and formation of a "liquid" AuS phase which is not visible in STM under the conditions of our experiments.

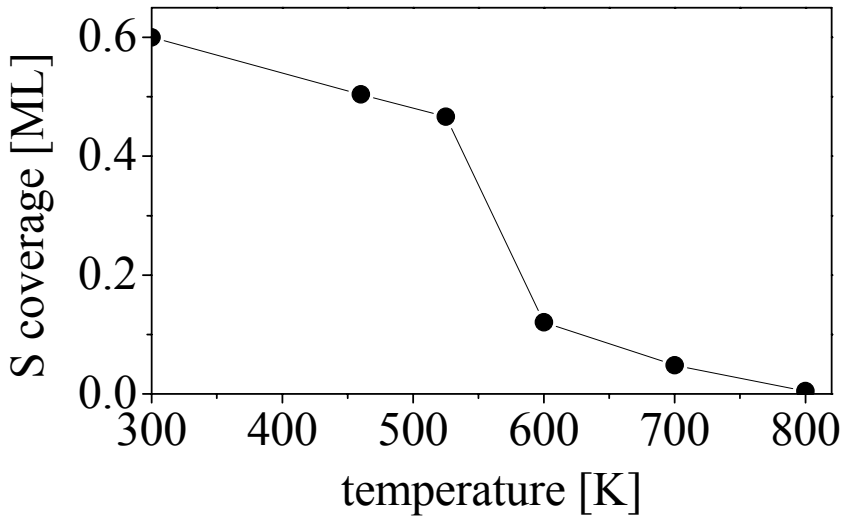

Figure **5**: The amount of S incorporated in the 2D AuS phase (prepared at room temperature) versus annealing temperature, as determined by the S_{150}/Au_{239} AES peak ratio (calibrated against the (√3x√3)R30° S adlayer with a S coverage of 0.33 ML). The sample was annealed for 20 minutes at each temperature and AE spectra were subsequently recorded at room temperature. Development of the long-range ordered AuS phase in the temperature range from 450 K to 525 K is accompanied by a decrease of the S coverage of approx. 20%. Higher annealing temperatures lead to a rapid loss of sulfur, most likely caused by AuS decomposition.

VII

To be submitted to: Surf. Sci. Lett.
November, 2004

Enhanced transient reactivity of an O-sputtered Au(111) surface

Monika M. Biener[1,2], Juergen Biener[3,4], and Cynthia M. Friend[1,2, †]
[1]Department of Chemistry and
[2]Division of Engineering and Applied Sciences and
[3]Center for Imaging and Mesoscale Structures
Harvard University
12 Oxford Street, Cambridge, Massachusetts 02138 USA
[4]Lawrence Livermore National Laboratory
7000 East Ave, Livermore, CA 94550 USA

[†]Author to whom correspondence should be sent

Abstract

The interaction of SO_2 with oxygen-sputtered Au(111) surfaces ($\theta_{oxygen} \leq 0.35$ ML) was studied by monitoring the oxygen and sulfur coverages as a function of SO_2 exposure. Two reaction regimes were observed: oxygen depletion followed by sulfur deposition. An enhanced, *transient* sulfur deposition rate is observed at the oxygen depletion point. This effect is specifically pronounced if the Au surface is continuously exposed to SO_2. The enhanced reactivity towards S deposition seems to be linked to the presence of highly reactive, under-coordinated Au atoms. Adsorbed oxygen appears to stabilize, but also to block these sites. In absence of the stabilization effect of adsorbed oxygen, i.e. at the oxygen depletion point, the enhanced reactivity decays on a timescale of a few minutes. These observations shed a new light on the catalytic reactivity of highly dispersed gold nanoparticles.

Introduction

The high reactivity of dispersed gold nanoparticles supported on metal oxide surfaces has recently attracted considerable interest. For example, gold nanoparticles on TiO_2(110) are very efficient catalysts for the low-temperature oxidation of CO,[1] as well as for the decomposition of SO_2.[2] Various models have been proposed to explain the unusual catalytic properties of gold nanoclusters ranging from metal-support interactions to finite size effects.[1] A new aspect of gold nanoclusters was recently introduced by Rodriguez et al.,[2] who performed a theoretical study on the reactivity of under-coordinated Au atoms. The study reveals that under-coordinated Au atoms in Au nanoparticles can play an important role. Specifically, it was demonstrated that SO_2 interacts more strongly with under-coordinated Au atoms than with regular terrace atoms of a Au(111) surface.

In contrast to the high reactivity of supported Au nanoparticles, bulk metallic gold typically exhibits a low reactivity. For example, Liu et al. observed that SO_2 adsorbs molecularly on Au(111) at 100 K,[3] and desorbs without noticeable decomposition at 150 K. Recently, we investigated the interaction of SO_2 with Au(111) at 300 K, and observed the formation of a two-dimensional gold sulfide overlayer by using large exposures of SO_2.[4] A possible mechanism for the observed S deposition is the disproportionation of SO_2 into adsorbed S and SO_3, in which the latter species desorbs. There is precedent for SO_3 formation during SO_2 exposure to oxygen-covered Cu(110) and oxygen-covered Ag(110).[5, 6] However, on these surfaces SO_3 does not desorb but decomposes with increasing temperature, consistent with a recent theoretical investigation[7] based on the bond order conservation-Morse potential method.

In the present work we employed Auger Electron Spectroscopy (AES) to study the interaction of SO_2 with an oxygen-sputtered Au(111) surface by monitoring the oxygen and sulfur coverages as a function of SO_2 exposure. We explain the observed reaction kinetics of sulfur deposition in terms of an enhanced *transient* reactivity of under-coordinated gold species. The experiments described in this paper contribute to a better understanding of the enhanced catalytic reactivity of supported Au nanoparticles used as oxidation catalysts.

Experimental

The experiments were performed in a UHV system with a base pressure of $5x10^{-11}$ mbar. The system is equipped with commercial instrumentation for STM, AES and LEED, and details of the experimental setup are published elsewhere.[8] The purity of both, oxygen (Matheson, research purity grade) and SO_2 (Matheson, unhydrous grade) was periodically checked with a residual gas analyzer. SO_2 was dosed by backfilling the chamber at pressures between $5x10^{-7}$ and $2x10^{-6}$ mbar (uncorrected ion gauge reading). The Au(111) sample was cleaned by cycles of Ar sputtering at room temperature (60 min/1000 eV/4 μA) and annealing (10 min at 900 K followed by one hour at 600 K) until contaminations were no longer detected by means of AES.

Oxygen-sputtering (500 V, 1 μA, 300 K) of Au(111) surfaces leads to surface roughening and chemisorption of oxygen. According to Saliba et al.[9] an O_{519}/Au_{239} AES peak-to-peak height ratio of 1.0 corresponds to a oxygen coverage of ~ 0.85 ML. Using this calibration, we observed a oxygen saturation coverage of 0.35 ML ± 0.05 ML (1 ML = $1.4x10^{15}$ cm^{-2}). The S coverage was calibrated against the S_{150} AES signal obtained from a Au(111)/(√3x√3)R30° S surface.[4]

In order to study the effect of annealing (and thus decreasing surface roughness) on the reactivity towards SO_2, some oxygen-sputtered Au(111) surfaces were annealed to 400 K prior to SO_2 exposure. AES reveals that the oxygen coverage decreases by ~ 40 % during annealing of oxygen-sputtered Au(111) surfaces. This can be explained by isothermal desorption of molecular oxygen, as the onset of oxygen desorption from Au(111) is observed at ~ 400 K.[9]

STM images were collected at room temperature, and Z-channel as well as I-channel images were obtained simultaneously. Etched $Pt_{0.8}$ $Ir_{0.2}$ tips from Molecular Imaging were used for imaging.

Results and Discussion

Oxygen-sputtering of Au(111) surfaces introduces a rough surface morphology as illustrated by the STM images shown in Fig. 1. For this particular preparation the Au surface was exposed to a fluence of ~ 6 x 10^{15} O_2^+ ions/cm^2 (corresponding to ~ 9 ML). After annealing to 400 K (10 minutes), AES reveals an oxygen coverage of ~ 0.2 ML. The sputtered surface remains relatively smooth on a large scale (Fig. 1a), and the original step-terrace structure can still be observed. However, a close-up view of the image (Fig. 1b) reveals the development of a rough surface morphology consisting of mounds and pits. The symmetry of both, mounds and pits, reflects the hexagonal symmetry of a (111) surface, and the length scale of the pattern is ~ 15 nm (Fig. 1b). A similar surface morphology has been observed after Ar^+ ion bombardment of Au(111) surfaces.[10, 11] The linescan shown in Fig. 1c reveals a short range surface roughness of up to ~1.0 nm (corresponding to 4 monoatomic steps).

The rough surface morphology of oxygen-sputtered Au(111) (Fig. 1) can be easily modified by tip-sample interactions during STM imaging. Figure 2 shows an area of the sample which has been modified during a previous scan in the upper part of the image: the length scale of the pattern increases as mounds and pits coalesce, and the corrugation decreases from ~1.0 nm (4 monoatomic steps) to ~0.25 nm (1 monoatomic step) as illustrated by the linescan shown in Fig. 2, bottom. Notably, this phenomenon was only observed immediately after the tip was cleaned by applying 10 V pulses (to another area of the sample) — a procedure that repetitively yields a tip that exhibits metallic behavior, as judged by the observed current (I) vs. voltage (V) curves.

The depletion of adsorbed oxygen and the deposition of S on oxygen-sputtered Au(111) surfaces during exposure to SO_2 was monitored by AES. The oxygen coverage decreases with increasing SO_2 exposure, as revealed by the decreasing O_{519}/Au_{239} AES peak ratio (Fig. 3, open symbols). The deposition of sulfur is delayed, and only observed after the initially adsorbed oxygen completely disappeared based on the S_{150}/Au_{239} AES peak ratio (Fig. 3, full symbols). The depletion of oxygen is not caused by electron stimulated oxygen desorption during AES data collection, as consecutive Auger spectra collected in the absence of SO_2 do not result in a decreasing O_{519}/Au_{239} AES peak ratio. Annealed (squares/ triangles)

and as-sputtered (circles) surface preparations exhibit the same behavior with respect to oxygen depletion and sulfur deposition.

The decreasing oxygen coverage with increasing SO_2 exposure suggests that chemisorbed oxygen on Au(111) surfaces can be abstracted by impinging SO_2 molecules via SO_3 formation:[12]

$SO_2 + O_{ad} \rightarrow SO_{3,\,gas}$ (I)

The deposition of sulfur is only observed *after* oxygen is *completely* removed by reaction (I). The observation of S deposition can be explained in terms of a disproportionation reaction of SO_2 into adsorbed S and SO_3 via a two-step mechanism:

SO_2 decomposition: $SO_2 \rightarrow S_{ad} + 2O_{ad}$, (II)

followed by O abstraction (I). As the oxygen released by SO_2 decomposition (II) is not detected by AES, oxygen abstraction (I) is required to be considerably faster than SO_2 decomposition (II). Indeed, the rate of oxygen abstraction is roughly 4 times faster than the rate of SO_2 decomposition as judged by the experimentally observed rates of oxygen depletion/sulfur deposition (Fig. 3).

The Au(111) surface exhibits an enhanced, transient reactivity towards SO_2 decomposition within the first one hundred langmuir of SO_2 exposure after reaching the oxygen depletion point (Fig. 4). The extent of this reactivity enhancement is strongly influenced by the experimental procedure: The step-like increase in the S-coverage at the oxygen depletion point is more pronounced if the Au surface is continuously exposed to SO_2 while reaching the oxygen depletion point (Fig. 4, squares and tringles). Specifically, a four times higher jump in the sulfur coverage is observed for continuous SO_2 exposure compared to an experiment where the SO_2 exposure was frequently interrupted for collecting AES data (Fig. 4, circles). This reveals that the surface reactivity towards SO_2 disproportionation decreases on a timescale of a few minutes (typical time necessary to collect AES data) after reaching the oxygen depletion point.

An oxygen-sputtered Au(111) surface exhibits a very rough surface morphology, and thus a high concentration of under-coordinated Au atoms, even after annealing to 400 K (Fig. 1). This is not a very stable surface configuration as demonstrated by the observation of tip-induced surface modifications during STM imaging (Fig. 2). Very similar surface

morphologies have been reported for nanoporous Au, where it has been argued that chemisorbed oxygen stabilizes small pores and thus under-coordinated Au atoms present on these highly curved surfaces.[13, 14] If under-coodinated Au atoms are indeed stabilized by chemisorbed oxygen, the depletion of oxygen during interaction with SO_2 should destabilize the rough surface morphology of an oxygen-sputtered Au(111) surface.

In a recent theoretical study, Rodriguez et al.[2] emphasize the enhanced catalytic reactivity of under-coordinated Au atoms. Specifically, the study demonstrates that under-coordinated Au atoms interact strongly with adsorbed SO_2, and decomposition is only slightly less favorable than desorption. The calculated activation barriers for decomposition and desorption of SO_2 on Au clusters consisting of 14 atoms are ~22 kcal/mol and ~15 kcal/mol, respectively. Following these results, we attribute the enhanced, transient reactivity towards SO_2 decomposition at the oxygen depletion point to the presence of under-coordinated Au atoms: oxygen adsorption stabilizes these sites but also blocks the catalytic activity. Efficient SO_2 decomposition is observed only after all initially adsorbed oxygen is removed by reaction (I). Surface rearrangements on a timescale of a few minutes (triggered by oxygen depletion) explain the transient character of these highly reactive sites. Consistent with our experimental observations, this effect is more pronounced for unannealed Au(111)/O surfaces (annealing generally reduces the surface roughness).

The oxygen depletion observed in the present study suggests SO_3 formation. Formation of SO_3 was also observed during interaction of SO_2 with oxygen-covered Cu(110) and Ag(110) surfaces at 300 K.[5, 6] However, on these surfaces, SO_3 does not desorb, but decomposes during consequent heating. The reaction energetics of the interaction of SO_2 with Cu, Ag, and Au (111) surfaces was previously calculated by Sellers et al..[7] This study reveals that SO_2 can react with chemisorbed oxygen on Au and Ag surfaces towards SO_3. In addition, distinct periodic trends for the reaction barriers of decomposition and desorption of SO_3 were reported: the barrier for SO_3 desorption decreases in the order Cu, Ag, Au (23 kcal/mol, 21 kcal/mol, 19 kcal/mol), whereas the barrier for SO_3 decomposition increases in the order Cu, Ag, Au (3 kcal/mol, 10 kcal/mol, 12 kcal/mol). These values suggest that desorption of SO_3 is more likely on Au than on Cu or Ag, consistent with our interpretation of the experimental results discussed above.

Our results contribute to a better understanding of the reactivity of highly dispersed gold nanoparticles. The enhanced reactivity of Au nanoparticles is generally interpreted as either a confinement effect or in terms of metal-support interactions. The present work, however, provides evidence that under-coordinated Au atoms can play an important role by increasing the reactivity, even in the absence of a specific metal-support interaction.

Conclusion

Two reaction regimes were observed during interaction of SO_2 with an O-sputtered Au(111) surface: oxygen removal and S deposition. The surface exhibits an enhanced reactivity towards SO_2 decomposition at the oxygen depletion point. This is attributed to the presence of highly reactive, under-coordinated Au species which are activated by oxygen depletion. The transient nature of these species explains the observed decrease in reactivity towards sulfur deposition within minutes.

Acknowledgements

We gratefully acknowledge the support of this work by Harvard University NSEC, funded by the National Science Foundation, grant no. PHY-01-17795.
J. B. acknowledges current support under the auspices of the U. S. Department of Energy by the University of California, Lawrence Livermore National Laboratory, under Contract No. W-7405-Eng-48.

References

1 M. Valden, X. Lai, and D. W. Goodman, Science 281 (1998) 1647.
2 J. A. Rodriguez, M. Perez, T. Jirsak , et al., Chem. Phys. Lett. 378 (2003) 526.
3 G. Liu, J. A. Rodriguez, J. Dvorak, et al., Surf. Sci. 505 (2002) 295.
4 M. M. Biener, J. Biener, and C. M. Friend, (submitted)
5 A. R. Alemozafar, X.-C. Guo, and R. J. Madix, J. Chem. Phys. 116 (2001) 4698.
6 A. R. Alemozafar, X.-C. Guo, R. J. Madix, et al., Surf. Sci. 504 (2002) 223.
7 H. Sellers and E. Shustorovich, J. Mol. Catal. A 119 (1996) 367.
8 M. M. Biener, J. Biener, R. Schalek, et al., in press
9 N. Saliba, D. H. Parker, and B. E. Koehl, Surf. Sci. 410 (1998) 270.

[10] V. Viashnyakov, S. E. Donnelly, and G. Carter, Philos. Mag. B 70 (1994) 151.

[11] K. P. Reimann, A. Rehmet, W. Bolse, et al., in *Mat. Res. Soc. Symp.* (Materials Reasearch Society, 1997), Vol. 439, p. 361.

[12] Unfortunately, our experimental setup did not allow us to directly detect the reaction product SO_3 by mass spectroscopy. Thus we can not completely rule out the possibility that the observed oxygen loss is caused by a reaction of adsorbed oxygen with background CO.

[13] A. Dursun, D. V. Pugh, and S. G. Corcoran, J. Electrochem. Soc. 150 (2003) B355.

[14] R. C. Newman, S. G. Corcoran, J. Elrlebacher, et al., MRS Bulletin 24 (1999) 24.

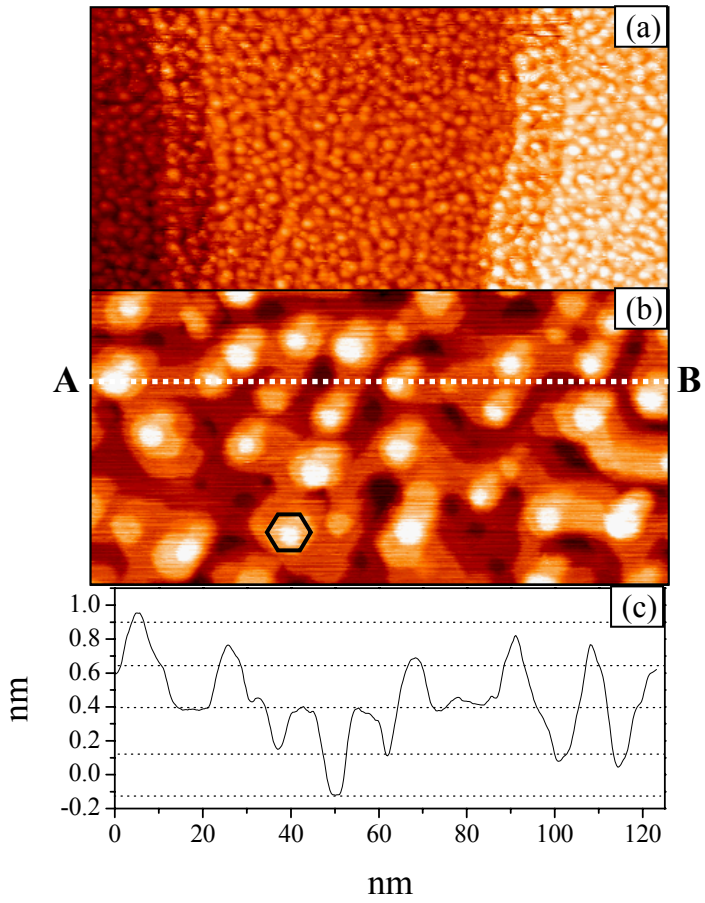

Fig. 1:
STM images showing the morphology of an O-sputtered Au(111) surface. (a) The surface is relatively smooth on a large scale and the original step-terrace structure can still be observed. (b) Locally the surface exhibits a rough morphology consisting of mounds and pits. The pattern reflects the hexagonal symmetry of a (111) surface. (c) The surface roughness of ~ 1 nm (corresponding to 4 monoatomic steps) is demonstrated in the linescan along the line between A and B.. The oxygen coverage is estimated to be 0.2 ML, based on the O_{519}/Au_{239} AES peak ratio. (a): 500 nm x 250 nm, and (b) 125 nm x 62nm.

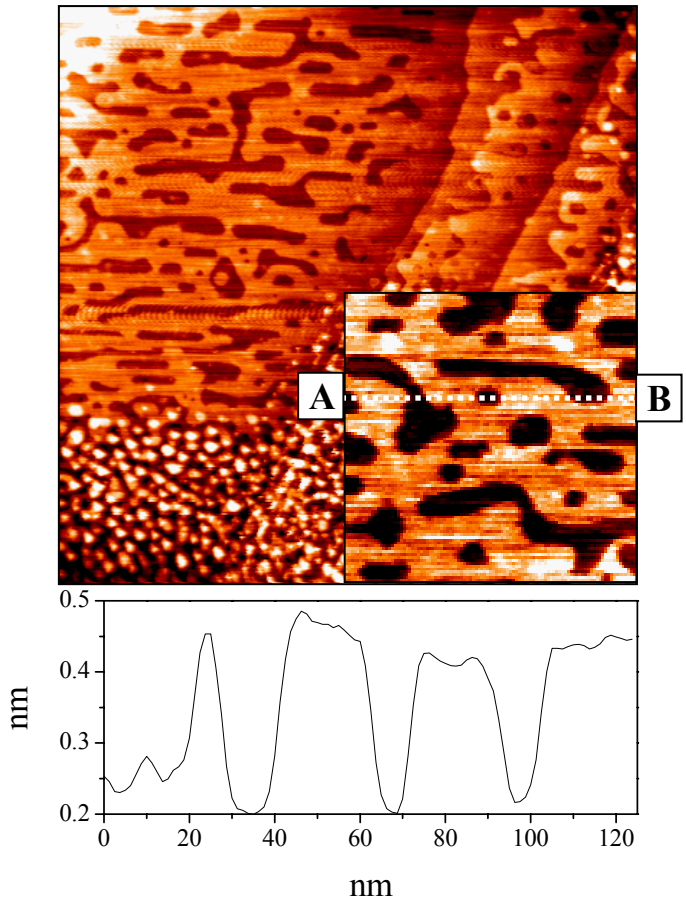

Fig. 2:
STM images of an O-sputtered Au(111) surface after tip-induced surface modification. The image is a zoom-out of a surface area that was previously scanned. The area that was previously scanned (top part) exhibits a different morphology: the islands coalesce and the corrugation decreases to 1 monoatomic step, as illustrated by the linescan along the line between A and B. 500 nm x 500 nm (inset: 125 nm x 125 nm).

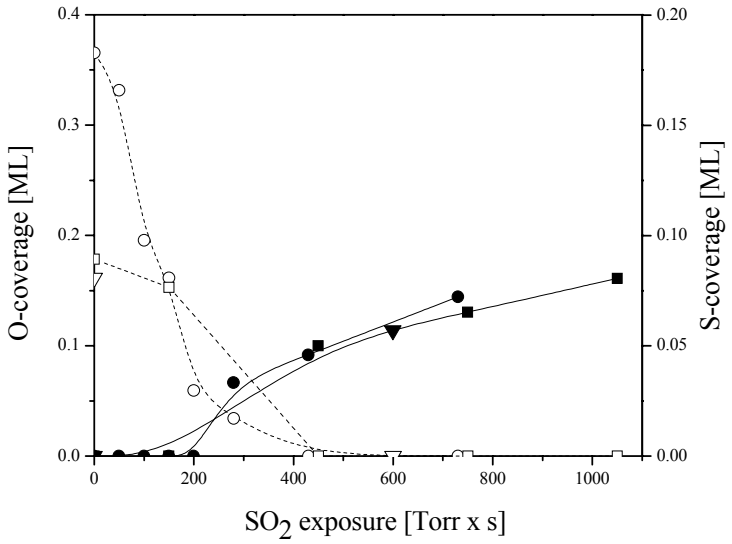

Fig. 3:
O_{519}/Au_{239} AES peak ratio (open symbols) and S_{150}/Au_{239} AES peak ratio (full symbols) obtained from as-sputtered (circles) as well as annealed (squares/triangles) surfaces as a function of SO_2 exposure at 300 K. The oxygen coverage decreases with SO_2 exposure and the sulfur deposition starts after oxygen is completely removed.

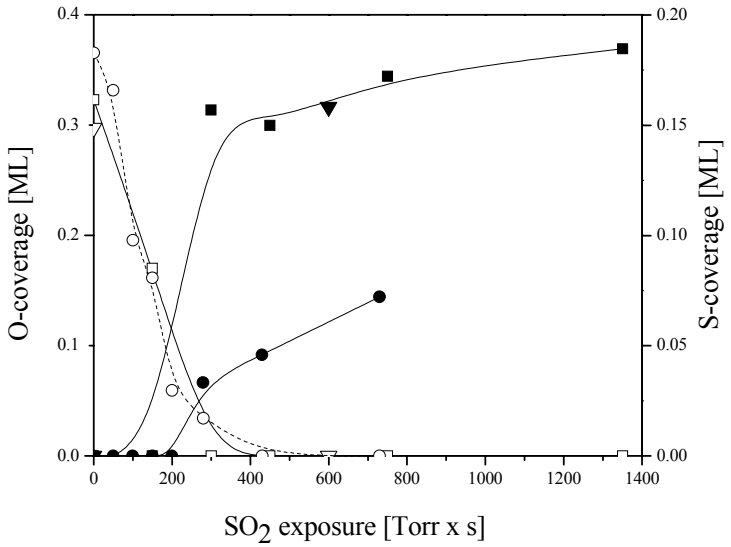

Fig. 4:
O_{519}/Au_{239} AES peak ratio (open symbols) and S_{150}/Au_{239} AES peak ratio (full symbols) versus SO_2 exposure at 300 K for 3 different unannealed preparations. The circles represent the same data as those displayed in figure 3, the squares and triangles show oxygen and sulfur coverage for larger SO_2 dosing increments. The surface exhibits an enhanced transient reactivity towards SO_2 decomposition if SO_2 is continuously dosed at the oxygen depletion point (squares and triangles). This indicates the existence of transient highly reactive Au species.